The method of homogenisation as a means to parameterise small-scale processes in the ocean and atmosphere

Edward James Goldsmith

A dissertation submitted in partial fulfillment
of the requirements for the degree of
Doctor of Philosophy
of
University College London.

Department of Mathematics
University College London

August 9, 2022

I, Edward James Goldsmith, confirm that the work presented in this thesis is my own. Where information has been derived from other sources, I confirm that this has been indicated in the work.

Signature ________________________

Date 09/08/2022

Abstract

The first part of this thesis examines how finite-amplitude, small-scale topography affects small-amplitude motions in the ocean. The technique of homogenisation is used to develop an ‘averaged’ system based on the rotating shallow water equations in the presence of topography with horizontal extent much less than the wavelengths of the long waves in question. The extent to which the dispersion relations of Poincaré, Kelvin and Rossby waves are modified from their flat-bottomed counterparts is illuminated, using a range of numerical and analytical techniques. Both random and regular periodic arrays of topography are considered, with the special case of regular cylinders studied in detail, because this case allows for highly accurate analytical results. We find formulae for the approximate frequency change for all three wave types, with a particularly simple analytic expression for the Rossby wave dispersion relation, extending previous results from the quasi-geostrophic regime. In addition to this, the manner in which trapped topographic Rossby waves affect the dispersion relations for a finite topography is illuminated.

The second part examines the propagation of atmospheric waves through a small-scale convective cloud field. The method of homogenisation reveals that the small-scale clouds act to vertically redistribute the horizontal momentum and buoyancy profiles of the large-scale flow. Mathematically, this occurs due to the presence of non-local integral operators involving ‘transilient kernels’ in the homogenised equations. The dispersion relations are plotted for some of the wave modes propagating in a mid-latitude β-channel, which show that the cloud field slows the baroclinic waves, with low-frequency waves most affected.

Impact statement

Parameterisation is one of the most fundamental concepts in predictive meteorology, since it allows large-scale numerical weather prediction simulations and general circulation models to capture the effects of small-scale phenomena in the absence of a high-resolution grid. These models are used ubiquitously for predicting daily weather patterns, extreme weather events and climate change across many time-scales, and are vital to our understanding of the oceans and atmosphere. Perfecting the manner in which small-scale processes such as convection are parameterised in these models is therefore of key importance for accurately predicting the weather and climate in real-time, whilst introducing as few biases as possible.

In this thesis, we use the mathematical method of homogenisation to investigate multiple-scale phenomena in the oceans and atmosphere with a view to accurately building parameterisations of convection. We assess the consequences of using parameterisations based on the horizontal average of a quantity across a grid cell, concluding that they lead to potentially large errors in modelling predictions. Crucially, our analyses allow us to produce non-heuristic parameterisations of both wave-topography interactions in the ocean and wave-cloud interactions in the atmosphere, which avoid these modelling errors. Our work has implications for the creation of accurate convective parameterisations in large-scale models, which in turn has consequences for how we predict not only daily weather occurrences, but also catastrophic weather and climate events.

The material is presented in a manner so as to highlight the utility of homogenisation as means to parameterise small-scale processes in a geophysical setting, and to motivate its use in future weather and climate models.

Acknowledgements

First and foremost, I would like to thank my primary supervisor, Professor Gavin Esler, for his continual support throughout my Ph.D. As well as providing me with all the assistance I could have possibly asked for, he has always done so with the utmost kindness, compassion, and sympathy (even when I've ill-advisedly refused to make things easy for myself).

I would also like to thank my secondary supervisor, Professor Valery Smyshlyaev, for helping me get a handle on the theory of homogenisation, and for helping me locate and translate some elusive Russian papers.

Credit must also go to Professor Ted Johnson, and my supervisor at the Met Office, Dr Mike Whitall, for useful and inspiring discussions at various times throughout my Ph.D.

On a more personal note, I'd like to thank my parents, Brenda and Tony Goldsmith, and my brother, Jonny Goldsmith for their unwavering love and support throughout my life. Without them, I would never have completed this Ph.D. and for that, I am eternally grateful.

Finally, I would like to thank Adrian Wilson-Smith, without whom this thesis would likely never have reached completion.

The work in chapter 3 and Appendices B–E has appeared in the paper (Goldsmith and Esler, 2021), written in collaboration with Professor J. G. Esler at University College London.

This thesis was completed under the supervision of ***Professor J. G. Esler****.*

Contents

List of Figures

Chapter 1

Introduction

Geophysical phenomena occur across a variety of different spatial and temporal scales. As a consequence, the fluid dynamics associated with the oceans and atmosphere can be very difficult to model from a numerical standpoint, since the discretisation of a model which describes large-scale processes can require a huge number of grid points in order to fully resolve the small-scale motions. One such example of where motions spanning multiple scales is of particular relevance is the phenomenon of convection in the atmosphere. Notably, atmospheric convection is a highly turbulent process with fluxes of momentum and buoyancy, as well as thermodynamic variations occurring on spatial scales of less than one kilometre; however, convective clouds also aggregate, and form large, coherent structures such as hurricanes (Houze, 1993), squall lines (Houze, 1977), mesoscale convective complexes (North et al., 2015), and superclusters (Mapes and Houze, 1993). Whilst it is true that the ability of computers to tackle such complex problems has increased exponentially in the last several decades, there still exist enormous deficits in computing power which must be overcome in order to produce accurate meteorological models - in particular, global circulation models (GCMs) and numerical weather prediction (NWP) simulations are often unable to be run efficiently on a grid with a high enough resolution to resolve cloud structures (Collins et al., 2013). For this reason, multi-scale modelling has become a very heavily studied topic across the many disciplines involved with GCMs and NWP simulations, and remains of key importance in building accurate weather and climate forecasts.

Since small-scale processes cannot be resolved by the grids used in large-scale models, meteorologists use a method known as *parameterisation* to represent these phenomena. The idea is that instead of trying to resolve the small-scale motions explicitly, which necessarily requires much finer resolutions, one can include their effects by approximating their bulk properties at each point on a much coarser grid. Naturally, the improved efficiency that parameterisation brings to the models comes at a cost, namely that the small-scale dynamics and cross-scale coupling are only approximate, and are derived from other simpler (and often heuristic) physics. As a result, such parameterisations can vary significantly in their utility, and it is not uncommon that they lead to biases in their predictions (e.g. Pathak et al., 2019; Hyder et al., 2018; Scaife et al., 2010; Li et al., 2019). Developing parameterisations which accurately capture small-scale phenomena within large-scale models is of primary importance to meteorologists since one of the most common source of errors in weather and climate predictions stem from inaccuracies introduced at the unresolved scales (Hamill and Whitaker, 2005; Janjić and Cohn, 2006; Zadra et al., 2018; Bell et al., 2020; Waller et al., 2021).

In this thesis, we investigate the effects of small-scale processes on the propagation of long waves through the ocean and atmosphere using the mathematical theory of homogenisation. The original work presented here consists of two distinct geophysical models examining long waves in a rotating reference frame in the presence of small-scale structures. The first of these, which deals with the shallow water equations in the presence of a small-scale topography is utilised to highlight how significant errors are possible when the effects of a sub-grid structure is implemented in a model using a parameterisation based on the mean value of that variable across a grid cell. Whilst it may be argued that the model itself is more directly relevant to studying ocean waves over a rough-bottomed seabed, the implications of the study carry across to the atmospheric situation with ease, since many convective parameterisations are based upon horizontally averaged mass fluxes (see e.g. Gregory, 2002). Furthermore, the analogy between this problem, and the propagation of waves in a stratified atmosphere, where the topography represents regions of reduced stratification is also discussed.

The second body of original work extends the results to a stratified atmosphere in the presence of small-scale convective circulations driven by localised heat sources. The method of homogenisation is once again utilised, and the effects of convection on the propagation of long waves is examined. Importantly, it is shown how a rigorous asymptotic approach may be used to represent sub-grid scale convection in large-scale atmospheric models with direct implications for building accurate parameterisations in the future. The results indicate that small-scale convective clouds act to vertically redistribute the profiles of horizontal momentum and buoyancy through non-local integral operators, and may be quantified in large-scale models through the use of *transilient kernels*.

Homogenisation theory and geophysical fluid dynamics (GFD) come from different ends of the "mathematical spectrum" so to speak, with homogenisation having its foundation in functional analysis and the theory of partial differential equations, and GFD being heavily influenced by physics and the applied sciences. For this reason, the thesis begins in chapter 2 by introducing the fundamental principles for each. Firstly, in section 2.1, the theory of homogenisation is introduced along with some key results and examples. In particular, this section focusses on homogenising the classical wave equation with a rapidly varying local wave speed. The main results from GFD which relate to large-scale wave propagation are then introduced in section 2.2. In chapter 3 the method of homogenisation as a means to study geophysical wave behaviour is investigated by way of homogenising the rotating shallow water equations in the presence of a small-scale topography. Chapter 4 extends these results to the study of wave propagation in a stratified atmosphere in the presence of small-scale convective clouds. Finally, in chapter 5, conclusions are drawn. Much of the overtly technical mathematics is relegated to the appendices, which may be found at the end of the thesis.

Chapter 2

Homogenisation & rotating flows - the basics

This chapter is devoted to introducing the mathematical concepts which underlie the rest of the thesis. The topics covered fall into two broad categories, namely *the method of homogenisation* to which section 2.1 is devoted, and *waves in a rotating fluid*, which is discussed in section 2.2.

2.1 The method of homogenisation

The method of homogenisation is an example of a well-established, rigorous mathematical theory with motivations which span numerous fields of study within the physical sciences. In essence, homogenisation is a method of averaging which may be applied to highly heterogeneous problems - that is, problems which vary on two (or more) disparate spatial scales. Such problems are often characterised by partial differential equations with rapidly varying coefficients, which, through the method of homogenisation are ‘replaced’ by homogeneous (or ‘effective’) coefficients. These effective coefficients are determined through a multiple-scale analysis which implicitly couples the small- and large-scales present in the problem, and in some sense act like averaged properties of the medium which they describe.

Whilst it is true that much of the rigorous mathematical justification for homogenisation has been developed in the latter half of the 20th century, problems of this nature date back at least as far as 1892 with Lord Rayleigh’s study of conduction through a composite material (Rayleigh, 1892). Since then much attention has been given to problems of this sort across a wide range of disciplines, including material science (e.g. Hassani and Hinton, 1999; Guedes and Kikuchi, 1990; Briane and Camar-Eddine, 2007; Pastukhova, 2005), optics (e.g. Mottin et al., 2011; McPhedran et al., 1988; Felbacq, 2016) and fluid flow through porous media (Chamsri, 2013; Daly and Roose, 2015) and on the planetary scale (e.g. Mei, 1985; Mei and Vernescu, 2010; Vanneste, 2000a,b; Benilov, 2000). In many introductory texts, the method of homogenisation is discussed in the context of elliptic PDEs; however, as we are ultimately interested in the propagation of waves, it is more relevant for our interests to introduce the theory as it applies to the hyperbolic wave equation. Whilst there do exist subtle differences between the elliptic and hyperbolic cases (and indeed the parabolic case), they will not be relevant to our mathematical treatment. However, the interested reader is referred to Brahim-Otsmane et al. (1992), Cioranescu and Donato (1999) §12 or Papanicolau et al. (1978) Ch.2 §3 for a more thorough discussion.

The layout of this chapter is as follows. In section 2.1.1 the problem of homogenising the classical wave equation is set up, and the main aims of the procedure are outlined. The formal asymptotics are then carried out in section 2.1.1.1 for the case where the spatial dimension $d \geq 2$, and the homogenised equation along with the cell problem are derived. In section 2.1.1.2 an important property of the homogenised coefficient is discussed. Finally, in section 2.1.2 an example problem is given in order to highlight the main points.

2.1.1 The classical wave equation

As an introduction, the canonical problem of homogenising the classical wave equation is reviewed. Consider the second-order, hyperbolic, initial-boundary value problem

$$
\begin{aligned}
\partial^2_{tt}\phi^\varepsilon - \nabla\cdot(A^\varepsilon\nabla\phi^\varepsilon) &= 0, \quad \text{for} \quad (\boldsymbol{x},t)\in\Omega\times(0,T),\\
\phi^\varepsilon(\boldsymbol{x},0) &= a(\boldsymbol{x}), \quad \text{for} \quad \boldsymbol{x}\in\Omega,\\
\phi^\varepsilon_t(\boldsymbol{x},0) &= b(\boldsymbol{x}), \quad \text{for} \quad \boldsymbol{x}\in\Omega,\\
\phi^\varepsilon &= c(\boldsymbol{x},t), \quad \text{for} \quad (\boldsymbol{x},t)\in\partial\Omega\times(0,T),
\end{aligned}
\tag{2.1}
$$

where the scalar quantity $A^\varepsilon = A^\varepsilon(\boldsymbol{x})$ is uniformly bounded away from zero, and where $\Omega\subset\mathbb{R}^d$ is an open connected subset of d-dimensional Euclidean space, with a smooth boundary $\partial\Omega$. The initial data $a(\boldsymbol{x}), b(\boldsymbol{x})$ and boundary data $c(\boldsymbol{x},t)$ are also taken to be uniformly bounded functions. The key characteristic of the system (2.1) which motivates the method of homogenisation is the dependence of $A^\varepsilon(\boldsymbol{x})$, and $\phi^\varepsilon(\boldsymbol{x},t)$ on ε where $\varepsilon \ll 1$ is a small parameter. Indeed, the coefficient A^ε (which in the context of the wave equation may be identified with the square of the wave speed) is assumed to be of the form

$$
A^\varepsilon(\boldsymbol{x}) = A(\boldsymbol{x},\boldsymbol{X}), \tag{2.2}
$$

where $\boldsymbol{X} = \boldsymbol{x}/\varepsilon$. That is, it depends on two spatial scales - a ‘large’ $O(1)$ scale, characterised by the variable $\boldsymbol{x}$, and a ‘small’ $O(\varepsilon)$ scale, characterised by the variable $\boldsymbol{X}$. Importantly, though these two spatial variables both depend on $\boldsymbol{x}$, they are treated as independent from one another due to the large scale-separation between them in the limit $\varepsilon\to 0$. The rigorous justification of this treatment is one of the canonical problems in homogenisation theory (see, e.g Allaire, 1992; Pavliotis and Stuart, 2008, Ch. 19).

The general idea behind the method of homogenisation is to replace the highly *heterogeneous* quantities $A^\varepsilon(\boldsymbol{x})$ and $\phi^\varepsilon(\boldsymbol{x},t)$ with corresponding *homogeneous* quantities $\boldsymbol{A}_{\text{eff}}(\boldsymbol{x})$ and $\hat{\phi}(\boldsymbol{x},t)$, such that in the limit of infinitely small inhomogeneities ($\varepsilon \to 0$), the system (2.1) converges to

$$\begin{aligned} \partial_{tt}^2 \hat{\phi} - \nabla \cdot (\boldsymbol{A}_{\text{eff}} \nabla \hat{\phi}) &= 0, \quad \text{for} \quad (\boldsymbol{x}, t) \in \Omega \times (0, T), \\ \hat{\phi}(\boldsymbol{x}, 0) &= a(\boldsymbol{x}), \quad \text{for} \quad \boldsymbol{x} \in \Omega, \\ \hat{\phi}_t(\boldsymbol{x}, 0) &= b(\boldsymbol{x}), \quad \text{for} \quad \boldsymbol{x} \in \Omega, \\ \hat{\phi} &= c(\boldsymbol{x}, t), \quad \text{for} \quad (\boldsymbol{x}, t) \in \partial\Omega \times (0, T). \end{aligned} \tag{2.3}$$

Importantly, the homogenised problem (2.3) does not explicitly depend on the small spatial structure, but rather contains the homogenised (or *effective*) matrix coefficient $\boldsymbol{A}_{\text{eff}}$ which implicitly couples the small- and large-scales. This coupling is found by solving an elliptic PDE over the small-scale, which is usually referred to as the ‘cell problem’. In the following section, we will explicitly derive the homogenised system (2.3), and its corresponding cell problem in the specific case where A is assumed to be a periodic function of the small-scale variables. Rigorous proofs of the convergence of the asymptotic treatment may be found in the literature (e.g. Colombini and Spagnolo, 1978; Brahim-Otsmane et al., 1992; Francfort and Murat, 1992; Pavliotis and Stuart, 2008, Ch. 7), however the approach taken here is somewhat more heuristic and follows roughly the same outline as that of Holmes (2012) §5 or Allaire (2012) as applied to the Poisson equation.

Note, that the following procedure may be carried out in any dimension $d \geq 2$ without any significant change, however the one-dimensional ($d = 1$) case is treated somewhat differently, and will be discussed separately.

2.1.1.1 Homogenisation procedure

In this section, the formal homogenisation procedure for the problem (2.1) is carried out. For the sake of simplicity, we take $d = 2$, since the same procedure is followed for any higher dimension. The $d = 1$ case however is different enough to merit its own treatment, and is addressed separately in the next section. Thus, for the remainder of this section, $\boldsymbol{x} = (x, y)$ is a two-dimensional vector, and correspondingly, $\nabla = (\partial_x, \partial_y)$ is the two-dimensional gradient operator.

First of all, it is important to make some assumptions about the coefficient

$A(\boldsymbol{x}, \boldsymbol{X})$. One such assumption which is commonplace in homogenisation theory is to assume that A is periodic on the small-scale. That is, there exist linearly independent vectors $\boldsymbol{X}_p^{(1)}, \boldsymbol{X}_p^{(2)}$ such that

$$A(\boldsymbol{x}, \boldsymbol{X} + \boldsymbol{X}_p^{(i)}) = A(\boldsymbol{x}, \boldsymbol{X}) \quad \text{for} \quad i = 1, 2, \tag{2.4}$$

for all values of $\boldsymbol{x}$ and $\boldsymbol{X}$ in the domain Ω. Under such an assumption, the domain adopts a lattice type structure, with each cell in the lattice denoted by Ω_p being a parallelogram. As a result of this, it must be true that knowledge of the small-scale structure of a quantity across an entire cell, gives the small-scale structure across the entire domain by extension.

Recalling that $\boldsymbol{x}$ and $\boldsymbol{X}$ are to be treated independently, using the chain rule allows the gradient operator to be expanded according the the multi-scale formalism as

$$\nabla \longrightarrow \nabla_{\boldsymbol{x}} + \frac{1}{\varepsilon}\nabla_{\boldsymbol{X}}, \tag{2.5}$$

where the subscripts denote which variables the gradient operator acts upon. Substituting this into equation (2.1) leads to

$$\begin{aligned}(\nabla_{\boldsymbol{X}} + \varepsilon\nabla_{\boldsymbol{x}}) \cdot \left[A(\boldsymbol{x}, \boldsymbol{X}) \left(\nabla_{\boldsymbol{X}} + \varepsilon\nabla_{\boldsymbol{x}}\right) \phi^\varepsilon\right] &= \varepsilon^2 \partial_{tt}^2 \phi^\varepsilon, \quad \text{for} \quad \boldsymbol{x} \in \Omega \times (0, T),\\ \phi^\varepsilon(\boldsymbol{x}, 0) &= a(\boldsymbol{x}), \quad \text{for} \quad \boldsymbol{x} \in \Omega,\\ \phi_t^\varepsilon(\boldsymbol{x}, 0) &= b(\boldsymbol{x}), \quad \text{for} \quad \boldsymbol{x} \in \Omega,\\ \phi^\varepsilon &= c(\boldsymbol{x}, t), \quad \text{for} \quad \boldsymbol{x} \in \partial\Omega \times (0, T).\end{aligned} \tag{2.6}$$

Since equations (2.6) contain the small parameter ε, and because the coefficient A is a periodic function of $\boldsymbol{X}$, it is reasonable to seek a solution for ϕ^ε in the form of a regular perturbation expansion given by

$$\phi^\varepsilon(\boldsymbol{x}) = \phi_0(\boldsymbol{x}, \boldsymbol{X}) + \varepsilon\phi_1(\boldsymbol{x}, \boldsymbol{X}) + \varepsilon^2\phi_2(\boldsymbol{x}, \boldsymbol{X}) + \cdots \tag{2.7}$$

where each ϕ_i $(i = 0, 1, 2, \ldots)$ is periodic in $\boldsymbol{X}$. Substituting this ansatz into (2.6), and equating terms at each order in ε, leads to a hierarchy of equations. At $O(1)$, the leading order PDE is given by

$$\nabla_{\boldsymbol{X}} \cdot (A \nabla_{\boldsymbol{X}} \phi_0) = 0, \quad \text{for} \quad \boldsymbol{x} \in \Omega \times (0, T). \tag{2.8}$$

The general solution to this equation which is bounded over Ω, and which satisfies the boundary and initial conditions is

$$\phi_0 = \phi_0(\boldsymbol{x}, t), \quad \text{on} \quad \boldsymbol{x} \in \Omega \times (0, T), \tag{2.9}$$

with

$$\begin{aligned} \phi_0(\boldsymbol{x}, 0) &= a(\boldsymbol{x}), \quad \text{for} \quad \boldsymbol{x} \in \Omega, \\ \phi_{0t}(\boldsymbol{x}, 0) &= b(\boldsymbol{x}), \quad \text{for} \quad \boldsymbol{x} \in \Omega, \\ \phi_0 &= c(\boldsymbol{x}, t), \quad \text{for} \quad \boldsymbol{x} \in \partial\Omega \times (0, T). \end{aligned} \tag{2.10}$$

That is, the leading order field is independent of the small-scale variations, and satisfies the inhomogenenous boundary conditions and initial conditions. The fact that the only solution satisfying (2.8) is a function of $\boldsymbol{x}$ only, is closely related to the fact that the only bounded solutions of Laplace's equation over $\mathbb{R}^2$ are constants - a result known as 'the maximum principle' (Pavliotis and Stuart, 2008, §7.2.4; Holmes, 2012, §5.3.2). Note that these boundary and initial conditions are those required for the homogenised equations since they are now independent of ε, and hence from this point forward, only the PDE in (2.6) needs to be considered.

At $O(\varepsilon)$, we have

$$\nabla_{\boldsymbol{X}} \cdot (A \nabla_{\boldsymbol{X}} \phi_1) = -\nabla_{\boldsymbol{X}} A \cdot \nabla_{\boldsymbol{x}} \phi_0. \tag{2.11}$$

This is a linear, elliptic equation which must be solved in order to determine ϕ_1, where the right-hand side depends on $\nabla_{\boldsymbol{x}} \phi_0$ (a function with spatial dependence on $\boldsymbol{x}$ only). Furthermore, it suffices to solve ϕ_1 across only the cell, and then to extend its solution to the whole domain by periodic extrapolation. Therefore, the general solution may be written as the linear combination

$$\phi_1(\boldsymbol{x}, \boldsymbol{X}, t) = \boldsymbol{\xi}(\boldsymbol{x}, \boldsymbol{X}) \cdot \nabla_{\boldsymbol{x}} \phi_0 + d(\boldsymbol{x}, t), \tag{2.12}$$

where $\boldsymbol{\xi} = (\xi_1, \xi_2)^T$ is periodic, with components satisfying

$$\nabla_{\boldsymbol{X}} \cdot (A \nabla_{\boldsymbol{X}} \xi_i) = -\partial_{X_i} A, \quad \text{for} \quad i = 1, 2, \tag{2.13}$$

and where $d(\boldsymbol{x}, t)$ is an arbitrary function which is independent of the small-scale variables. Equation (2.13) is known as the 'cell problem'.

Finally, at $O(\varepsilon^2)$

$$\nabla_{\boldsymbol{X}} \cdot (A \nabla_{\boldsymbol{X}} \phi_2 + A \nabla_{\boldsymbol{x}} \phi_1) + \nabla_{\boldsymbol{x}} \cdot (A \nabla_{\boldsymbol{X}} \phi_1) + \nabla_{\boldsymbol{x}} \cdot (A \nabla_{\boldsymbol{x}} \phi_0) = \partial_{tt}^2 \phi_0. \tag{2.14}$$

Fortunately, it is not necessary to solve this equation, and instead the periodicity of the problem on the small-scale may be exploited so that the homogenised system emerges out of a 'solvability condition'. For this purpose, a cell-average operator $\langle \cdot \rangle$ is introduced, which is defined to act upon a function $g(\boldsymbol{x}, \boldsymbol{X}, t)$ as

$$\langle g \rangle(\boldsymbol{x}, t) = \frac{1}{|\Omega_p|} \int_{\Omega_p} g(\boldsymbol{x}, \boldsymbol{X}, t) \, \mathrm{d}\boldsymbol{X}, \tag{2.15}$$

where in two dimensions $|\Omega_p|$ is the area of the cell. Applying this operator to equation (2.14) allows some simplifications to be made. Assuming suitable smoothness properties for A, the divergence theorem may be used to find

$$\begin{aligned} \int_{\Omega_p} \nabla_{\boldsymbol{X}} \cdot (A \nabla_{\boldsymbol{X}} \phi_2 + A \nabla_{\boldsymbol{x}} \phi_1) \, \mathrm{d}\boldsymbol{X} = \\ \int_{\partial \Omega_p} \hat{\boldsymbol{n}} \cdot (A \nabla_{\boldsymbol{X}} \phi_2 + A \nabla_{\boldsymbol{x}} \phi_1) \, \mathrm{d}S = 0, \end{aligned} \tag{2.16}$$

where the second equality is due to the periodicity of the functions A, ϕ_1, ϕ_2 over the cell. Furthermore, we recall that from (2.9), ϕ_0 is independent of $\boldsymbol{X}$, and hence

$\langle \phi_0 \rangle = \phi_0$. Therefore, the cell-averaged PDE is given by

$$\nabla_{\boldsymbol{x}} \cdot \left[\langle A \rangle \nabla_{\boldsymbol{x}} \phi_0 + \langle A \nabla_{\boldsymbol{X}} \phi_1 \rangle \right] = \partial_{tt}^2 \phi_0. \tag{2.17}$$

Now, all that is left to do is to use the expression (2.12) to simplify the second term in the brackets, which yields the homogenised PDE

$$\partial_{tt}^2 \phi_0 - \nabla \cdot \left(\boldsymbol{A}_{\text{eff}} \nabla \phi_0 \right) = 0, \quad \text{for} \quad (\boldsymbol{x}, t) \in \Omega \times (0, T), \tag{2.18}$$

where the 2×2 matrix $\boldsymbol{A}_{\text{eff}}$ is given by

$$\boldsymbol{A}_{\text{eff}}(\boldsymbol{x}) = \begin{pmatrix} \langle A \rangle + \langle A \partial_{X_1} \xi_1 \rangle & \langle A \partial_{X_1} \xi_2 \rangle \\ \langle A \partial_{X_2} \xi_1 \rangle & \langle A \rangle + \langle A \partial_{X_2} \xi_2 \rangle \end{pmatrix}. \tag{2.19}$$

Equation (2.18) combined with the boundary and initial conditions (2.10) retrieves the system (2.3) where the homogeneous quantity $\hat{\phi}$ is given by ϕ_0.

A special case of this result is found when the cell has fourfold symmetry. In this situation the off-diagonal terms in (2.19) vanish, and the diagonal elements are equal, so that

$$\boldsymbol{A}_{\text{eff}}(\boldsymbol{x}) = c_{\text{eff}}^2(\boldsymbol{x}) \boldsymbol{\mathcal{I}}, \tag{2.20}$$

where $\boldsymbol{\mathcal{I}}$ is the 2×2 identity matrix. In this case, the wave equation becomes

$$\partial_{tt}^2 \phi_0 - \nabla_{\boldsymbol{x}} \cdot \left(c_{\text{eff}}^2 \nabla_{\boldsymbol{x}} \phi_0 \right) = 0, \tag{2.21}$$

where the quantity $c_{\text{eff}}(\boldsymbol{x})$ is recognisable as the homogenised wave speed.

2.1.1.2 Reuss–Voigt bounds

Now that the homogenised equations have been derived, an important property of the effective coefficient $\boldsymbol{A}_{\text{eff}}$ is discussed. Often in the theory of homogenisation, the precise value of the effective coefficient cannot be found explicitly, and mathematicians would rather be able to estimate its value by finding upper and lower bounds. One of the simplest pair of bounds are known as the Reuss–Voigt bounds, attributed to (Reuss, 1929) and (Voigt, 1928), and are well known in the literature (see e.g. Allaire, 2012; Nandakumaran, 2007; Mei and Vernescu, 2010, §5.5).

Let λ_i for $i = 1, 2$ be the eigenvalues of $\boldsymbol{A}_{\text{eff}}$, then they satisfy

$$\langle A^{-1} \rangle^{-1} \leq \lambda_i \leq \langle A \rangle. \tag{2.22}$$

The lower (Reuss) bound is the harmonic mean of the coefficient over the cell, and the upper (Voigt) bound, the arithmetic mean. The proof of this fact comes from rewriting the effective coefficient as the solution to a variational problem, of which the cell problem is the Euler-Lagrange equation, and can be found for example in Allaire (2012). Consequently, the case in which the cell has fourfold symmetry and $\boldsymbol{A}_{\text{eff}} = A_{\text{eff}} \boldsymbol{\mathcal{I}}$ leads to

$$\langle A^{-1} \rangle^{-1} \leq A_{\text{eff}} \leq \langle A \rangle. \tag{2.23}$$

The Reuss–Voigt bounds can be each realised in specific situations. Indeed, the only case in which $A_{\text{eff}} = \langle A \rangle$ is the trivial case in which A is constant with respect to the small-scale. It is worth emphasising this point, since the most ‘obvious’ approach to finding an averaged set of equations may well be to simply take the arithmetic mean of A, whereas this, in fact, is never the ‘correct’ average when there is a small-scale structure. On the other hand, $A_{\text{eff}} = \langle A^{-1} \rangle^{-1}$ is only achieved in the one-dimensional problem, which will be the focus of the next section.

2.1.1.3 The one-dimensional case

The one-dimensional case leads to an important simplification. Consider now the one-dimensional counterpart of the system (2.1), so that

$$\begin{aligned} &\frac{\partial^2 \phi^\varepsilon}{\partial t^2} - \frac{\partial}{\partial x}\left(A^\varepsilon \frac{\partial \phi^\varepsilon}{\partial x} \right) = 0, \quad \text{for} \quad (x,t) \in (\alpha, \beta) \times (0, T), \\ &\phi^\varepsilon(x, 0) = a(x), \quad \phi^\varepsilon_t(x, 0) = b(x), \quad \text{for} \quad x \in (\alpha, \beta), \\ &\phi^\varepsilon(\alpha, t) = c_1(t), \quad \phi^\varepsilon(\beta, t) = c_2(t), \quad \text{for} \quad t \in (0, T). \end{aligned} \tag{2.24}$$

It is again assumed that $A^{\varepsilon}(x)$ may be written

$$A^{\varepsilon}(x) = A(x, X), \tag{2.25}$$

where $X = x/\varepsilon$, and that there exists a constant X_p such that

$$A(x, X + X_p) = A(x, X), \tag{2.26}$$

so that A is periodic on the small-scale. The homogenisation procedure broadly follows that of the previous section, with the resulting homogenised PDE given by

$$\frac{\partial^2 \phi_0}{\partial t^2} - \frac{\partial}{\partial x}\left(A_{\text{eff}} \frac{\partial \phi_0}{\partial x}\right) = 0, \quad \text{for} \quad (x, t) \in (\alpha, \beta) \times (0, T). \tag{2.27}$$

The main difference here, is that the effective coefficient $A_{\text{eff}}(x)$ is simply a scalar function of the large-scale spatial variable as opposed to a matrix, and is given by

$$\begin{aligned} A_{\text{eff}}(x) &= \left\langle A\left(1 + \frac{\partial \xi}{\partial X}\right)\right\rangle \\ &= \frac{1}{X_p}\int_0^{X_p} A(x, X)\left(1 + \frac{\partial \xi}{\partial X}(x, X)\right)\,\mathrm{d}X. \end{aligned} \tag{2.28}$$

The scalar quantity $\xi(x, X)$ is the solution to the one dimensional cell problem

$$\begin{aligned} \frac{\partial}{\partial X}\left(A\frac{\partial \xi}{\partial X}\right) &= -\frac{\partial A}{\partial X}, \quad \text{for} \quad X \in (0, X_p), \\ \xi(x, 0) &= \xi(x, X_p), \end{aligned} \tag{2.29}$$

which is exactly solvable.

Integrating (2.29) once with respect to X gives

$$A(x, X)\left(1 + \frac{\partial \xi}{\partial X}\right) = k_1(x), \tag{2.30}$$

where $k_1(x)$ is a function of the large-scale variable only. In fact, it can be immediately seen that applying the averaging operator to equation (2.30) leads to

$$k_1(x) = A_{\text{eff}}(x). \tag{2.31}$$

Integrating (2.30) once more, gives

$$\xi(x, X) = -X + A_{\text{eff}}(x) \int_0^X \frac{1}{A(x, Z)} \, \mathrm{d}Z + k_2(x), \tag{2.32}$$

where $k_2(x)$ is another constant of integration, and applying the periodic cell-boundary conditions, it is deduced that

$$A_{\text{eff}}(x) = \langle A^{-1} \rangle^{-1}. \tag{2.33}$$

That is, the effective coefficient is given by the harmonic mean of $A(x)$, achieving equality with the lower (Reuss) bound of possible coefficients determined by (2.23).

In deriving this result for the one dimensional case, it was assumed that A is periodic on the small-scale. However, it may be shown with some extra work that this requirement can be lifted completely, and that in fact the presence of any small-scale structure, periodic or not, leads formally to the same result (Holmes, 2012, §5.2). The process of generalising the result to the non-periodic case requires only that $A(x, X)$ be finite, and bounded away from zero, and that the cell-averaging operator $\langle \cdot \rangle$ be replaced by the operator $\langle \cdot \rangle_\infty$ which acts upon a function $g(x, X)$ as

$$\langle g \rangle_\infty(x) = \lim_{X \to \infty} \left(\frac{1}{X} \int_0^X g(x, Z) \, \mathrm{d}Z \right). \tag{2.34}$$

Furthermore, since there is no periodic cell structure to exploit in this case, the $O(\varepsilon^2)$ equation must be solved to determine ϕ_2. In the one dimensional case this is achieved with little difficulty, and the homogenised system (2.27) is retrieved. We note that for a random coefficient, this result is strictly formal, and applies only in the long wavelength limit. For shorter wavelengths, scattering and localisation leads to situations in which waves may propagate only across small portions of the domain (see e.g. Van Der Baan, 2001; Sheng et al., 1986; Figotin and Klein, 1997;

Figotin and Gorentsveig, 1998).

2.1.2 An example problem

In order to demonstrate the efficacy of the homogenisation method an example model problem is investigated. Consider the wave equation (2.1) in a semi-infinite periodic channel of width π centred on $y = 0$, and bounded by side walls at $y = -\pi/2, \pi/2$. It is assumed that the solutions are periodic in time and hence can be written in the form

$$\phi^{\varepsilon}(\boldsymbol{x}, t) = \tilde{\phi}^{\varepsilon}(\boldsymbol{x}) \exp(-\mathrm{i}\omega t), \tag{2.35}$$

where ω is the wave frequency. It is further assumed that the channel is periodic, with period 2π in the x-direction, and that the channel walls are equipped with homogeneous Dirichlet boundary conditions. Thus, the problem is given by

$$\begin{aligned} \nabla \cdot (A^{\varepsilon} \nabla \phi^{\varepsilon}) = -\omega^2 \phi^{\varepsilon}, &\quad \text{for} \quad (x, y) \in (0, 2\pi) \times (-\pi/2, \pi/2), \\ \phi^{\varepsilon} = 0, &\quad \text{on} \quad y = -\pi/2, \pi/2, \\ \phi^{\varepsilon}(0, y) = \phi^{\varepsilon}(2\pi, y), &\quad \text{for} \quad y \in (-\pi/2, \pi/2). \end{aligned} \tag{2.36}$$

Relative to the channel, the periodic cell is a square of side length $2\pi\varepsilon$, so that the values the small-scale variables take are confined to the square $\boldsymbol{X} \in (-\pi, \pi) \times (-\pi, \pi)$. The coefficient $A(\boldsymbol{X})$, chosen to be independent of the large-scale, is given by a symmetric Gaussian profile

$$A(\boldsymbol{X}) = 1 - \frac{1}{2} \exp\left(-\frac{1}{2}|\boldsymbol{X}|^2\right). \tag{2.37}$$

It should be noted that A is not strictly smooth across the cell boundary as is formally required, however since the Gaussian decays rapidly as the cell boundary is approached, it is 'smooth enough' for numerical experiments. The quantity ε is identified as

$$\varepsilon = \frac{L_c}{L_x} \equiv \frac{1}{n}, \tag{2.38}$$

where L_c is the cell side length, L_x is the width of the channel, and n is the number of cells distributed along the length of one period of the channel.

Note, that from the form of (2.37), and the fact that the periodic cell is square in shape means that the problem has a four-fold symmetry. Furthermore, since $A(\boldsymbol{X})$ is independent of $\boldsymbol{x}$ we should expect the homogenised PDE to be of the form (2.21), where the effective wave speed c_{eff} is a constant. Thus, the homogenised system is given by

$$\begin{aligned} c_{\text{eff}}^2 \nabla_{\boldsymbol{x}}^2 \phi_0 &= -\omega^2 \phi_0, \quad \text{for} \quad (x,y) \in (0,2\pi) \times (-\pi/2, \pi/2), \\ \phi_0 &= 0, \quad \text{on} \quad y = -\pi/2, \pi/2, \\ \phi_0(0,y) &= \phi_0(2\pi, y), \quad \text{for} \quad y \in (-\pi/2, \pi/2). \end{aligned} \tag{2.39}$$

This is a straightforward eigenvalue problem which can be solved in order to determine the discrete set of eigenvectors $\phi_{0,\boldsymbol{k}}$ and corresponding eigenvalues $-\omega_{\boldsymbol{k}}^2$, where $\boldsymbol{k} = (k,l)$ is the two-dimensional wave vector with k, l both taking integer values. By first numerically solving the cell problem (2.13) using a Fourier spectral method (see e.g. Trefethen, 2000, Ch. 3) determining the constant c_{eff}^2, standard numerical or analytical methods may be implemented to find the set of solutions to (2.39). In particular, the eigenvalue corresponding to $\boldsymbol{k} = (1,1)$ is focussed on, and denoted by $-\omega_{\text{hom}}^2$.

Next, the full eigenvalue problem (2.36) is solved numerically. Importantly, the dependence of the problem on the cell parameter ε allows a discrete set of problems to be solved. That is, for each value of $n = 4, 6, 8, ...$ the cell-parameter takes discrete values $\varepsilon_n = 1/4, 1/6, 1/8, ...$ each of which corresponds to a version of (2.36) where the channel is divided into $n^2/2$ cells. For each of these problems, the set of eigenvectors and eigenvalues may be found numerically, so that again focussing on the $\boldsymbol{k} = (1,1)$ solutions, a sequence of eigenvalues denoted by $-\omega_n^2$ is obtained.

Figure 2.1 demonstrates the fundamental result of the homogenisation procedure - the convergence of the solution of (2.36) to that of the homogenised system

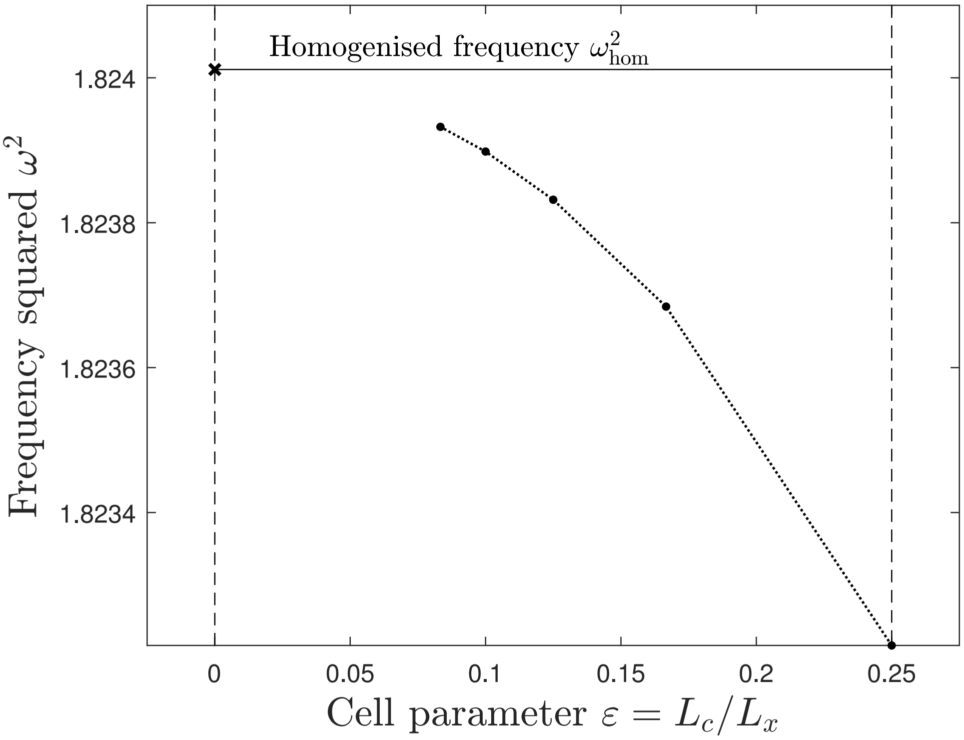

Figure 2.1: The squared frequencies corresponding to wave vector $\boldsymbol{k} = (1, 1)$ calculated from the eigenvalue problems (2.36) and (2.39). Shown at the discrete points $\varepsilon_n = 1/n$ for $n = 4, 6, 8, 10, 12$ are the terms of the sequence ω_n^2 (black dots), and at $\varepsilon = 0$, the quantity ω^2_{hom} (black cross). Also shown is a piecewise linear interpolant (dotted line).

(2.39). Indeed, it is clear that as $\varepsilon \to 0$, the sequence $\{\omega_n^2\}$ converges to ω^2_{hom}, albeit in increasingly small steps as the number of cells is increased. This is a particularly powerful result as solving the full problem requires a significant amount of computing power due to the 'roughness' of the parameter A^ε for small ε. This means that in order to achieve machine precision for even relatively small values of n, many grid-points must be used. Furthermore, achieving precise results for greater values of n than shown becomes increasingly more difficult, as the number of grid-points needed increases nonlinearly - to find ω^2_{12} precisely, 200×201 grid-points were used across the channel. In contrast, calculating ω^2_{hom} comes with little computational difficulty, as the cell problem (2.13) requires relatively few grid-points, with 40×40 points across the cell proving sufficient for machine precision.

2.2 Waves in a rotating fluid

The purpose of this section is to introduce some of the fundamental mathematical and physical principles in geophysical fluid dynamics. Much of the matter presented here would likely be familiar to the reader with an introductory knowledge of the subject, and may be found in most standard textbooks (e.g. Vallis, 2006; Gill, 1982; Pedlosky, 1987; Holton, 2004) in some form. It is, however, worthwhile briefly reviewing some of this standard theory, since in later chapters more complex and unfamiliar concepts will be introduced which build closely upon the techniques given here. In particular, many of the results presented here which pertain to oceans with a flat seabed will be generalised in chapter 3, where topography is introduced, and those pertaining to a stratified atmosphere will be generalised in chapter 4.

The goal here is to gain some intuitive and quantitative understanding of large-scale waves in the ocean and atmosphere. Waves of this sort are a key element in driving the Earth's oceanic and atmospheric circulations, as well as in the formation of many weather patterns and oscillations such as the El Niño–Southern Oscillation and the Madden–Julian Oscillation. Thus, understanding these waves is a vital component in the study of meteorology, climatology and geophysics, and facilitates accurate weather and climate predictions over a vast range of time-scales. In the mid-latitudes, there exist three main waves of interest, namely inertia-gravity, Rossby and Kelvin waves. Inertia-gravity waves (also known as Poincaré waves in the case of a single shallow fluid layer) are oscillations caused by the displacement of a fluid from stable equilibrium where the restoring force is due to a vertical gradient or discontinuity in buoyancy. This may occur either within a vertically stratified fluid such as the troposphere, or at the interface of two fluids with different densities, for example, on the free surface of the ocean which separates the water from the air. Rossby waves (also known as planetary waves) are a particular type of long wave which occur as the ocean or atmosphere is disturbed from geostrophic equilibrium (i.e. when the Coriolis force and pressure gradient are in perfect balance). The fundamental mechanism for their existence is the rotation of the Earth, and the Coriolis force which varies with latitude, as well as the conservation of potential vorticity. Finally, Kelvin waves occur when the Earth's rotation balances the Coriolis force against a waveguide such as a coastline, along which they propagate in one direction.

As a precursor to developing a theory for these waves, it is first necessary to introduce some important geophysical concepts, and thus this chapter is organised as follows. In section 2.2.1 we give the basic equations of motion for an inviscid fluid in a rotating reference frame, from which we derive the shallow water equations in section 2.2.2. In section 2.2.2.1, the notion of potential vorticity, as well as its associated conservation law is discussed. In section 2.2.3, we derive the Boussinesq equations governing the dynamics of a vertically stratified fluid. The Coriolis force is then given a more thorough treatment in section 2.2.4, where we introduce the f-plane and β-plane approximations. In section 2.2.5, the notions of geostrophic balance and quasi-geostrophy are introduced, and the quasi-geostrophic potential vorticity equation is derived. Finally, in section 2.2.6, the dispersion relations for the shallow water Poincaré, Rossby and Kelvin waves in a mid-latitude β-channel are derived, using both numerical and asymptotic techniques.

2.2.1 Governing equations

The equations governing an incompressible, inviscid, fluid of uniform density in a rotating frame, and under the influence of gravity are taken as the starting point for this chapter. From these equations, distinguished limits which apply to both oceanic and atmospheric systems can be derived. Mathematically, the laws governing conservation of horizontal momentum, vertical momentum, and mass are given by

$$\frac{D\boldsymbol{u}}{Dt} + f\boldsymbol{k} \times \boldsymbol{u} = -\frac{1}{\rho}\nabla p, \tag{2.40}$$

$$\frac{Dw}{Dt} = -\frac{1}{\rho}\frac{\partial p}{\partial z} - g, \tag{2.41}$$

$$\nabla \cdot \boldsymbol{u} + \frac{\partial w}{\partial z} = 0, \tag{2.42}$$

where $\boldsymbol{u} = (u, v, 0)^T$ is the horizontal velocity vector, w is the vertical velocity, p is the pressure, and ρ is the density of the fluid. Here, g is the gravitational acceleration (taken to be a constant), and $f = 2\Omega \sin\theta$ is the Coriolis parameter, where Ω is the vertical component of the angular velocity of the Earth, and θ is the spherical coordinate corresponding to latitude. For consistency with later sections of the thesis, the gradient operator $\nabla = (\partial_x, \partial_y, 0)$ is taken to be only the horizontal components of the full three dimensional gradient, and thus the material derivative is written as

$$\frac{D}{Dt} = \frac{\partial}{\partial t} + \boldsymbol{u} \cdot \nabla + w\frac{\partial}{\partial z}. \tag{2.43}$$

2.2.2 Shallow water equations

The derivation of the shallow water equations is a standard exercise, and can be found in any geophysical fluid dynamics textbook (see e.g. Vallis, 2006; Gill, 1982; Pedlosky, 1987). It is however useful to review the result, especially in the case where the resting ocean depth due to topography is not constant, and so we present a derivation here based on these sources. Whilst the name implies that these equations pertain only to the study of the ocean, it is worth noting that the shallow water equations are also of significant importance when studying the atmosphere. Indeed, it could be argued that the atmosphere and ocean have more in common than they do in opposition, since both are in some sense ‘shallow’, and obey the same physical laws. However, the shallow water equations are of interest only when the vertical motions in the fluid are small compared to the horizontal motions.

Consider a single, shallow fluid layer with a constant density ρ. By ‘shallow’, it is meant that the aspect ratio of the layer thickness to the horizontal scale of motions of interest is small. Since density is taken to be a constant, equations (2.40-2.42) are a closed system in 4 variables, and under the prescription of appropriate boundary conditions, fully describe the fluid motion. Let $\eta(\boldsymbol{x}, t)$ describe the free surface elevation above the resting state (at $z = 0$), and let $h(\boldsymbol{x})$ denote the thickness of the fluid at rest. Importantly, the dependence of the layer thickness on the spatial variable implies the presence of a varying bottom topography. Boundary conditions at the free surface $z = \eta(\boldsymbol{x}, t)$ and bottom boundary $z = -h(\boldsymbol{x})$ equate the vertical velocity of the fluid with the material derivative of the surface - that is to say that a fluid element at a boundary must remain on the boundary for all time, or equivalently, that the boundary is a streamline. It is further assumed that the pressure at the free surface is constant, and given by some reference pressure, which may be taken to be 0. Mathematically, these conditions are summarised by

$$w = \frac{D\eta}{Dt} \equiv \frac{\partial \eta}{\partial t} + \boldsymbol{u} \cdot \nabla \eta, \quad \text{on} \quad z = \eta(\boldsymbol{x}, t), \tag{2.44}$$

$$p = 0, \quad \text{on} \quad z = \eta(\boldsymbol{x}, t), \tag{2.45}$$

$$w = \frac{D(-h)}{Dt} \equiv -\boldsymbol{u} \cdot \nabla h, \quad \text{on} \quad z = -h(\boldsymbol{x}). \tag{2.46}$$

Letting $\alpha = L_z/L_x$ be the aspect ratio, where L_z, L_x are typical vertical and horizontal scales in the fluid, an elementary dimensional analysis shows that all terms on the left-hand side in the vertical momentum equation (2.41) are proportional to α^2. Under the shallow water assumption that $\alpha \ll 1$, these terms may be disregarded, leaving only the hydrostatic equation

$$\frac{\partial p}{\partial z} = -g\rho. \tag{2.47}$$

Integrating this between z and $\eta(\boldsymbol{x}, t)$, and applying the condition (2.45) allows the pressure to be determined in terms of the surface elevation, which is simply given by the expression

$$p(\boldsymbol{x}, z, t) = \rho g \left[\eta(\boldsymbol{x}, t) - z\right]. \tag{2.48}$$

Substituting this into the horizontal momentum equation (2.40) gives the equation for conservation of momentum in the shallow water system

$$\frac{D\boldsymbol{u}}{Dt} + f\boldsymbol{k} \times \boldsymbol{u} = -g\nabla\eta, \tag{2.49}$$

where now the material derivative is simply given by

$$\frac{D}{Dt} = \frac{\partial}{\partial t} + \boldsymbol{u} \cdot \nabla \tag{2.50}$$

since the horizontal velocity components are assumed to be independent of z. The system is then closed by integrating the continuity equation between the bottom boundary, and the free surface so that

$$\int_{-h(\boldsymbol{x})}^{\eta(\boldsymbol{x},t)} \nabla \cdot \boldsymbol{u} \, \mathrm{d}z = w(\boldsymbol{x}, -h(\boldsymbol{x}), t) - w(\boldsymbol{x}, \eta(\boldsymbol{x}, t), t) \tag{2.51}$$

$$= -\frac{\partial \eta}{\partial t} - \boldsymbol{u} \cdot \nabla \eta - \boldsymbol{u} \cdot \nabla h, \tag{2.52}$$

where the second equality comes from applying the conditions (2.44) and (2.46). Rearranging this equation, and recalling rules for differentiation under the integration sign (Flanders, 1973), one immediately recovers the equation

$$\frac{\partial \eta}{\partial t} + \nabla \cdot \left(\int_{-h}^{\eta} \boldsymbol{u} \, \mathrm{d}z \right) = 0. \tag{2.53}$$

Again, since $\boldsymbol{u}$ is independent of z, this may be simplified to

$$\frac{\partial \eta}{\partial t} + \nabla \cdot [(\eta + h)\boldsymbol{u}] = 0, \tag{2.54}$$

which combined with equation (2.49) completes the derivation of the shallow water equations.

An important case to consider, is that in which the shallow water equations are linearised about a state of rest. That is, by writing

$$\boldsymbol{u}(\boldsymbol{x}, t) = (0, 0)^T + \boldsymbol{u}'(\boldsymbol{x}, t), \quad \eta(\boldsymbol{x}, t) = 0 + \eta'(\boldsymbol{x}, t), \tag{2.55}$$

where the primed variables are considered to be small perturbations such that any products of primed variables are negligible, equations (2.49) and (2.54) simplify to

$$\frac{\partial \boldsymbol{u}}{\partial t} + f\boldsymbol{k} \times \boldsymbol{u} = -g\nabla \eta, \tag{2.56}$$

$$\frac{\partial \eta}{\partial t} + \nabla \cdot (h\boldsymbol{u}) = 0, \tag{2.57}$$

where the prime notation is immediately dropped for simplicity. These equations, namely ‘the linearised, rotating shallow water equations’, are the starting point for the next chapter in this thesis.

2.2.2.1 Conservation of potential vorticity

The notion of potential vorticity and its associated conservation law was first introduced by Rossby (1936), and since then has become one of the key concepts in geophysical fluid dynamics. Rossby, building upon a theorem concerning circulation by Bjerknes et al. (1898) (see also Thorpe et al., 2003), realised that in a shallow fluid layer, the absolute vorticity of a fluid (the vorticity of the fluid relative to the rotating reference frame plus the vorticity of the Earth) must be proportional to its depth, and that this constant of proportionality, which was termed ‘the potential vorticity’ (Rossby, 1940) was conserved following fluid trajectories. This astute observation allows a single equation governing the potential vorticity to be written, which in many cases allows one to avoid explicit calculations based on the full equations of motion. Here we derive Rossby’s elegant result for a shallow fluid.

Taking the curl of the shallow water momentum equation (2.49) gives the vorticity equation

$$D_t(\zeta + f) + (\zeta + f)\nabla \cdot \boldsymbol{u} = 0, \tag{2.58}$$

where $\zeta = \partial_x v - \partial_y u$ is the vertical component of the relative vorticity of the fluid, and where we have used the fact that f is independent of t. Next, rewriting the continuity equation (2.54) in the form

$$D_t(\eta + h) + (\eta + h)\nabla \cdot \boldsymbol{u} = 0, \tag{2.59}$$

allows the two to be combined by eliminating the quantity $\nabla \cdot \boldsymbol{u}$, to form a single conservation equation given by

$$\frac{D}{Dt}\left(\frac{\zeta + f}{\eta + h}\right) = 0. \tag{2.60}$$

This is known as ‘the potential vorticity equation’, and expresses the fact that the potential vorticity $q = (\zeta + f)/(\eta + h)$ is conserved following fluid paths. This result is of fundamental importance in geophysical fluid dynamics, as it provides significant constraints on wave propagation in a shallow fluid layer. For instance, in a layer of constant thickness, any increase / decrease in the Coriolis parameter f must be accompanied by a decrease / increase in relative vorticity ζ. Likewise, for a constant f, any increase / decrease in depth of the fluid must be accompanied by an increase / decrease in ζ - a concept known as 'vortex stretching'. This constant trade-off between relative vorticity ζ, Coriolis parameter f and layer thickness $h+\eta$ is the driving force behind many large-scale oceanic and atmospheric phenomena, in particular the propagation of Rossby waves, which will be discussed in more detail later on in this chapter.

The linearised version of (2.60) is given by

$$\frac{1}{h}\frac{\partial}{\partial t}\left(\zeta - \frac{f\eta}{h}\right) + \boldsymbol{u}\cdot\nabla\left(\frac{f}{h}\right) = 0. \tag{2.61}$$

This result will be useful in section 2.2.6.2 and later on in chapter 3.

2.2.3 The stratified Boussinesq equations in a rotating frame

The Boussinesq equations are a particularly useful limit of the primitive equations (2.40–2.42) for studying motions in the ocean and atmosphere which rely on the background stratification. Importantly, they take account of small density perturbations about the mean profile, and allow one to study the effects of stratification of the dynamics of a fluid. Here, we outline the basic principles of the Boussinesq approximation based on textbook derivations which may be found in e.g. Vallis (2006), Gill (1982), Olbers et al. (2012) etc.

Firstly, we decompose the density into a mean background profile, and small perturbations as

$$\rho = \rho_0 + \overline{\rho}(z) + \rho'(\boldsymbol{x}, z, t), \tag{2.62}$$

where the background density profile consists of a constant ρ_0, and small vertical variations $\overline{\rho}(z)$. The terms are ordered as

$$|\rho'| \ll |\overline{\rho}| \ll |\rho_0|. \tag{2.63}$$

Correspondingly, pressure is decomposed as

$$p = p_0(z) + \overline{p}(z) + p'(\boldsymbol{x}, z, t), \tag{2.64}$$

where the background variables are chosen to satisfy the hydrostatic balance relations

$$\frac{dp_0}{dz} = -g\rho_0, \qquad \frac{d\overline{p}}{dz} = -g\overline{\rho}. \tag{2.65}$$

Substitution of these expansions into (2.40) and neglecting density variations gives the horizontal momentum equation

$$\frac{D\boldsymbol{u}}{Dt} + f\boldsymbol{k} \times \boldsymbol{u} = -\nabla\left(\frac{p'}{\rho_0}\right). \tag{2.66}$$

In the vertical momentum equation, slightly more work must be done. Here, we assume that density fluctuations are negligible except when multiplied by the gravitational acceleration g (which is a large quantity). This is known as the Boussinesq approximation. Substituting the expansions into (2.41) and applying the relations (2.65), we find that to a good approximation

$$\frac{Dw}{Dt} = -\frac{\partial}{\partial z}\left(\frac{p'}{\rho_0}\right) - g\frac{\rho'}{\rho_0}. \tag{2.67}$$

Whilst the continuity equation remains unchanged at leading order, a further equation for ρ' is needed in order to close the system. Such an equation is found from the equation of state

$$\frac{D\rho}{Dt} = \dot{q}, \tag{2.68}$$

where $\dot{q}$ is a source term. Inserting (2.62), and multiplying by $-g/\rho_0$ gives

$$\frac{D}{Dt}\left(-\frac{g\rho'}{\rho_0}\right) - \frac{g}{\rho_0}\frac{d\overline{\rho}}{dz}w = \dot{Q}, \tag{2.69}$$

where $\dot{Q} = -g\dot{q}/\rho_0$. This completes the derivation of the Boussinesq equations.

Introducing the variables

$$p = \frac{p'}{\rho_0}, \quad b = -g\frac{\rho'}{\rho_0}, \tag{2.70}$$

(where we are reusing the notation p to represent scaled pressure perturbations), as well as the 'buoyancy frequency'

$$N^2 = -\frac{g}{\rho_0}\frac{d\overline{\rho}}{dz}, \tag{2.71}$$

(also known as the Brunt–Väisälä frequency) then allows the Boussinesq equations to be written conveniently as

$$\frac{D\boldsymbol{u}}{Dt} + f\boldsymbol{k} \times \boldsymbol{u} = -\nabla p, \tag{2.72}$$

$$\frac{Dw}{Dt} = -\frac{\partial p}{\partial z} + b, \tag{2.73}$$

$$\nabla \cdot \boldsymbol{u} + \frac{\partial w}{\partial z} = 0, \tag{2.74}$$

$$\frac{Db}{Dt} + N^2 w = \dot{Q}. \tag{2.75}$$

A common limit of these equations arises when vertical motions are assumed to be small. Under such an assumption, the material derivative of w disappears from the vertical momentum equation, and we are left with the hydrostatic balance

$$\frac{\partial p}{\partial z} = b. \tag{2.76}$$

The equations with (2.73) replaced by (2.76) are called the hydrostatic Boussinesq equations.

2.2.4 Rotational effects

So far, the quantity f, known as the Coriolis parameter has been treated rather ambiguously, and thus the aim of this subsection is to give a more thorough description of the Coriolis force, and its contribution to the dynamics of geophysical flows. In its most general form, the quantity f is given by

$$f = 2\Omega \sin\theta, \tag{2.77}$$

where Ω is the vertical component of the angular velocity of the Earth, and θ is the spherical coordinate corresponding to latitude. This expression, however, is of little use when considering Cartesian approximations to the primitive (spherical) equations of motion such as (2.40-2.42) due to its complicated dependence on spatial coordinates. Thus, it is standard practice to approximate the Coriolis parameter in such a way that both allows for a simple treatment of rotation in the governing equations, as well as capturing the relevant effects of the Earth's rotation.

One such approximation, known as the 'f-plane' approximation involves treating the Coriolis parameter as a constant, say $f_0 = 2\Omega \sin\theta_0$, where θ_0 is a constant latitude. This approximation has its uses - in particular when studying flows over short length scales where the variations with latitude in the Earth's rotation are negligible. It can however be severely limiting when studying large-scale geophysical flows where important dynamics are found in the latitudinal variations in f. Moreover, when studying motions near the equator (where $f_0 = 0$), the dynamics introduced by the rotation of the Earth are found entirely within the latitudinal variations of f which are absent in the f-plane.

The next most simple approximation which takes account of the latitudinal variations of f is known as the 'β-plane' approximation. By considering small variations θ' about a fixed latitude θ_0, the Coriolis parameter can be approximated as

$$f \approx 2\Omega \sin\theta_0 + 2\Omega\left(\theta' - \theta_0\right)\cos\theta_0. \tag{2.78}$$

This can then be identified with a linear tangent plane approximation for f of the form

$$f(y) \approx f_0 + \beta y, \tag{2.79}$$

where $\beta = df/dy|_{\theta_0} = 2\Omega a^{-1}\cos\theta_0$, a is the Earth's radius, and f_0 is given as before. The β-plane approximation in which f is given by equation (2.79) can be nicely visualised as a tangent plane touching the Earth's surface at the latitude θ_0. Throughout the rest of this thesis, the β-plane approximation will be used in calculations, particularly in the context of mid-latitude β-channels. The important consequence of using such an approximation when analysing large-scale wave dynamics, is that any poleward deflection of a travelling wave is thus accompanied by a change in f.

2.2.5 Geostrophic balance and quasi-geostrophy

A defining feature of flows subjected to gravity, and in a rotating reference frame is their tendency not to adjust to a state of rest, but rather a state of 'geostrophic balance'. That is, in the context of shallow water flows, the situation in which the Coriolis acceleration is balanced by the horizontal pressure gradient. Mathematically, this is written

$$f\boldsymbol{k} \times \boldsymbol{u} = -g\nabla\eta. \tag{2.80}$$

As it turns out, in the Earth's mid-latitudes, the atmosphere and ocean are in a constant state of near-geostrophic balance (Phillips, 1963), due to the Coriolis acceleration providing a force to balance the pressure gradient in the fluid, and obscuring the tendency for a fluid to flow from areas of high pressure to low pressure. Rather, the geostrophic wind travels along isobars (lines of constant pressure), flowing clockwise around areas of high presure, and anticlockwise around areas of low pressure when $f > 0$ (Northern Hemisphere). Whilst the geostrophic wind is a reasonable first approximation over much of the Earth's surface, the equation (2.80) is only a diagnostic relationship - that is, since it contains no time derivatives, predictions about the evolution of the velocity field cannot be made from it alone.

As a thought experiment, one might consider this balance on an f-plane, so that $f \equiv f_0$ is a constant, and a topography profile with gently sloping bottom. It is immediately apparent that when in geostrophic balance, the fluid velocity is parallel to *isobaths* (lines of constant depth). One could then also imagine a disturbance to this flow where a fluid column of relative vorticity ζ is slightly perturbed from its starting position, so as to increase its vertical extent. By the conservation of potential vorticity equation (2.60), such an increase in depth must be accompanied by an increase in relative vorticity so as to restore geostrophic balance. Indeed, this must ultimately lead to oscillatory behaviour about the geostrophic state, involving a constant exchange between relative vorticity and fluid depth. This is precisely the physics which leads to *topographic* Rossby waves.

Whilst this situation on an f-plane with a sloping topography provides a good intuitive insight into the dynamical processes at work, and in many cases leads to useful physical results in the Ocean setting, it is not the most relevant model to this thesis. However, there is an exact analogy between this case, and the case with a flat-bottomed ocean in the absence of topography viewed on a β-plane, as the non-constancy of the Coriolis parameter allows a similar exchange between ζ and f to take place and drive *planetary* Rossby waves. The following asymptotic treatment, based on this intuition, involves examining a low frequency perturbation about the balanced state, and allows an equation to be derived which governs the wave dynamics of the disturbance due to the constraint imposed by the potential vorticity.

2.2.5.1 The quasi-geostrophic potential vorticity equation

We now derive an important limiting case of the shallow water equations which will be used in chapter 3. Consider the linear equations (2.56) and (2.57) under the β-plane approximation (2.79), so that

$$\begin{aligned} \frac{\partial \boldsymbol{u}}{\partial t} + (f_0 + \beta y)\boldsymbol{k} \times \boldsymbol{u} &= -g\nabla\eta, \\ \frac{\partial \eta}{\partial t} + \nabla \cdot (h\boldsymbol{u}) &= 0. \end{aligned} \tag{2.81}$$

It is useful to write these equations in terms of non-dimensional variables (denoted with an asterisk) using the scalings

$$\boldsymbol{u} = U\boldsymbol{u}^*, \quad \eta = \frac{f_0 L U}{g}\eta^*, \quad \boldsymbol{x} = L\boldsymbol{x}^*, \quad t = \frac{1}{f_0}t^*, \quad h = H_0 h^*, \tag{2.82}$$

where H_0 is a typical depth scale, $L = \sqrt{gH_0}/f_0$ is the Rossby radius - that is, the length-scale over which the Coriolis force becomes as significant as gravity. Denoting by $L_\beta = f_0/\beta$ the length-scale associated with the planetary vorticity gradient, and defining the dimensionless parameter $b = L/L_\beta$, equations (2.81) become

$$\begin{aligned}\frac{\partial \boldsymbol{u}}{\partial t}+(1+by)\boldsymbol{k}\times\boldsymbol{u}&=-\nabla\eta,\\ \frac{\partial \eta}{\partial t}+\nabla\cdot(h\boldsymbol{u})&=0,\end{aligned} \tag{2.83}$$

where the asterisk notation is dropped for convenience. Note that the non-dimensional β effect is considered a small parameter so that $b \ll 1$. In order that geostrophic balance is found at leading order, time is rescaled as $T = bt$, and the fluid depth is rewritten as $h = 1 - bh_b$ so as to include only small $O(b)$ bottom variations, with $h_b(\boldsymbol{x})$ representing the topography deviations from a uniform depth. Thus, the equations become

$$\begin{aligned}b\frac{\partial \boldsymbol{u}}{\partial T}+(1+by)\boldsymbol{k}\times\boldsymbol{u}&=-\nabla\eta,\\ b\frac{\partial \eta}{\partial T}+\nabla\cdot\left[(1-bh_b)\,\boldsymbol{u}\right]&=0.\end{aligned} \tag{2.84}$$

Seeking perturbation expansions of the form

$$\boldsymbol{u}=\boldsymbol{u}^{(0)}+b\boldsymbol{u}^{(1)}+\cdots, \qquad \eta=\eta^{(0)}+b\eta^{(1)}+\cdots, \tag{2.85}$$

and balancing terms in the system (2.84) of like order in b, the leading order terms are found to satisfy the equations of geostrophic balance

$$\boldsymbol{k}\times\boldsymbol{u}^{(0)}=-\nabla\eta^{(0)}, \qquad \nabla\cdot\boldsymbol{u}^{(0)}=0. \tag{2.86}$$

It is notable that in non-dimensional form, $\eta^{(0)}$ acts as a streamfunction for the leading order velocity field $\boldsymbol{u}^{(0)}$, since the velocity components satisfy $\left(u^{(0)}, v^{(0)}\right) = \left(-\partial_y\eta^{(0)}, \partial_x\eta^{(0)}\right)$.

The equations at next order are given by

$$\frac{\partial \boldsymbol{u}^{(0)}}{\partial T} + \boldsymbol{k} \times \boldsymbol{u}^{(1)} + y\boldsymbol{k} \times \boldsymbol{u}^{(0)} = -\nabla \eta^{(1)}, \tag{2.87}$$

$$\frac{\partial \eta^{(0)}}{\partial T} + \nabla \cdot \boldsymbol{u}^{(1)} - \nabla \cdot \left(h_b \boldsymbol{u}^{(0)}\right) = 0. \tag{2.88}$$

From these equations, and the leading order geostrophic balance, a single equation in $\eta^{(0)}$ can be derived. By taking the curl of (2.87), and then substituting (2.88) and (2.86), one retrieves the equation

$$\partial_T \left(\nabla^2 \eta^{(0)} - \eta^{(0)}\right) + \nabla^{\perp} \eta^{(0)} \cdot \nabla h_b + \partial_x \eta^{(0)} = 0, \tag{2.89}$$

where $\nabla^{\perp} = \boldsymbol{k} \times \nabla$ is the *skew-gradient* operator. Equation (2.89) is known as the 'quasi-geostrophic potential vorticity equation', and was first derived in this form by Charney (1948), who performed a systematic scale-analysis of the governing equations for the atmosphere.

2.2.6 Dispersion in a mid-latitude β-channel

To set the scene for later analyses of shallow water systems, in particular the dynamics of shallow water waves over small-scale topography, it is helpful to first develop quantitative results for wave dispersion in a mid-latitude channel. The focus of this section is to introduce the three main large-scale waves found in the mid-latitudes, namely Poincaré, Kelvin, and Rossby waves, and to calculate their dispersion relations using both a numerical procedure, and an asymptotic approximation. Our set-up involves considering waves confined to a mid-latitude channel on a β-plane, centred at $y = 0$ and bounded by sidewalls at $y = \pm w_c$. Indeed, doing so allows for relatively straightforward and accurate calculation of the wave velocities and dispersion relations. Furthermore, highly accurate asymptotic approximations can be derived in the case where the beta parameter is assumed to be small, which acts as a good starting point for deriving accurate analytical results when a small-scale topography is introduced in chapter 3. Our approach to the asymptotic calculations closely follows that of Paldor et al. (2007); Paldor and Sigalov (2008).

Consider the linear equations (2.56) and (2.57), non-dimensionalised according to the scalings (2.82) on a β-plane, and written in component form

$$\frac{\partial u}{\partial t} - (1+by)v = -\frac{\partial \eta}{\partial x}, \tag{2.90}$$

$$\frac{\partial v}{\partial t} + (1+by)u = -\frac{\partial \eta}{\partial y}, \tag{2.91}$$

$$\frac{\partial \eta}{\partial t} + h\frac{\partial u}{\partial x} + h\frac{\partial v}{\partial y} = 0. \tag{2.92}$$

Here, h is assumed to be constant and has thus be taken outside of the horizontal derivatives. The boundary conditions are those of no normal flow on the channel walls, which may be written as $v(\pm w_c/L) = 0$. We deal first with the numerical calculations of the dispersion relations.

2.2.6.1 Numerical calculations of the wave dispersion relations

In order to calculate solutions of (2.90-2.92) in a β-channel, we must turn our attention towards numerical techniques. Since we are most interested in waves which are periodic in the x-direction and periodic in time, solutions to (u, v, η) proportional to $\exp(\mathrm{i}(kx - \omega t))$ are sought, where k is the zonal wavenumber and ω is the frequency. Therefore, making the substitutions

$$(u, v, \eta) \to (u(y), v(y), \eta(y)) \exp(\mathrm{i}(kx - \omega t)), \tag{2.93}$$

reduces the equations (2.90–2.92) to a system of ODEs in y, given by

$$-\mathrm{i}\omega u - (1+by)v = -\mathrm{i}k\eta, \tag{2.94}$$

$$-\mathrm{i}\omega v + (1+by)u = -\frac{\partial \eta}{\partial y}, \tag{2.95}$$

$$-\mathrm{i}\omega\eta + \mathrm{i}khu + h\frac{\partial v}{\partial y} = 0. \tag{2.96}$$

The equations are closed with the boundary conditions $v(\pm 1) = 0$ so that there can be no flow through the channel walls. Note that this corresponds to setting $w_c = L$ initially, so that the channel half-width is equal to the Rossby radius. Whilst it is true that the channel width does affect the solution by determining the quantisation of the meridional component of the wavenumber in the channel, the changes caused by varying w_c are of little interest physically to this thesis and so from hereon the channel width will always be assumed to have walls at $y = \pm 1$ ($\pm L$ in dimensional form).

The system of ODEs (2.94-2.96) defined on $y = [-1, 1]$ is well suited to a Chebyshev spectral method in which the y-grid is discretised into $N + 1$ points ($N = 24$ is used) located at the zeros of the Chebyshev polynomial of order $N + 1$. Standard techniques (see e.g. Trefethen, 2000) allow the differentiation matrix $\boldsymbol{D}_y$ to be obtained for the grid, which allows the discretised version of (2.94-2.96) to be written as a generalised eigenvalue problem of the form

$$-\mathrm{i}\omega \boldsymbol{A}\boldsymbol{v} + \boldsymbol{B}\boldsymbol{v} = 0, \tag{2.97}$$

where $\boldsymbol{v} = (u_1, \cdots, u_{N+1}, v_2, \cdots v_N, \eta_1, \cdots, \eta_{N+1})^T$, and $\boldsymbol{A}$ and $\boldsymbol{B}$ are square block matrices of size $3N + 1$. Note that the discretised v-equation spans only the interior points of the Chebyshev grid, so that the boundary conditions $v(\pm 1) = 0$ are satisfied (on the discrete grid these are enforced by setting $v_1 = v_{N+1} = 0$). Correspondingly, the matrix $\boldsymbol{B}$ is found by first considering the square block matrix of size $3N + 3$ given by

$$\boldsymbol{B} = \left(\begin{array}{c|c|c} 0 & -\boldsymbol{f} & \mathrm{i}k\boldsymbol{\mathcal{I}} \\ \hline \boldsymbol{f} & 0 & \boldsymbol{D}_y \\ \hline \mathrm{i}kh\boldsymbol{\mathcal{I}} & h\boldsymbol{D}_y & 0 \end{array}\right), \tag{2.98}$$

where $\boldsymbol{f} = \mathrm{diag}(1+by_1, \cdots, 1+by_{N+1})$ and $\boldsymbol{\mathcal{I}}$ is the identity matrix, and removing the rows and columns in positions $N + 2$ and $2N + 2$ (we retain the same variable name $\boldsymbol{B}$ for simplicity). The matrix $\boldsymbol{A}$ can be determined by the same process, and for the flat-bottomed channel, this matrix simply reduces to the identity matrix of size $3N + 1$. It is however useful to leave equation (2.97) in its generalised eigenvalue form for ease of generalisation in the later section 3.2.4. The eigenvalues and eigenvectors solving (2.97) are straightforward to find using standard numerical routines.

2.2.6.2 Asymptotic approximations for the wave dispersion relations

Whilst it is not difficult to solve the discrete equation (2.97) to obtain highly accurate numerical approximations for the wave velocities and frequencies in the channel, it is arguably a lot more insightful to develop simple expressions to approximate the solutions. In this section, we analyse equations (2.90-2.92) in the asymptotic regime $b \ll 1$ and find analytical representations of the wave frequencies at leading-order. This asymptotic regime is an appropriate one for the purposes of studying waves in the mid-latitudes, where typical values of the planetary vorticity gradient are $b \approx 0.005$ for the open ocean, and $b \approx 0.05$ for the atmosphere. The analysis closely follows the approach of Paldor et al. (2007) who derive similar asymptotic expressions for the dispersion relations, and Paldor and Sigalov (2008) who extend their analysis to next order in b.

To begin the asymptotic analysis, it is first helpful to derive a single equation for the poleward component of velocity. To do so requires the linearised PV equation (2.61) which for constant h and written in dimensionless form is given by

$$\frac{\partial}{\partial t}\left[\zeta - \frac{(1+by)}{h}\eta\right] + bv = 0, \tag{2.99}$$

where $\zeta = \partial_x v - \partial_y u$ is the relative vorticity of the fluid. Note that this equation can also be derived simply by taking $\partial_x(2.91) - \partial_y(2.90)$ and substituting in (2.92). Now, by taking $-(by/h)\partial_t(2.90) + (1/h)\partial^2_{tt}(2.91) - (1/h)\partial^2_{yt}(2.92) - \partial_x(2.99)$, a single equation for $v(\boldsymbol{x}, t)$ is obtained, given by

$$\frac{\partial}{\partial t}\left[\frac{1}{h}\left(\frac{\partial^2 v}{\partial t^2} + (1+by)^2 v\right) - \nabla^2 v\right] - b\frac{\partial v}{\partial x} = 0. \tag{2.100}$$

Again, choosing the channel sidewalls to be at $y = \pm 1$ and seeking solutions which are periodic in time with frequency ω, and in x with wavenumber k so that

$$v(\boldsymbol{x}, t) \to v(y)\exp\left(\mathrm{i}(kx - \omega t)\right), \tag{2.101}$$

the PDE reduces to the Sturm-Liouville eigenvalue problem

$$\frac{d^2v}{dy^2}+\left(\frac{\omega^2}{h}-k^2-\frac{bk}{\omega}-\frac{(1+by)^2}{h}\right)v=0,\qquad v(\pm1)=0. \tag{2.102}$$

This is a standard problem once the eigenvalues $\{E_n, n=1,2,3\dots\}$ are identified with $E(\omega,k)=\omega^2/h-k^2-bk/\omega$. In general, the $\{E_n\}$, which depend only on the parameter b, must be calculated numerically as in the previous section, with the dispersion relations then found from the roots of the cubic

$$\frac{\omega^2}{h}-k^2-\frac{bk}{\omega}=E_n(b),\qquad n=1,2,3\dots. \tag{2.103}$$

The roots of (2.103) for each eigenvalue E_n form three solution branches. The two roots with greatest magnitude (but which differ in sign) correspond to Poincaré waves, whilst the final, much smaller root corresponds to a Rossby wave.

Of course, there also exists a trivial solution to (2.102) given by $v=0$ everywhere. This solution corresponds to another wave present in the channel, namely the Kelvin wave. To find the dispersion relation for this wave, we set $v=0$ in equations (2.90) and (2.92), giving

$$\frac{\partial u}{\partial t}=-\frac{\partial\eta}{\partial x},\qquad \frac{\partial\eta}{\partial t}+h\frac{\partial u}{\partial x}=0. \tag{2.104}$$

Once again seeking periodic solutions for u and η which are proportional to $\exp\left(\mathrm{i}(kx-\omega t)\right)$, it is deduced that the dispersion relation for this particular wave is given analytically by

$$\omega=\sqrt{h}k. \tag{2.105}$$

When it is assumed that $v(y)$ is not uniformly zero across the channel, then equation (2.102) must be solved in order to determine the eigenvalues E_n and hence the dispersion relations for Poincaré and Rossby waves. Unfortunately, this is not a straight forward process since for $b\neq0$, no analytical solutions to the problem exist which satisfy the channel boundary conditions. However, as previously pointed out, the parameter b which quantifies the magnitude of the planetary vorticity gradient is typically small in most oceanic and atmospheric settings, and thus allows for a relatively simple asymptotic treatment of the problem.

Under the assumption that $b \ll 1$, the leading-order approximate solutions to (2.102) corresponding to Poincaré waves are found when the wave frequencies ω_P are of order unity. In this case, the eigenvalues at leading order are

$$E_{n,P} \equiv \frac{\omega_P^2}{h} - k^2, \tag{2.106}$$

and the problem reduces to solving the ODE

$$\frac{d^2v}{dy^2} + \left(E_{n,P} - \frac{1}{h}\right) v = 0, \qquad v(\pm 1) = 0, \tag{2.107}$$

which has a simple wave solution given by

$$v_{n,P}(y) = A_P \exp\left(\mathrm{i}y\sqrt{E_{n,P} - 1/h}\right) + B_P \exp\left(-\mathrm{i}y\sqrt{E_{n,P} - 1/h}\right), \tag{2.108}$$

where A_P and B_P are constants. Applying the boundary conditions at $y = \pm 1$ leads to the constraint $E_{n,P} - 1/h = \pi^2 n^2/4$, and hence the dispersion relations for Poincaré waves at leading order are given by

$$\omega_P = \pm\sqrt{1 + h(k^2 + \pi^2 n^2/4)} + O(b), \qquad n = 1, 2, 3 \ldots. \tag{2.109}$$

Rossby wave solutions occur when the wave frequencies ω_R are assumed to be $O(b)$, in which case the leading order terms in the the eigenvalues are given by

$$E_{n,R} \equiv -k^2 - \frac{bk}{\omega_R}. \tag{2.110}$$

An identical analysis to the Poincaré wave case leads to the constraint $E_{n,R} - 1/h = \pi^2 n^2/4$, and thus the dispersion relations for Rossby waves are given by

$$\omega_R = -\frac{bkh}{1 + h(k^2 + \pi^2 n^2/4)} + O(b^2). \tag{2.111}$$

It is notable that (2.111) can also be derived from the quasi-geostrophic potential vorticity equation (2.89) when h_b is a constant, and after rescaling time. This is unsurprising, since in deriving (2.89) the same $b \ll 1$ assumption was made, along with the assumption that ω was of the same order (since we rescaled time with $T = bt$). These scalings naturally filter out both Poincaré and Kelvin waves, and hence only the low-frequency Rossby waves remain.

Figure 2.2 compares the dispersion relations calculated from (2.97) to the analytical expressions (2.105), (2.109) and (2.111) for a flat-bottomed ocean of depth $h = 1$, and a relatively large beta parameter $b = 0.5$. Perhaps surprisingly, the asymptotic approximations agree well with the numerical results even for such a large value of b. This fact is particularly pertinent to the next chapter of this thesis when the bathymetry is allowed to vary, since it is well known (Pedlosky, 1987, §3.10) that large-scale gradients in the ocean depth result in gradients in the potential vorticity which also support Rossby waves, and hence larger values of b may be more representative of typical ocean conditions. Note that the numerical and asymptotic results corresponding to the Kelvin wave are exactly in agreement, since when $v = 0$ uniformly across the channel the dispersion relation is found from the governing equations analytically.

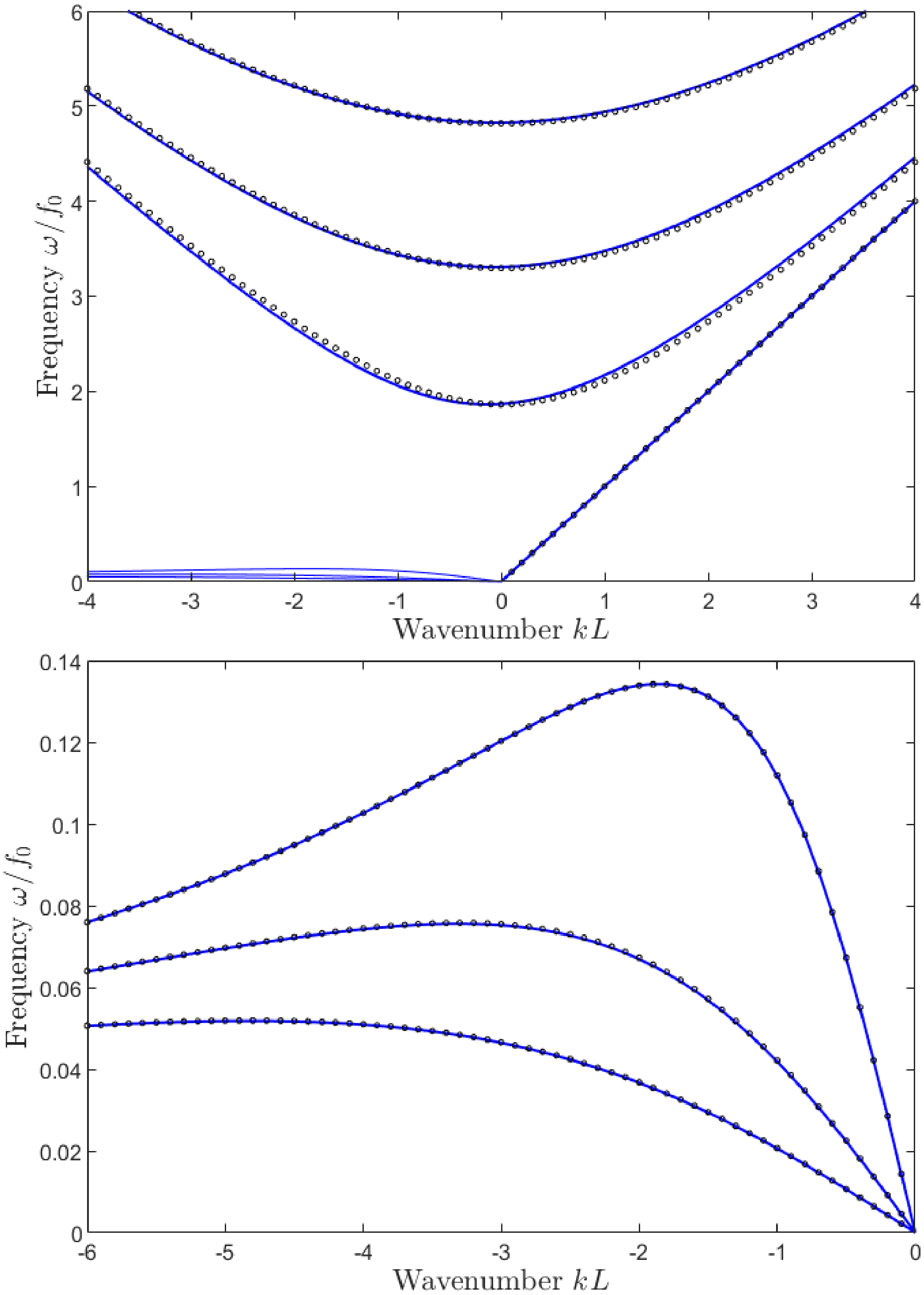

Figure 2.2: Dispersion relations for the Kelvin wave, and the first three modes ($n = 1, 2, 3$) of Poincaré and Rossby waves over a flat bottom of depth $h = 1$, beta parameter $b = 0.5$, and non-dimensional channel width $w_c/L = 1$. Shown are the numerical solutions to (2.97) (blue lines), as well as the asymptotic approximations (2.105), (2.109) and (2.111) (black circles). The top panel shows the dispersion relations for all three wave types, and the lower panel shows only the Rossby waves for clarity.

Chapter 3

The rotating shallow water equations in the presence of varying topography

The work in this chapter has appeared in Goldsmith and Esler (2021).

In the previous chapter, the dispersive characteristics of the waves in a flat-bottomed shallow water β-channel were investigated using both asymptotic and numerical techniques. Here, the question of how these dispersion relations are modified in the presence of finite topography, with horizontal scale much smaller than the wavelength of the waves in question, is addressed in detail using the method of homogenisation. The aim is to provide some quantitative insight into the extent to which variable ocean bathymetry can cause wave propagation speeds to differ from predictions based on the average ocean depth, with a view to providing guidance to ocean model developers as to the general importance of accurate parameterisation of bottom roughness, at least as far as accurately representing the propagation of large-scale waves is concerned.

We aim to connect with and extend two important bodies of work. The first concerns the non-rotating problem, in which the linear rSWE reduce to the classical wave equation. Topography enters the problem as a variable local wave speed $c = \sqrt{gh}$ (g gravity, h ocean depth), and to determine the effective speed c_{eff} of long waves in the presence of variations in c is a classical problem in the mathematics of homogenisation, in its essence equivalent to that first formulated by Rayleigh (1892) for the heat equation. The technicalities of this were covered in section 2.1 of this thesis. Modern analysis of homogenisation problems (see e.g. the reviews of Nandakumaran, 2007; Allaire, 2012; Mei and Vernescu, 2010, §5.5) reveals that, using $\langle\cdot\rangle$ to denote a horizontal average, $\langle c^{-2}\rangle^{-1} \leq c_{\text{eff}}^2 \leq \langle c^2\rangle$, i.e. for any small-scale bathymetry the square of the effective long wave speed c_{eff} is bounded below by the harmonic mean of c^2 (in the elasticity literature the Reuss bound) and above by its arithmetic mean (the Voigt bound) (see also §2.1.1.2 for a discussion). Equivalently, the effective ocean depth H_{eff} 'felt' by the long waves satisfies $\langle h^{-1}\rangle^{-1} \leq H_{\text{eff}} \leq \langle h\rangle$. Notably, the lower (harmonic mean or Reuss) bound is actually attained for propagation over one-dimensional topography (e.g. Rosales and Papanicolaou, 1983; Hu and Chan, 2005; Van Der Baan, 2001), (see also Holmes, 2012, for an introductory treatment) meaning that the simple approximation of using the averaged depth $\langle h\rangle$ in place of H_{eff} will certainly result in large modelling errors for waves propagating over steep ocean ridges. For two-dimensional topography H_{eff} lies somewhere between the two bounds, and one aim here is to quantify its exact dependence on topographic height and area fraction for some idealised two-dimensional topographies, in particular arrays of periodic cylinders for which highly accurate asymptotic solutions exist (e.g. Balagurov and Kashin, 2001; Godin, 2013). Another key question is how the classical wave equation analysis is modified by the introduction of rotation, i.e. are Poincaré and Kelvin waves affected to the same extent as non-rotating gravity waves?

The second key body of work concerns the quasi-geostrophic limit of the rSWE. Here solutions of the homogenisation problem formulated by Rhines and Bretherton (1973), applied to both sparse random topographies and (possibly densely packed) periodic arrays (Vanneste, 2000a,b; Benilov, 2000), give insight into the extent to which Rossby wave propagation is affected by small-scale topography. Compared with the gravity wave case, the physics is relatively complicated, as the long Rossby waves of interest can interact resonantly with trapped topographic Rossby waves attached to each seamount (see e.g. Jansons and Johnson, 1988). In the absence of regularising dissipative processes, such as Ekman friction, the modified Rossby wave dispersion relations feature singularities at the resonant frequencies. These quasi-geostrophic results are naturally restricted to topography satisfying the requirements of quasi-geostrophic scaling, i.e. ocean depth variations must satisfy $|h - \langle h \rangle|/\langle h \rangle \ll 1$, and the horizontal scale of the topography must be sufficiently large that the Rossby number of the motion remains small (see discussion below). The present treatment, in the full rSWE, relaxes these assumptions and extends the previous results to finite topographies including islands. Not only is an assessment of the wider validity of the quasi-geostrophic results made possible, but also a quantitative comparison between the relative effect of the topography on the different wave types (Rossby, Kelvin and Poincaré) can be made.

It is important to emphasise that the focus here is on waves which are long relative to the topographic length scale. Other asymptotic regimes of interest involve flow over topography with a shallow gradient or infinitesimal amplitude. In these cases, the homogenisation technique and related multiple-scale methods can be adapted to study the behaviour of waves with wavelengths comparable to the topography, a situation which allows for phenomena such as Bragg resonance between surface gravity waves and periodic topography (e.g. Mei, 1985; Naciri and Mei, 1988). Similarly, Bühler and Holmes-Cerfon (2011) and Li and Mei (2014) have considered the effect of bathymetry on internal tides in a stratified ocean, and have quantified the damping effect of a random topographic distribution at leading order in amplitude. As a consequence, the results presented here do not constitute a complete picture, and shorter waves can be expected to exhibit a distinct and rich phenomenology.

This chapter is organised as follows. In section 3.1 the method of homogenisation is introduced and applied to the linearised rSWE to obtain the homogenised governing equations. The coefficients in these governing equations are determined from the solutions of cell problems defined on the short length scale, which are formulated explicitly for the rSWE. The quasi-geostrophic and non-rotating limits of the governing equations and cell problems are then considered, making the connection to previous results clear. In section 3.2 the case of periodic arrays of seamounts arranged in a regular square lattice is treated in detail. Particular attention is given to cylindrical seamounts, because the multipole expansion method of e.g. Balagurov and Kashin (2001) and Godin (2013) can be used in this case to obtain highly accurate asymptotic solutions to the cell problems, including the new 'rotating' cell problem which arises from the rSWE. The outcome is various means to determine the topographically induced corrections to the dispersion relations of Kelvin, Poincaré and Rossby waves, including an explicit formula valid for Rossby waves in the presence of finite amplitude topography, complementing the quasi-geostrophic results of Benilov (2000) and Vanneste (2000b). In section 3.3 the case of well-separated randomly distributed seamounts is considered, with seamount height, radius and density determined by a prescribed distribution. Again, the goal is to determine the corrections to the wave dispersion relations. In section 3.4 conclusions are drawn.

3.1 The non-dimensional equations and multiple scales approach

Recall the linearised rSWE on a β-plane in an ocean of undisturbed depth h, and which are non-dimensionalised according to the scalings (2.82)

$$\begin{aligned} \boldsymbol{u}_t + (1+by)\boldsymbol{k}\times\boldsymbol{u} &= -\nabla\eta, \\ \eta_t + \nabla\cdot(h\boldsymbol{u}) &= 0. \end{aligned} \tag{3.1}$$

The depth h is assumed to vary on a horizontal scale l due to the presence of topography, and in all that follows it is assumed that $l \ll L, L_\beta$. (Recall also $L = \sqrt{gH_0}/f_0$ is the Rossby radius, $L_\beta = f_0/\beta$ is the length scale associated with the planetary vorticity gradient and $b = L/L_\beta$ is a non-dimensional parameter which is treated as order unity).

Below, we will also make use of the linear potential vorticity equation (2.61), which for a varying topography on a β-plane, and non-dimensionalised as above, is given by

$$\frac{1}{h}\frac{\partial}{\partial t}\left(\zeta - \frac{(1+by)\eta}{h}\right) + \boldsymbol{u}\cdot\nabla\left(\frac{1+by}{h}\right) = 0, \tag{3.2}$$

where $\zeta = \boldsymbol{k}\cdot\nabla\times\boldsymbol{u}$ is the relative vorticity.

To exploit the horizontal scale separation between the topography and the length scales of the waves of interest, a small parameter $\varepsilon = l/L \ll 1$ can now be introduced. To permit multiple-scale analysis, the spatial variable $\boldsymbol{X} = \boldsymbol{x}/\varepsilon$ can be defined, which describes spatial variations on the scale of the topography, which we treat as independent of $\boldsymbol{x}$ as permitted by the concept of two-scale convergence. In general, the topography $h(\boldsymbol{X},\boldsymbol{x})$ can also be allowed to vary on the long length scale associated with $\boldsymbol{x}$, as would be useful for example to describe a large-scale topographic slope covered in small-scale seamounts.

Next, we introduce an average $\langle\cdot\rangle$ over the short scales, which can be applied to any function $g(\boldsymbol{X},\boldsymbol{x})$,

$$\langle g\rangle = \frac{1}{|\Omega|}\int_\Omega g(\boldsymbol{X},\boldsymbol{x})\ \mathrm{d}\boldsymbol{X}. \tag{3.3}$$

In the following sections, two main cases will be considered. The first, most tractable case, is that of a regular periodic lattice of seamounts, in which case Ω is a single doubly periodic cell ($|\Omega|$ denotes its area). The second case is that of randomly distributed topography, in which case Ω can be taken to be a spatial average over a 'mesoscale' region which is (asymptotically) intermediate in size between the small and large scales. In the asymptotic limit, the number of mountains in the mesoscale region will tend to infinity, and the mesoscale average will be independent of the particular distribution of the topography and will therefore be equivalent to an ensemble average. The analysis which follows in the rest of this section applies equally in both regimes. Averaged variables will be denoted below by capitals, e.g. applying the spatial average to the topography gives

$$H(\boldsymbol{x}) = \langle h(\boldsymbol{X},\boldsymbol{x})\rangle. \tag{3.4}$$

Finally, replacing horizontal derivatives according to the multi-scale formalism, using the chain rule (i.e. $\nabla \to \varepsilon^{-1}\nabla_{\boldsymbol{X}} + \nabla_{\boldsymbol{x}}$) gives

$$\begin{aligned} \varepsilon \boldsymbol{u}_t + \varepsilon(1+by)\boldsymbol{k}\times\boldsymbol{u} &= -\nabla_{\boldsymbol{X}}\eta - \varepsilon\nabla_{\boldsymbol{x}}\eta, \\ \varepsilon\eta_t + \nabla_{\boldsymbol{X}}\cdot(h\boldsymbol{u}) + \varepsilon\nabla_{\boldsymbol{x}}\cdot(h\boldsymbol{u}) &= 0. \end{aligned} \tag{3.5}$$

The equations (3.5) are the starting point for the analysis to follow.

3.1.1 The homogenised equations

The large-scale homogenised equations can be obtained from (3.5) by seeking a multiple-scale perturbation solution of the form

$$\begin{aligned} \eta(\boldsymbol{X},\boldsymbol{x},t;\varepsilon) &= \eta_0(\boldsymbol{X},\boldsymbol{x},t) + \varepsilon\eta_1(\boldsymbol{X},\boldsymbol{x},t) + ... \\ \boldsymbol{u}(\boldsymbol{X},\boldsymbol{x},t;\varepsilon) &= \boldsymbol{u}_0(\boldsymbol{X},\boldsymbol{x},t) + \varepsilon\boldsymbol{u}_1(\boldsymbol{X},\boldsymbol{x},t) + ... \end{aligned} \tag{3.6}$$

Inserting (3.6) in (3.5) gives, at leading order

$$\nabla_{\boldsymbol{X}}\eta_0 = 0, \qquad \nabla_{\boldsymbol{X}}\cdot(h\boldsymbol{u}_0) = 0. \tag{3.7}$$

From this we deduce that $\eta_0 = \Pi(\boldsymbol{x},t)$ is independent of the small-scale variable $\boldsymbol{X}$ (i.e. $\eta_0 = \langle\eta_0\rangle := \Pi$), and that

$$\boldsymbol{u}_0(\boldsymbol{X},\boldsymbol{x},t) = \frac{\boldsymbol{U}H + \nabla_{\boldsymbol{X}}^{\perp}\psi}{h}, \tag{3.8}$$

where $\nabla_{\boldsymbol{X}}^{\perp} \equiv \boldsymbol{k}\times\nabla_{\boldsymbol{X}}$ is the skew-gradient operator, and

$$\boldsymbol{U}(\boldsymbol{x},t) = \frac{\langle\boldsymbol{u}_0 h\rangle}{\langle h\rangle}$$

is the depth-weighted average velocity. Here $\psi(\boldsymbol{X},\boldsymbol{x},t)$ is an unknown scalar function to be determined.

Next, applying the averaging operator to the multi-scale equations (3.5), after multiplying the momentum equation by h, gives, at leading order

$$\begin{aligned} \boldsymbol{U}_t + (1+by)\boldsymbol{k}\times\boldsymbol{U} &= -\nabla_{\boldsymbol{x}}\Pi + \frac{\langle \eta_1 \nabla_{\boldsymbol{X}} h\rangle}{H}, \\ \Pi_t + \nabla_{\boldsymbol{x}}\cdot(H\boldsymbol{U}) &= 0. \end{aligned} \tag{3.9}$$

Equations (3.9) govern the evolution of long waves in the presence of topography, except that to close the equations it remains necessary to evaluate the correlation term $\langle \eta_1 \nabla_{\boldsymbol{X}} h\rangle$ in terms of the averaged variables $\boldsymbol{U}$, Π and H.

To evaluate the correlation term η_1 must be determined, and to do so it is necessary to consider the momentum equation of (3.5) at next order. Multiplying by h and taking the divergence $\nabla_{\boldsymbol{X}}\cdot(\cdot)$, gives

$$\nabla_{\boldsymbol{X}}\cdot(h\nabla_{\boldsymbol{X}}\eta_1) - (1+by)\nabla^2_{\boldsymbol{X}}\psi = -\nabla_{\boldsymbol{X}} h\cdot\nabla_{\boldsymbol{x}}\Pi. \tag{3.10}$$

This is an elliptic equation for η_1 which involves the other unknown function ψ. Evidently another equation is needed to close the system, which can be determined most easily from the PV equation (3.2), which at leading order in ε is

$$\begin{aligned} \nabla_{\boldsymbol{X}}\cdot\left(\frac{\nabla_{\boldsymbol{X}}\psi_t}{h}\right) - (1+by)\nabla_{\boldsymbol{X}}\psi\cdot\nabla^{\perp}_{\boldsymbol{X}}\left(\frac{1}{h}\right) = \\ - H\left((1+by)\boldsymbol{U} - \boldsymbol{k}\times\boldsymbol{U}_t\right)\cdot\nabla_{\boldsymbol{X}}\left(\frac{1}{h}\right). \end{aligned} \tag{3.11}$$

Notice that (3.10) and (3.11) have both been written with terms involving the unknown ψ and η_1 on the left, and 'source' terms involving h and the averaged variables on the right. Before η_1 can be found in terms of the sources from (3.10), (3.11) must first be solved for ψ. The time dependence in (3.11) is an expected feature, and arises because the rotation adds new physics to the shallow water equations, namely that topography at any horizontal scale will support the motion of trapped topographic Rossby waves (Jansons and Johnson, 1988; Longuet-Higgins, 1967). As discussed in the quasi-geostrophic context by Vanneste (2000b) and Benilov (2000), these trapped Rossby waves can be excited resonantly by the large-scale motion.

In general, because (3.10-3.11) are linear in ψ and η_1, the solution for η_1 can be expressed formally using a Green's function approach, in the form of history integral over the past state of the system. This approach, broadly following that of (Vanneste, 2000a), is followed in Appendix C, and results in an integro-differential equation (C.6) for the time-evolution of the momentum $\boldsymbol{U}$.

However, our primary interest here is in the impact of the topography on the dispersion relations of periodic waves, therefore solutions $\propto \exp(-\mathrm{i}\omega t)$ will henceforth be sought, allowing the substitution $\partial_t \to -\mathrm{i}\omega$. It follows that (3.11) becomes

$$\begin{aligned}\nabla_{\boldsymbol{X}} \cdot \left(\frac{\nabla_{\boldsymbol{X}}\psi}{h}\right) - \mathrm{i}\frac{1+by}{\omega}\nabla_{\boldsymbol{X}}\psi \cdot \nabla_{\boldsymbol{X}}^{\perp}\left(\frac{1}{h}\right) = \qquad\qquad\qquad\qquad \\ - H\left(\mathrm{i}\frac{1+by}{\omega}\boldsymbol{U} - \boldsymbol{k}\times\boldsymbol{U}\right)\cdot\nabla_{\boldsymbol{X}}\left(\frac{1}{h}\right),\end{aligned} \tag{3.12}$$

and the solutions η_1 and ψ of (3.10) and (3.12) can be expressed as

$$\begin{aligned}\eta_1 &= \boldsymbol{\Phi}\cdot\nabla_{\boldsymbol{x}}\Pi + H(1+by)\boldsymbol{\Psi}_{(1+by)/\omega}\cdot\left(\mathrm{i}\frac{1+by}{\omega}\boldsymbol{U} - \boldsymbol{k}\times\boldsymbol{U}\right), \\ \psi &= H\boldsymbol{G}\cdot\left(\mathrm{i}\frac{1+by}{\omega}\boldsymbol{U} - \boldsymbol{k}\times\boldsymbol{U}\right).\end{aligned} \tag{3.13}$$

In (3.13) the vectors $\boldsymbol{\Phi} = (\Phi_1, \Phi_2)^T$, $\boldsymbol{G} = (G_1, G_2)^T$ and $\boldsymbol{\Psi}_\alpha = (\Psi_{1,\alpha}, \Psi_{2,\alpha})^T$ are obtained by solving the cell problems

$$\nabla_{\boldsymbol{X}} \cdot (h\nabla_{\boldsymbol{X}}\Phi_i) = -\partial_{X_i}h, \tag{3.14}$$

and

$$\begin{aligned}\nabla_{\boldsymbol{X}} \cdot (h\nabla_{\boldsymbol{X}}\Psi_{i,\alpha}) &= \nabla_{\boldsymbol{X}}^2 G_i, \\ \nabla_{\boldsymbol{X}} \cdot \left(\frac{\nabla_{\boldsymbol{X}}G_i}{h}\right) - \mathrm{i}\alpha\nabla_{\boldsymbol{X}}G_i \cdot \nabla_{\boldsymbol{X}}^{\perp}\left(\frac{1}{h}\right) &= -\partial_{X_i}\left(\frac{1}{h}\right),\end{aligned} \tag{3.15}$$

respectively, where $\alpha > 0$ is a parameter. Since only η_1 appears in the averaged equations (3.9), the components G_i do not feature explicitly and act more as intermediate variables in the cell problem (3.15). Their dependence on α is therefore suppressed for convenience. The cell problems are elliptic equations defined on Ω, and have unique solutions up to arbitrary functions of the large-scale variables only (see e.g. §5.3.2 of Holmes, 2012). The arbitrary functions can be ignored since they do not contribute to the correlation term in (3.9).

It is important to emphasise that the solutions $\boldsymbol{\Phi}$ and $\boldsymbol{\Psi}_\alpha$ of the cell problems depend only on the details of the topography, not on the waves being studied or on dynamical parameters such as b. The first cell problem (3.14) is, for reasons to be explained below, identical to equation (2.13), most commonly arising in classical two-dimensional homogenisation problems of mathematical physics, such as heat transfer through heterogeneous media, the study of which dates back to Rayleigh (1892). The second cell problem (3.15), which is perhaps more accurately described as a one-parameter family of cell problems parametrised by α, is introduced by the presence of rotation and the associated topographic Rossby waves. An important point is that for real α, $\boldsymbol{\Psi}_\alpha = \boldsymbol{\Psi}^*_{-\alpha}$, as can be seen by making the substitutions $\alpha \to -\alpha$ and $G_i \to G_i^*$ (complex conjugate).

Inserting our expression for η_1 from (3.13) leads to

$$- \mathrm{i}\omega \left(\boldsymbol{\mathcal{I}} + \left(\frac{1+by}{\omega} \right)^2 \boldsymbol{\mathcal{K}}_{(1+by)/\omega} \right) \cdot \boldsymbol{U} + (1+by) \left(\boldsymbol{\mathcal{I}} + \boldsymbol{\mathcal{K}}_{(1+by)/\omega} \right) \cdot \boldsymbol{k} \times \boldsymbol{U} = - \left(\boldsymbol{\mathcal{I}} + \boldsymbol{\mathcal{D}} \right) \cdot \nabla_{\boldsymbol{x}} \Pi, \quad (3.16)$$

where $\boldsymbol{\mathcal{I}}$ is the identity matrix and the matrices $\boldsymbol{\mathcal{D}}$ and $\boldsymbol{\mathcal{K}}_\alpha$ are given by

$$\boldsymbol{\mathcal{D}} = -\frac{1}{H} \begin{pmatrix} \langle \Phi_1 \partial_{X_1} h \rangle & \langle \Phi_2 \partial_{X_1} h \rangle \\ \langle \Phi_1 \partial_{X_2} h \rangle & \langle \Phi_2 \partial_{X_2} h \rangle \end{pmatrix}, \quad \boldsymbol{\mathcal{K}}_\alpha = \begin{pmatrix} \langle \Psi_{1,\alpha} \partial_{X_1} h \rangle & \langle \Psi_{2,\alpha} \partial_{X_1} h \rangle \\ \langle \Psi_{1,\alpha} \partial_{X_2} h \rangle & \langle \Psi_{2,\alpha} \partial_{X_2} h \rangle \end{pmatrix}. \quad (3.17)$$

For cell problems with a fourfold rotational symmetry, for example axisymmetric seamounts arranged in a regular square lattice, these matrices simplify to $\boldsymbol{\mathcal{D}} = D\boldsymbol{\mathcal{I}}$ and

$$\boldsymbol{\mathcal{K}}_\alpha = \begin{pmatrix} K_1(\alpha) & -\mathrm{i}K_2(\alpha) \\ \mathrm{i}K_2(\alpha) & K_1(\alpha) \end{pmatrix},$$

for real, scalar functions $K_1(\alpha)$ and $K_2(\alpha)$, which hereafter we will call the 'topographic resonance functions'. The cell-averaged linear rSWE then simplify to

$$\begin{aligned}
&-\mathrm{i}\omega\left(1+\left(\tfrac{1+by}{\omega}\right)^2 K_1\left(\tfrac{1+by}{\omega}\right)+\left(\tfrac{1+by}{\omega}\right)K_2\left(\tfrac{1+by}{\omega}\right)\right)\boldsymbol{U}\\
&+(1+by)\left(1+K_1\left(\tfrac{1+by}{\omega}\right)+\left(\tfrac{1+by}{\omega}\right)K_2\left(\tfrac{1+by}{\omega}\right)\right)\boldsymbol{k}\times\boldsymbol{U}=-(1+D)\nabla_{\boldsymbol{x}}\Pi,\\
&\qquad\qquad\qquad\qquad\qquad\qquad -\mathrm{i}\omega\Pi+\nabla_{\boldsymbol{x}}\cdot(H\boldsymbol{U})=0,
\end{aligned}\tag{3.18}$$

where again, we emphasise that D, $K_1(\alpha)$ and $K_2(\alpha)$ are properties of the topography alone.

The system of equations (3.18) can be solved to obtain expressions determining the dispersion relations of the Poincaré, Kelvin and Rossby waves solutions of the rSWE on the β-plane. In sections 3.2 and 3.3 below, numerical and analytical results are presented which illustrate the extent to which different topographies affect the dispersion relations of these waves. The results of this section have counterparts when Ekman friction is included in the governing equations (see Appendix B), but for simplicity our main focus here is on the frictionless case. However, as in the quasi-geostrophic problem (Vanneste, 2000a,b), it is necessary to include a regularising process such as Ekman friction in order to make physical sense of behaviours when there is a resonance between the waves of interest and topographic Rossby waves on the seamounts. Other dissipative processes, such as eddy diffusivity of momentum, could also play a regularising role. Additionally, nonlinearity will also likely act to remove the singularity at the resonances as occurs in the theory of Bragg scattering of water waves (see e.g. the weakly nonlinear analysis of Hara and Mei, 1987). Here, following Vanneste (2000b), only Ekman friction is considered and in Appendix B the results above are generalised to include this effect. The analogue of the equations (3.18) are shown there to be (B.12).

Next, we consider some relevant limits of equations (3.9) and (3.18).

3.1.2 Quasi-geostrophic limit of the homogenised equations

The quasi-geostrophic limit of the homogenised equations (3.9) can be obtained by considering the joint limit $b \ll 1$, in which $h = 1 - bh_b$, i.e. deviations from a uniform depth of unity are small, and are described by the rescaled bottom topography $h_b(\boldsymbol{X})$ (as for the full system, h_b can be allowed to depend on $\boldsymbol{x}$ if required). Time must also be rescaled to the slower timescale $T = bt$. Expanding

$$\Pi = \Pi^{(0)} + b\Pi^{(1)} + b^2\Pi^{(2)} + ..., \quad \boldsymbol{U} = \boldsymbol{U}^{(0)} + b\boldsymbol{U}^{(1)} + b^2\boldsymbol{U}^{(2)} + ..., \tag{3.19}$$

leads to geostrophic balance at leading order $-\nabla_{\boldsymbol{x}}\Pi^{(0)} = \boldsymbol{k} \times \boldsymbol{U}^{(0)}$ (equivalently $\boldsymbol{U}^{(0)} = \nabla_{\boldsymbol{x}}^{\perp}\Pi^{(0)}$), and at next order

$$\begin{aligned} \partial_T \boldsymbol{U}^{(0)} + \boldsymbol{k} \times \boldsymbol{U}^{(1)} + y\boldsymbol{k} \times \boldsymbol{U}^{(0)} &= -\nabla_{\boldsymbol{x}}\Pi^{(1)} - \langle \eta_1^{(0)} \nabla_{\boldsymbol{X}} h_b \rangle, \\ \partial_T \Pi^{(0)} + \nabla_{\boldsymbol{x}} \cdot \boldsymbol{U}^{(1)} &= 0. \end{aligned} \tag{3.20}$$

Applying $\nabla_{\boldsymbol{x}}^{\perp}\cdot$ to the momentum equation in (3.20), and using the free surface displacement equation to eliminate $\nabla_{\boldsymbol{x}} \cdot \boldsymbol{U}^{(1)}$, leads to the quasi-geostrophic potential vorticity equation

$$\partial_T \left(\nabla_{\boldsymbol{x}}^2 \Pi^{(0)} - \Pi^{(0)} \right) + \Pi_x^{(0)} + \nabla_{\boldsymbol{x}} \cdot \langle h_b \nabla_{\boldsymbol{X}}^{\perp} \eta_1^{(0)} \rangle = 0. \tag{3.21}$$

Here, $\eta_1^{(0)}$ is determined by the leading-order terms in (3.10) and (3.11) which can be simplified to

$$\partial_T \nabla_{\boldsymbol{X}}^2 \eta_1^{(0)} - \nabla_{\boldsymbol{X}} \eta_1^{(0)} \cdot \nabla_{\boldsymbol{X}}^{\perp} h_b = \nabla_{\boldsymbol{x}} \Pi^{(0)} \cdot \nabla_{\boldsymbol{X}}^{\perp} h_b. \tag{3.22}$$

Equations (3.21) and (3.22) are the homogenised equations of the quasi-geostrophic system of Vanneste (2000a,b) in the absence of friction, and a generalised version of equation (2.89) to include small-scale topography. If we seek solutions $\propto \exp(-\mathrm{i}\Omega T)$, where $\Omega = \omega/b$ is the frequency on the slow time scale, then the solution $\eta_1^{(0)}$ is found from the leading-order terms in (3.13) to be

$$\eta_1^{(0)} = \frac{\mathrm{i}}{\Omega} \tilde{\boldsymbol{\Psi}}_{1/\Omega} \cdot \nabla_{\boldsymbol{x}}^{\perp} \Pi. \tag{3.23}$$

where the vector $\tilde{\boldsymbol{\Psi}}_{\alpha} = \mathrm{Re}\ (\tilde{\Psi}_{1,\alpha}, \tilde{\Psi}_{2,\alpha})^T$ has components which solve the cell problem (3.15) at leading-order in b,

$$\nabla^2_{\boldsymbol{X}} \tilde{\Psi}_{i,\alpha} - \mathrm{i}\alpha \nabla_{\boldsymbol{X}} \tilde{\Psi}_{i,\alpha} \cdot \nabla^{\perp}_{\boldsymbol{X}} h_b = -\partial_{X_i} h_b. \tag{3.24}$$

Focussing on symmetric topography, defining $\tilde{K}(\alpha) = -\langle \tilde{\Psi}_{1,\alpha} \partial_{X_1} h_b \rangle$ to be the quasi-geostrophic analogue of $K_1(\alpha)$ (the quasi-geostrophic analogue of $K_2(\alpha)$ vanishes), and then substituting $\Omega = \omega/b$ allows the eigenvalue equation for the homogenised quasi-geostrophic system to be written as

$$-\mathrm{i}\omega \left(1 + \tfrac{b^2}{\omega^2} \tilde{K}\left(\tfrac{b}{\omega}\right)\right) \nabla^2_{\boldsymbol{x}} \Pi^{(0)} + \mathrm{i}\omega \Pi^{(0)} + b \Pi^{(0)}_x = 0, \tag{3.25}$$

recovering the result of Vanneste (2000a).

The derivation of (3.21-3.25) above differs from that of Vanneste (2000a) in a significant way. Here, we have obtained (3.21-3.25) by first deriving the homogenised equations (3.9) and then taking the quasi-geostrophic limit, corresponding to the following ordering of the small parameters: $\varepsilon \ll b \ll 1$. Vanneste, by contrast, applied the homogenisation procedure to the quasi-geostrophic equations themselves, consistent with the ordering $b \ll \varepsilon \ll 1$. The fact that the same equations are found in each case gives a clear indication that the result is independent of the value of the ratio $\varepsilon/b = lL_\beta/L^2$ (where l is the topography length scale, L is the Rossby radius and $L_\beta = f_0/\beta$). In fact, independence of ε/b can be shown more explicitly by a direct asymptotic treatment of (3.5) with $\varepsilon \sim b$ (details given in Appendix A). In other words, there is no restriction on the topographic length scale l, beyond the shallow water scaling $l \gg H_0$, for (3.21-3.22) to hold, a result which extends that of Vanneste, which covers only the case $l \gg L^2/L_\beta$.

3.1.3 Non-rotating homogenised equations

To introduce our main results below, it is helpful to first consider (3.9) in the absence of rotation

$$\begin{aligned} \boldsymbol{U}_t &= -\nabla_{\boldsymbol{x}}\Pi + \frac{\langle \eta_1 \nabla_{\boldsymbol{X}} h\rangle}{H}, \\ \Pi_t + \nabla_{\boldsymbol{x}} \cdot (H\boldsymbol{U}) &= 0. \end{aligned} \tag{3.26}$$

where in this case $\eta_1 = \boldsymbol{\Phi} \cdot \nabla_{\boldsymbol{x}}\Pi$, with $\boldsymbol{\Phi} = (\Phi_1, \Phi_2)^T$, and Φ_i is determined by the cell problem (3.14). In this case, taking the time derivative of the free surface equation and substituting for $\boldsymbol{U}_t$ results in the wave equation

$$\Pi_{tt} = \nabla_{\boldsymbol{x}} \cdot \left(H(\boldsymbol{\mathcal{I}} + \boldsymbol{\mathcal{D}}) \cdot \nabla_{\boldsymbol{x}}\Pi\right), \tag{3.27}$$

with $\boldsymbol{\mathcal{D}}$ given by (3.17). The result (3.27) shows that, as expected, shallow water gravity waves obey the wave equation. For symmetric arrays of seamounts with $\boldsymbol{\mathcal{D}} = D\boldsymbol{\mathcal{I}}$, the local gravity wave speed is given by $H_{\text{eff}}^{1/2}$, where $H_{\text{eff}} = H(1+D)$ is the non-dimensional effective depth (the dimensional units here being $\sqrt{gH_0}$). As discussed in the introduction, functional analysis techniques (e.g. Nandakumaran, 2007; Allaire, 2012; Mei and Vernescu, 2010, §5.5) applied to (3.27) when $\boldsymbol{\mathcal{D}} = D\boldsymbol{\mathcal{I}}$ reveals the Reuss–Voigt bounds $\bar{H} \equiv \langle h^{-1}\rangle^{-1} \leq H_{\text{eff}} \leq \langle h\rangle \equiv H$, with the lower (harmonic mean or Reuss) bound being attained exactly for propagation over a one-dimensional topography. In section 3.2 below the two-dimensional case is discussed in detail for the case of regular periodic arrays of circular cylinders.

3.2 The influence of topography on shallow water waves: regular arrays of seamounts

3.2.1 The effect of small-scale topography on the dispersion relation: a summary

First of all, a summary of results quantifying the effect of small-scale topography on the β-channel dispersion relations will be presented and discussed. Details of how

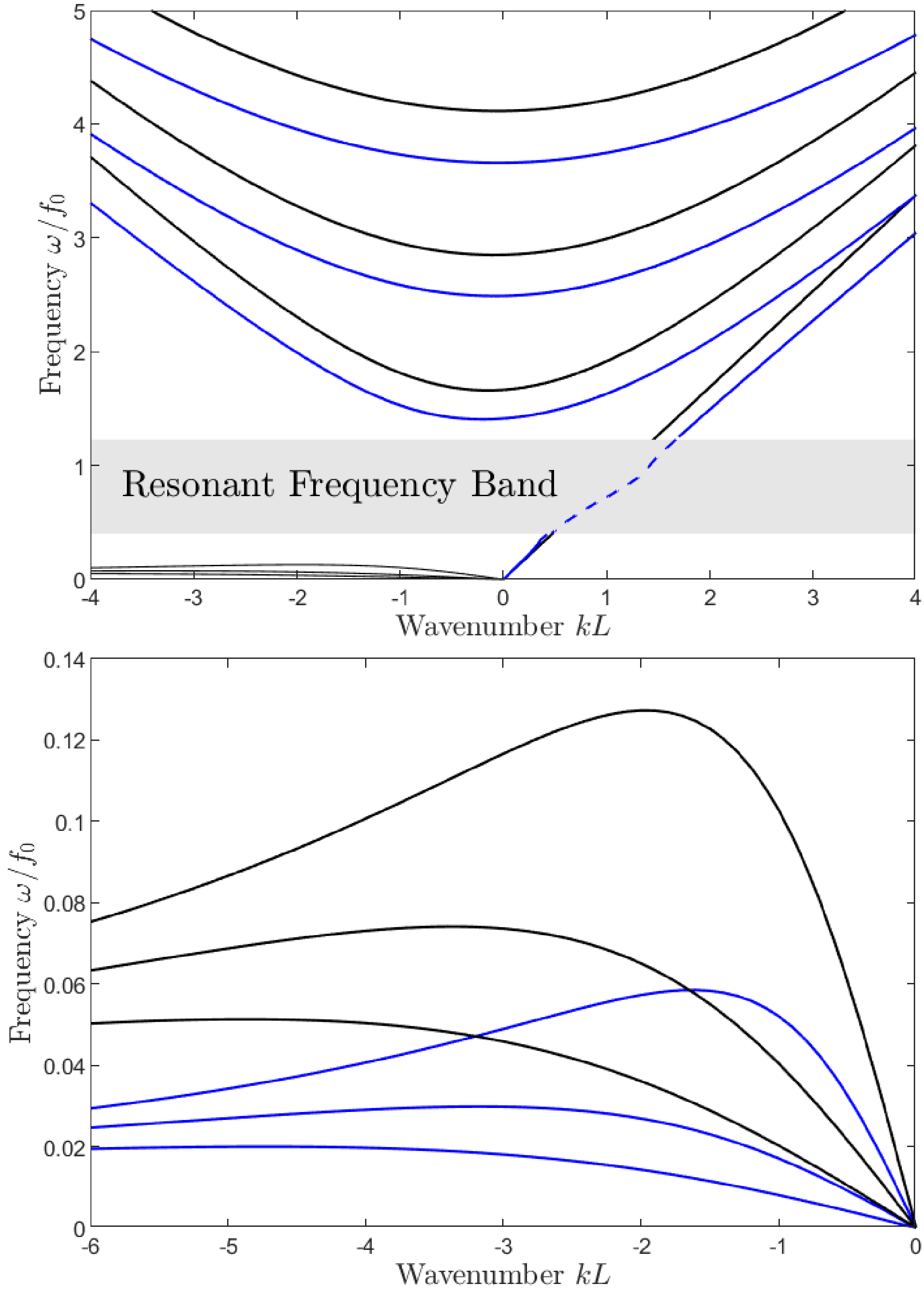

Figure 3.1: Dispersion relations for Poincaré, Rossby, and Kelvin waves with beta parameter $b = 0.5$, over (black curves) a flat-bottomed ocean of depth $H = 0.7135$, and (blue curves) a regular array of cylindrical seamounts with $h_+ = 1$, $h_- = 0.1$ (i.e. cylinder height $h_t = h_+ - h_- = 0.9$) covering area fraction $A = 1/\pi$. Only the first three branches of Poincaré and Rossby waves are shown in the upper panel, and the lower panel zooms in to show the Rossby waves more clearly. The dashed blue curve in the resonant frequency band shows the Kelvin wave solution in the extended equations when Ekman friction is present (see text).

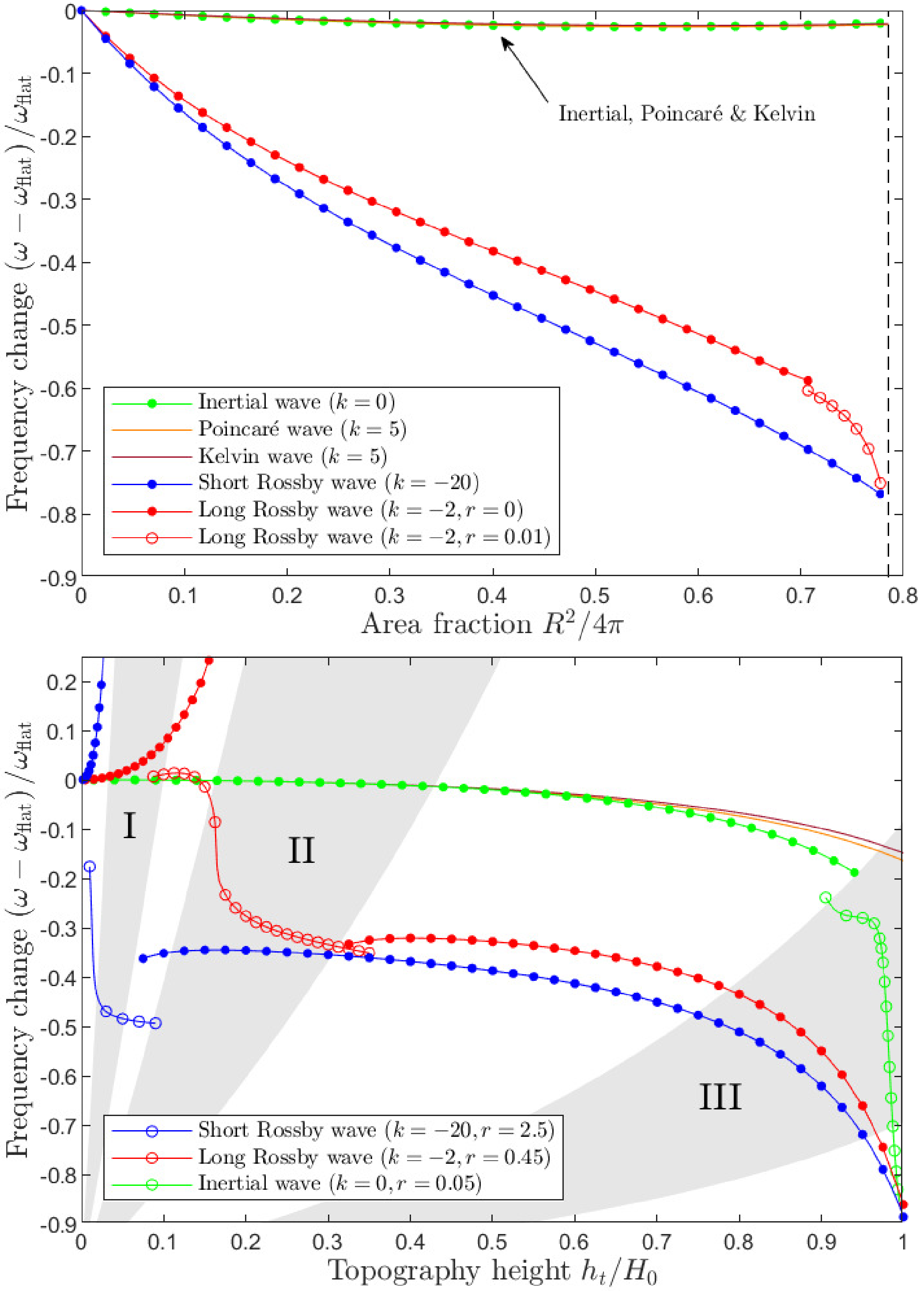

Figure 3.2: The effect of topography on the frequency of various wave types for $b = 0.5$, $h_+ = 1$, $h_- = 1 - h_t$ and cylinder area fraction A. Upper panel: Frequency change as a function of A for fixed topographic height $h_t = 0.5$. Note that the curves for the inertial, Poincaré, and Kelvin waves are near indistinguishable. Lower panel: Frequency change as a function of h_t for fixed area fraction $A = 1/\pi$. The shading shows the resonant regions for (I) the short Rossby wave, (II) the long Rossby wave, and (III) the inertial wave (for details see text). In both panels, curves with open circles show results when Ekman friction is present. These additional solutions are only plotted within and close to the relevant resonant regions.

the results are actually obtained, by numerical solution of (3.18), are postponed to the sections below. Results will be for regular periodic arrays of cylindrical seamounts, for which the topography is arranged in doubly periodic cells Ω defined on $\boldsymbol{X} \in (-\pi, \pi] \times (-\pi, \pi]$. The ocean depth is then given by

$$h(\boldsymbol{X}) = \begin{cases} h_- & |\boldsymbol{X}| \leq R \\ h_+ & |\boldsymbol{X}| > R \end{cases}, \tag{3.28}$$

i.e. the cylindrical seamounts have radius R, or cover area fraction $A = R^2/4\pi$, and have height $h_t = h_+ - h_-$.

First, to give an idea of the extent of the possible impact of small-scale topography, the blue curves in figure 3.1 show how the dispersion relation is changed in the presence of a rather extreme topography, for which $h_t = 0.9$, i.e. the height of the cylinders is 90% of the depth of the background ocean ($h_+ = 1$, $h_- = 0.1$), and the cylinder area fraction is $A = 1/\pi$ ($R = 2$). The black curves show the dispersion relations over a flat bottomed ocean, with a layer thickness given by the average ocean depth $H \approx 0.7135$ (the same numerical calculations performed in section 2.2.6, where h is replaced by H). The main results, summarising the effect of topography on the waves, are as follows: Poincaré waves are slightly slower, typically by around 20% including near-inertial waves, and Rossby waves are significantly slower, with their phase speed reduced by around 50%–60%. The Kelvin wave is slightly faster at small wavenumbers and slower at large wavenumbers, with the two regimes separated by a band of resonant wavenumbers within which Ekman friction effects must be considered to obtain physically reasonable results. The dashed blue curve shows a separate calculation for this region, based on numerical solutions of the extended equations (B.12), which include Ekman friction.

To illustrate how the results in figure 3.1 depend upon the topographic parameters, figure 3.2 shows the *relative* change in frequency for a set of representative waves. In the top panel, the frequency change is shown as a function of area fraction A (note that $A < \pi/4$, since $A = \pi/4$ corresponds to the cylinders touching), for the gravest inertial wave ($k = 0$, $n = 1$), a representative Poincaré wave ($k = 5$,

$n = 1$), a relatively short Kelvin wave ($k = 5$, chosen so that it is outside the resonant frequency band in figure 3.1), and both short $(k = -20)$ and long $(k = -2)$ Rossby waves. The topographic height is chosen as $h_t = 0.5$ (lower than for figure 3.1 where $h_t = 0.9$) and the beta parameter as $b = 0.5$. The results reinforce the impression from figure 3.1 that Rossby waves are affected much more than Kelvin or Poincaré waves. In fact, the contrast is even greater for the lower topography, because, as will be seen below, Rossby wave corrections are driven by resonances (or near resonances) with topographic Rossby waves on the seamounts, which can have a large effect even for low topography.

The lower panel shows how the results depend on the topographic height h_t. Curves for the six cases shown in the upper panel are plotted along with three further curves showing calculations with Ekman friction, which are included in order to give some indication of the behaviour in the (shaded) resonant regions. (Region (I) is resonant for the short Rossby wave, region (II) for the long Rossby wave and region (III) for the inertial wave.) The topography-induced change to the frequency for both the short and the long Rossby waves is seen to change sign as the resonant region is traversed, and the Ekman friction calculations give an idea of how the curves join in practice. The value of the Ekman friction r is chosen in each case to be close to the minimum required to obtain stable numerical results from (B.12) across the resonant region. As seen in the previous panel, Rossby waves are slowed by large-amplitude topography, but here can be seen to be accelerated by small-amplitude topography. Ekman friction, however, suppresses the acceleration at low amplitudes, and has comparatively little effect when the topography is large. The effect on inertial, Poincaré and Kelvin waves is once again relatively small except at extremely large h_t, when the inertial waves experience resonance and are slowed significantly (when Ekman friction is present).

In summary, all rSWE waves can experience resonance when their frequency approaches that of the trapped topographic Rossby waves, as has been reported for quasi-geostrophic Rossby waves by Vanneste (2000a,b) and Benilov (2000). The details vary by wave type. Rossby waves resonate only with relatively low topography, and inertial / Poincaré waves only for very large-amplitude topography. Kelvin waves will always experience resonance for some wavenumbers, for any topography supporting trapped waves, because their dispersion relation spans all frequencies.

Next, the calculations necessary to create figures 3.1 and 3.2 will be explained.

3.2.2 The first cell problem and the effective depth

Before an attempt can be made to solve (3.18), it is necessary to first solve the cell problems (3.14) and (3.15) defined on the doubly periodic cell Ω. The first of these, (3.14), is of particular interest because its solution allows the effective depth H_{eff} in the non-rotating problem to be determined.

For the case of the periodic array of cylindrical seamounts given by (3.28), (3.14) (dropping the i index as the problem is now identical up to a rotation for $i = 1$ and 2) simplifies to

$$\nabla_{\boldsymbol{X}}^2 \Phi^+ = 0, \quad \text{and} \quad \nabla_{\boldsymbol{X}}^2 \Phi^- = 0, \tag{3.29}$$

where the "$+$" and "$-$" indices correspond to parts of the solution in $|\boldsymbol{X}| > R$, and $|\boldsymbol{X}| < R$ respectively. The outer solution Φ^+ takes periodic boundary conditions on the edge of Ω. At the cylinder edge, the boundary conditions are

$$\begin{aligned} \Phi^+ &= \Phi^-, \\ h_+ \partial_\rho \Phi^+ - h_- \partial_\rho \Phi^- &= -\left(h_+ - h_-\right)\cos\theta, \end{aligned} \tag{3.30}$$

on $|\boldsymbol{X}| = R$, where (ρ, θ) are the usual polar coordinates for $\boldsymbol{X}$. For further discussion of the cylinder edge boundary conditions see Appendix D.

The cell problem (3.29-3.30) is a canonical problem arising in many areas of mathematical physics, most classically heat conduction through a two-dimensional porous medium with cylindrical occlusions (Rayleigh, 1892; Keller, 1963; McPhedran et al., 1988; Balagurov and Kashin, 2001) but also in electrostatics and optics (McPhedran and McKenzie, 1980) and in determining dielectric permittivity

(Godin, 2013). Our approach to solving (3.29-3.30), closely follows that of Godin (2013), and is based on a multipole expansion which exploits the rapid convergence of the Laurent series of the Weierstrass zeta function. Details are given in Appendix E.

Godin's method (see also Balagurov and Kashin, 2001) results in an infinite linear system which must be inverted in order to solve for Φ^+ and Φ^- and thus obtain H_{eff} exactly. However, it turns out that truncation of the system at very low order results in a sequence of increasingly accurate Padé approximants to the exact solution. Moreover, at low order these can be easily evaluated, for example the first three are given by

$$\begin{aligned} H_{\text{eff}}^{(0)} &= h_+ (1 - 2\gamma A) + O(A^{5/2}), \\ H_{\text{eff}}^{(1)} &= h_+ \left(\frac{1-\gamma A}{1+\gamma A}\right) + O(A^{9/2}), \\ H_{\text{eff}}^{(2)} &= h_+ \left(\frac{1-\gamma A - g_4\gamma^2 A^4}{1+\gamma A - g_4\gamma^2 A^4}\right) + O(A^{17/2}). \end{aligned} \tag{3.31}$$

Here, A is the cylinder area fraction (in our set-up $A = R^2/4\pi$) and $\gamma = (h_+ - h_-)/(h_+ + h_-)$, which hereafter will be termed the 'topography parameter', as it mediates how the topography influences the effective depth. Notice that $-1 < \gamma \leq 1$, with $\gamma = 1$ corresponding to an island, $\gamma = 0$ no topography and $\gamma \to -1$ a bottomless pit. For small topography of height h_b, $\gamma \approx h_b/2h_+$. The constant $g_4 \approx 0.305$ is obtained from the multipole expansion described in detail in Appendix E.

Figure 3.3 shows the effective depth H_{eff} for cylinders with height (left) $h_t = 0.9$ and (right) $h_t = 0.5$, as a function of the cylinder area fraction A. Note that the maximum possible area fraction is $A = \pi/4$, when the cylinders touch, and Godin's approach breaks down (Keller, 1963, describes the 'near-touching' regime). In each case H_{eff} (black circles) is obtained by a numerical calculation in which the linear system is truncated at 24 terms, which is found to be sufficient for convergence to machine precision for all results shown. As anticipated, $\bar{H} \leq H_{\text{eff}} \leq H$, i.e. H_{eff} in each case is seen to lie within the Reuss–Voigt bounds (dotted grey curves). Also plotted are the approximants $H_{\text{eff}}^{(0)}$, $H_{\text{eff}}^{(1)}$ and $H_{\text{eff}}^{(2)}$, showing that $H_{\text{eff}}^{(2)}$

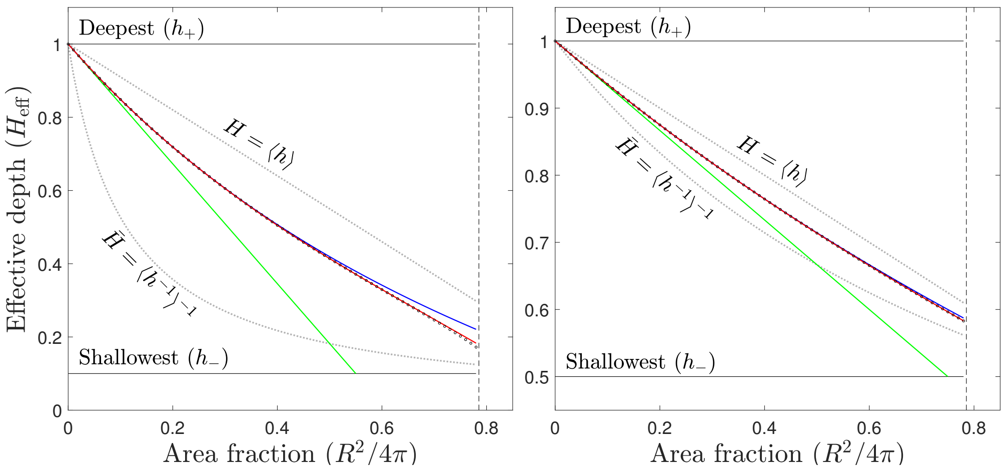

Figure 3.3: Effective depth H_{eff} (black circles) as a function of cylinder area fraction A in the cylindrical array problem with $h_+ = 1$, and topographic heights (left) $h_t \equiv h_+ - h_- = 0.9$ and (right) $h_t = 0.5$. Also plotted are the approximants $H_{\text{eff}}^{(i)}$ for $i = 0, 1, 2$ (green line, blue line, red line) and the arithmetic (H)/harmonic ($\bar{H}$) mean depths (upper/lower dotted grey curves).

gives an excellent approximation to the numerical result right up until the cylinders nearly touch. The zeroth-order approximant $H_{\text{eff}}^{(0)}$ is accurate for small area fraction, but diverges significantly from the numerical solution at larger A, and is is seen to violate the Reuss bound. This fact is important in assessing the limitations of results for randomly distributed seamounts in section 3.3, because the sparse seamount approximation ($A \ll 1$) used there turns out to be equivalent to using $H_{\text{eff}}^{(0)}$ to approximate H_{eff}. The results (3.31) have been further verified against figure 3 of Hu and Chan (2005), who plot the refractive index $(H/H_{\text{eff}})^{1/2}$ for the case of islands ($\gamma = 1$) as a function of area fraction A (see also Mei and Vernescu, 2010, §7.1, for an analogous result for acoustic waves). Excellent agreement is found (results not shown).

Finally, note that the difference between the effective depth H_{eff} and the mean depth H accounts entirely for the differences between the Poincaré and Kelvin wave dispersion relations at large wavenumber k seen in figure 3.1, because in the large k limit these waves do not feel rotation.

3.2.3 The second (rotating) cell problem

In this section the method used to solve the rotating cell problem (3.15), which is a new feature of the rSWE, is described. Recall that solutions of (3.15) are required in order to evaluate the topographic resonance functions $K_1(\alpha)$, and $K_2(\alpha)$ which appear in (3.18). In the cylindrical seamount case given by (3.28), (3.15) becomes (dropping the i index, and focussing on the $i = 1$ problem, which is sufficient due to symmetry)

$$\nabla^2_{\boldsymbol{X}} \Psi^{\pm}_{\alpha} = \nabla^2_{\boldsymbol{X}} G^{\pm} = 0, \tag{3.32}$$

with the boundary conditions

$$\begin{gathered} \Psi^{+}_{\alpha} = \Psi^{-}_{\alpha}, \quad \partial_\theta G^{+} = \partial_\theta G^{-}, \\ h_{+}\partial_\rho \Psi_\alpha - h_{-}\partial_\rho \Psi_\alpha = \partial_\rho G^{+} - \partial_\rho G^{-}, \\ \frac{\partial_\rho G^{+}}{h_{+}} - \frac{\partial_\rho G^{-}}{h_{-}} - \frac{\mathrm{i}\alpha}{R}\left(\frac{\partial_\theta G^{+}}{h_{+}} - \frac{\partial_\theta G^{-}}{h_{-}}\right) = -\left(\frac{1}{h_{+}} - \frac{1}{h_{-}}\right)\cos\theta, \end{gathered} \tag{3.33}$$

on $|\boldsymbol{X}| = R$. Here, the notation closely follows that for the non-rotating problem, and detailed derivations of the boundary conditions can be found in Appendix D. Full details of how the multipole expansion method of Godin (2013) is adapted to solve (3.32-3.33) are given in Appendix E.

Following the method for H_{eff} described above, the topographic resonance functions $K_1(\alpha)$ and $K_2(\alpha)$ are obtained from Godin's method by truncating and solving infinite linear systems, in which α appears as a parameter. The lowest-order truncations result in Padé approximants for $K_i(\alpha)$, namely $K_i^{(0)}$, $K_i^{(1)}$ etc., and explicit expressions for the leading three are given in (E.8-E.9).

The convergence of the sequences $K_{1,2}^{(i)}(\alpha) \to K_{1,2}(\alpha)$ is, however, more complicated than for $H_{\text{eff}}^{(i)} \to H_{\text{eff}}$ discussed above. To illustrate, figure 3.4 shows results for $i = 0, 1, 2$ (green/blue/red curves) and $i = 24$ (black circles). The complexity is introduced because the approximant functions $K_{1,2}^{(i)}(\alpha)$ each have i singularities (for $i > 1$) in $\alpha > 1$. In the limit $i \to \infty$, there are evidently an infinite number of these singularities, meaning that the 'true' $K_{1,2}(\alpha)$ cannot be described by rational functions of α. A similar problem, arising in electrostatics and optics, is analysed

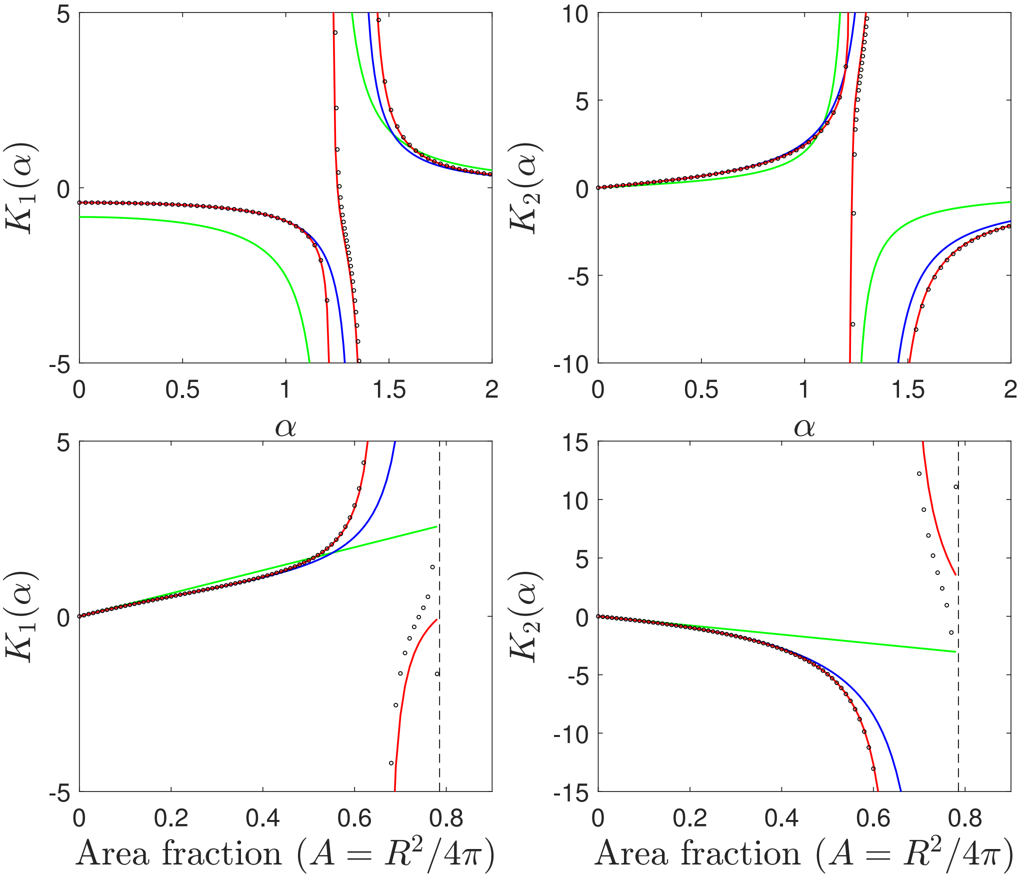

Figure 3.4: Values of $K_{1,2}^{(i)}(\alpha)$ plotted as functions of α and A. The low-order Padé approximants ($i = 0, 1, 2$) are shown with green, blue, and red lines respectively, and the 'true' Padé approximants ($i = 24$) are shown with circles. To give an idea of the convergence, only the main solution branches are plotted for each curve, e.g. in the first panel the 'true' K_1 has an infinite number of singularities in $1.2 \lesssim \alpha \lesssim 1.5$, which would be impossible to plot. The topographic height is fixed at $h_t = 0.9$, and the area fraction, and α are fixed at $A = 49/25\pi$, and $\alpha = 1.45$ in the top and bottom rows respectively.

in McPhedran and McKenzie (1980). Adapting their results to the present context, the locations of the singularities α_p (in $\alpha > 0$) are given by the formula

$$\alpha_p = \sqrt{\frac{1 - \lambda_p \gamma^2}{(1 - \lambda_p)\gamma^2}}, \tag{3.34}$$

where λ_p is the pth eigenvalue of the infinite matrix $\left(\boldsymbol{D}\boldsymbol{E}^T\boldsymbol{D}\right)^2$, given in appendix E. Further, it follows that the sequence $\{\alpha_p\}$ converges to an essential singularity at $\alpha_\infty = \lim_{p\to\infty} \alpha_p = \gamma^{-1}$. It turns out that, as is suggested by figure 3.4,

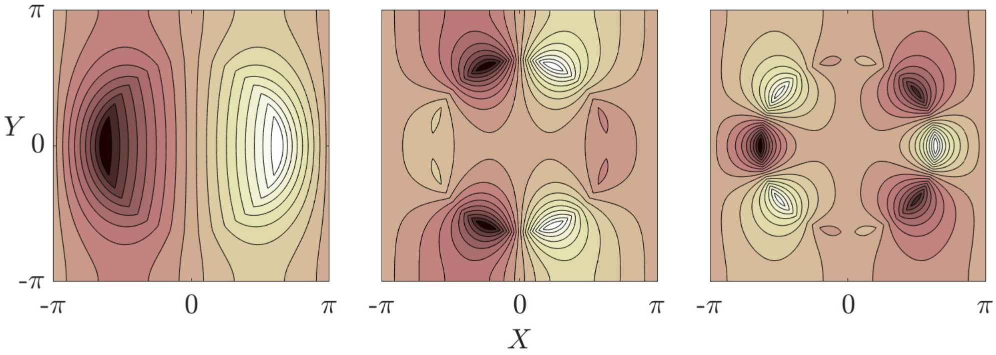

Figure 3.5: Spatial structure of the first three normal modes of the topographic array, illustrated by contouring $G_R = \mathrm{Re}\,\{\psi\}$. The cylindrical seamounts have radius $R = 2$ (area fraction $A = 1/\pi$) and height $h_t \equiv h_+ - h_- = 0.9$.

all singularities are confined to a narrow range of α, which expands slowly as the area fraction increases towards its maximum value. The low-order approximants do a good job away from the resonant band, and as the order increases they capture the location of the leading singularities with increasing accuracy.

Physically, the singularities in $K_{1,2}(\alpha)$ at $\alpha = \alpha_p$ ($p \geq 1$) occur due to the excitation of the normal modes of the topographic Rossby waves which propagate around the edges of the cylindrical seamounts (Jansons and Johnson, 1988; Benilov, 2000; Vanneste, 2000a; Longuet-Higgins, 1967). That the singularities all occur in $\alpha > 1$ is related to the topographic Rossby wave frequencies being bounded above by the inertial frequency. If a large-scale wave has a frequency which matches the frequency of one of these normal modes, a resonant excitation will occur which requires Ekman friction or another form of dissipation to regularise. The structure of the streamfunction of the first three normal modes is shown in figure 3.5. In practice, if a small amount of friction is added to the system, the effect of the higher modes is negligible compared with the first mode, due to the weak correlation between their fine-scale structure and that of the topography itself. The lower row in figure 3.4 shows how $K_{1,2}(\alpha)$ depend on the area fraction of the topography, for fixed $\alpha = 1.45$. The resonant band is seen to be located around $A \approx 0.64$.

In summary, the convergence issues with the functions $K_i(\alpha)$ present difficulties for the numerical solution of (3.18). Consequently, solutions of (3.18) are treated as valid only if no singularities of $K_i((1 + by)/\omega)$ are present within the computational domain. This condition defines the ‘resonant regions’ in figures 3.1 and 3.2) (or, strictly speaking, the non-resonant regions). Solutions given within the resonant regions use the extended system (B.12) to include Ekman friction, and are therefore regularised.

3.2.4 Numerical solution of (3.18)

Once the functions $K_1(\alpha)$, $K_2(\alpha)$ and D are found to the required accuracy, (3.18) can be solved numerically. The numerical method used is just a generalisation of that used in section 2.2.6.1. First, solutions $\propto \exp(\mathrm{i}kx)$ are sought for fixed wavenumber k, reducing the system to a first-order system of ODEs in the y-variable, defined on the interval $[-1, 1]$. This system is again suited to a Chebyshev spectral method ($N = 96$ is used here), the flat-bottomed eigenvalue problem (2.97) is retrieved by setting $K_1(\alpha) = K_2(\alpha) = D = 0$, and implementing the boundary conditions $V(\pm 1) = 0$.

When topography is present the matrices $\boldsymbol{A}$ and $\boldsymbol{B}$ in (2.97) themselves depend on ω, through the arguments of $K_1(\cdot)$ and $K_2(\cdot)$, and the method above must be adapted. The matrices are again determined by removing the rows and columns in positions $N + 2$ and $2N + 2$ from the block matrices

$$\boldsymbol{A}(\omega) = \left(\begin{array}{c|c|c} \boldsymbol{\mathcal{I}} + \boldsymbol{f}^2\boldsymbol{K}_1 + \boldsymbol{f}\boldsymbol{K}_2 & 0 & 0 \\ \hline 0 & \boldsymbol{\mathcal{I}} + \boldsymbol{f}^2\boldsymbol{K}_1 + \boldsymbol{f}\boldsymbol{K}_2 & 0 \\ \hline 0 & 0 & \boldsymbol{\mathcal{I}} \end{array}\right), \tag{3.35}$$

$$\boldsymbol{B}(\omega) = \left(\begin{array}{c|c|c} 0 & -\boldsymbol{f}\left(\boldsymbol{\mathcal{I}} + \boldsymbol{K}_1 + \boldsymbol{f}\boldsymbol{K}_2\right) & \mathrm{i}k(1+D)\boldsymbol{\mathcal{I}} \\ \hline \boldsymbol{f}\left(\boldsymbol{\mathcal{I}} + \boldsymbol{K}_1 + \boldsymbol{f}\boldsymbol{K}_2\right) & 0 & -(1+D)\boldsymbol{D}_y \\ \hline \mathrm{i}kH\boldsymbol{\mathcal{I}} & H\boldsymbol{D}_y & 0 \end{array}\right), \tag{3.36}$$

where $\boldsymbol{f} = \mathrm{diag}(1 + by_1, \cdots, 1 + by_{N+1})$, $\boldsymbol{\mathcal{I}}$ is the identity matrix, $\boldsymbol{D}_y$ is the Chebyshev differentiation matrix and now

$$\boldsymbol{K}_i(\omega) = \mathrm{diag}\left(K_i\left(\frac{1 + by_1}{\omega}\right), \cdots, K_i\left(\frac{1 + by_{N+1}}{\omega}\right)\right), \tag{3.37}$$

for $i = 1, 2$. For simplicity, we reuse the matrix variable names after removing the rows and columns corresponding to the boundary points.

Our approach is to use a fixed-point iteration method, by writing

$$-\,\mathrm{i}\omega_n \boldsymbol{A}\left(\omega_{n-1}\right)\boldsymbol{v}_n + \boldsymbol{B}\left(\omega_{n-1}\right)\boldsymbol{v}_n = 0, \tag{3.38}$$

for iteration n, and using the flat-bottomed frequency for the initial guess ω_0. The idea is that repeated solution of (3.38) will lead to the convergence of ω_n and $\boldsymbol{v}_n$ to the desired solutions ω and $\boldsymbol{v}$. While basic, this method works well in the sense that analogues of all flat-bottomed solutions can be routinely found using around 20 iterations (for near-machine accuracy), even for extreme topographies.

A further constraint on the numerical solutions is that, once ω is known, $K_i((1+by)/\omega)$ must be non-singular throughout the domain $y \in [-1, 1]$. Otherwise a resonance is evidently present, and the numerical solution of (3.38) does not make sense, not least because the discrete grid cannot handle singularities. For each singular point α_p of $K_i(\alpha)$, all frequencies in the interval $\omega \in [(1-b)\alpha_p^{-1}, (1+b)\alpha_p^{-1}]$ will have a singularity somewhere in the domain. The resonant frequency band is therefore defined to be the union over all p of these intervals. To find meaningful solutions in the resonant frequency band, it is necessary to add finite Ekman friction to the system and solve the resulting extended equations detailed in Appendix B. These Ekman friction calculations have been implemented by the same method, allowing our calculations to be extended into the resonant band.

3.2.5 Approximate formulae for the dispersion relations

Numerical calculation of the dispersion relation using (3.18) is, as described above, a complicated multi-step process. In practice it is arguably more insightful to have approximate formulae for the topographic effect, for example analogues of the $b \ll 1$ dispersion relations (2.105), (2.109) and (2.111) for the flat-bottomed case. It turns out that different approaches to obtain such formulae are necessary for Poincaré and Kelvin waves versus Rossby waves, and each will be considered in turn. It is important to emphasise that the limit $b \ll 1$ does not equate to the quasi-geostrophic limit, which also requires the topography to be $O(b)$, and that the results in the following two subsections are therefore valid for finite topographies.

3.2.5.1 Poincaré and Kelvin waves

Consider the limit $b \ll 1$ in which Poincaré waves and Kelvin waves have frequencies of order unity. (A separate regime in which the Kelvin wave has frequency $O(b)$ is not considered here.) In the limit $b \ll 1$, the Taylor expansion

$$K_{1,2}\left(\tfrac{1}{\omega}+b\tfrac{y}{\omega}\right)=K_{1,2}\left(\tfrac{1}{\omega}\right)+b\tfrac{y}{\omega}K_{1,2}'\left(\tfrac{1}{\omega}\right)+O(b^2),$$

can be used to simplify (3.18), which at leading order in b becomes

$$\begin{aligned}-\mathrm{i}\omega\left(1+\tfrac{1}{\omega^2}K_1\left(\tfrac{1}{\omega}\right)+\tfrac{1}{\omega}K_2\left(\tfrac{1}{\omega}\right)\right)\boldsymbol{U}+&\\ \left(1+K_1\left(\tfrac{1}{\omega}\right)+\tfrac{1}{\omega}K_2\left(\tfrac{1}{\omega}\right)\right)\boldsymbol{k}\times\boldsymbol{U}&=-\left(1+D\right)\nabla_{\boldsymbol{x}}\Pi,\\ -\mathrm{i}\omega\Pi+H\nabla_{\boldsymbol{x}}\cdot\boldsymbol{U}&=0,\end{aligned}\tag{3.39}$$

with channel wall boundary conditions $V(\pm 1)=0$. Mathematically, the absence of explicit y-dependence in equation (3.39) simplifies matters compared with (3.18), and harmonic wave solutions $\propto \exp\left(\mathrm{i}\left(kx+ly\right)\right)$ can be sought (we take $l=n\pi/2$ for ease of comparison with the results above). The result is the following nonlinear equation determining the dispersion relation

$$\left(1-\omega^2\right)\left[K_1\left(\tfrac{1}{\omega}\right)^2-\left(\omega+K_2\left(\tfrac{1}{\omega}\right)\right)^2\right]-H_{\mathrm{eff}}\left(\omega^2+K_1\left(\tfrac{1}{\omega}\right)+\omega K_2\left(\tfrac{1}{\omega}\right)\right)\kappa_n^2=0,\tag{3.40}$$

where $\kappa_n^2 = k^2+n^2\pi^2/4$. In general, the solution branches of (3.40) must be found numerically using a standard root finding method, although, because it is a single-variable equation, this is evidently much simpler than solving (3.18). For short waves with $\omega \gg 1$ (i.e. $\kappa_n \gg 1$), the resonance functions $K_{1,2}(\alpha)$ can be approximated by their value at $\alpha=0$, and using the fact that $K_2(0)=0$, the result simplifies further to

$$\omega_P^2 = \tfrac{1}{2}\left(1 + \kappa_n^2 H_{\text{eff}} + K_0^2\right) + \tfrac{1}{2}\left((1 + \kappa_n^2 H_{\text{eff}} + K_0^2)^2 + 4K_0^2 - 4K_0\kappa_n^2 H_{\text{eff}}\right)^{1/2} \tag{3.41}$$

Here, H_{eff} and $K_0 \equiv K_1(0)$ are constants determined by the topography which, in the case of regular cylinders, allows for progressively more accurate approximations to be obtained from (3.31) and (E.8) respectively. For example, the zeroth-order approximations are $H_{\text{eff}} = h_+(1 - 2\gamma A)$ and $K_0 = -2\gamma^2 A$, which are accurate for low area fraction A. The result (3.41) can be compared with the flat-bottomed formula (2.109) with $h = H$, which is recovered by setting $\gamma = 0$ or $A = 0$.

For the Kelvin wave it suffices to set $V = 0$ in (3.39) and, following the analysis of the flat-bottomed case, it follows that

$$\omega^2 + K_1\left(\tfrac{1}{\omega}\right) + \omega K_2\left(\tfrac{1}{\omega}\right) = k^2 H_{\text{eff}}. \tag{3.42}$$

Once again, this is a nonlinear equation, which must be solved numerically using a root finding method to obtain the Kelvin wave dispersion relation. The short wave result ($\omega \gg 1$) is

$$\omega_K^2 = k^2 H_{\text{eff}} - K_0, \tag{3.43}$$

which can be compared with (2.105) with $h = H$.

3.2.5.2 Rossby waves

Rossby waves frequencies are $O(b)$ in the limit $b \ll 1$, therefore to obtain approximate formulae the asymptotic forms of $K_1(\alpha)$ and $K_2(\alpha)$ are required for $\alpha \gg 1$. For the case of the regular array of cylinders they are

$$K_1(\alpha) = \frac{c_2}{\alpha^2} + \frac{c_4}{\alpha^4} + \cdots, \quad K_2(\alpha) = \frac{d_1}{\alpha} + \frac{d_3}{\alpha^3} + \cdots,$$

where the sequences of constants $\{c_i\}$ and $\{d_i\}$ can be determined to the required accuracy by expanding the formulae in (E.8) and (E.9). For example, the zeroth-order approximations to the first coefficients are $c_2 = 2A$ and $d_1 = -2\gamma A$.

Retaining terms in (3.18) up to $O(b)$, it follows that

$$-\mathrm{i}\omega\left(1+c_2+d_1\right)\boldsymbol{U}+\left(1+by\right)\left(1+d_1\right)\boldsymbol{k}\times\boldsymbol{U}=-\left(1+D\right)\nabla_{\boldsymbol{x}}\Pi,$$
$$-\mathrm{i}\omega\Pi+H\nabla_{\boldsymbol{x}}\cdot\boldsymbol{U}=0. \qquad (3.44)$$

The leading-order Rossby wave dispersion relation is then found to be

$$\begin{aligned}\omega_R&=-\frac{kb\left(1+d_1\right)H_{\text{eff}}}{\left(1+d_1\right)^2+\left(1+c_2+d_1\right)H_{\text{eff}}\kappa_n^2},\\ &\approx-\frac{kbh_+\left(1-2\gamma A\right)}{\left(1-2\gamma A\right)+\left(1+2(1-\gamma)A\right)\kappa_n^2h_+},\end{aligned} \qquad (3.45)$$

where the second expression uses the zeroth-order approximations for H_{eff}, c_2 and d_1, which are valid for low area fraction $A \ll 1$. The dispersion relation (3.45) can be compared with its flat-bottomed counterpart (2.111) with $h = H$.

Some asymptotic dispersion relations are plotted in figure 3.6 for a topography with relatively large height ($h_t = 0.9$), and area fraction ($A = 1/\pi$), and at finite $b = 0.5$, in order to test the validity of the approximations by comparison with numerical solutions of (3.18). Because A is relatively large, the second-order approximants are used for H_{eff} and $K_{1,2}$. Agreement between the full solution of (3.18) and the asymptotics is seen to be good, even at this relatively large value of b, and further tests with lower values of b have confirmed the expected rate of convergence.

3.2.6 Quasi-geostrophic regime

In this section our focus is the quasi-geostrophic regime which, as discussed in section 3.1.2 above, requires not only $b \ll 1$, as in the preceding sections, but also $O(b)$ topography. Writing $h_t = bh_b$, and applying the methods described above to (3.25) results in the following nonlinear equation for the Rossby wave dispersion relation for the scaled frequency $\Omega = \omega/b$,

$$\Omega+\frac{k}{1+\kappa_n^2}+\frac{\kappa_n^2}{\Omega(1+\kappa_n^2)}\tilde{K}\left(\tfrac{1}{\Omega}\right)=0. \qquad (3.46)$$

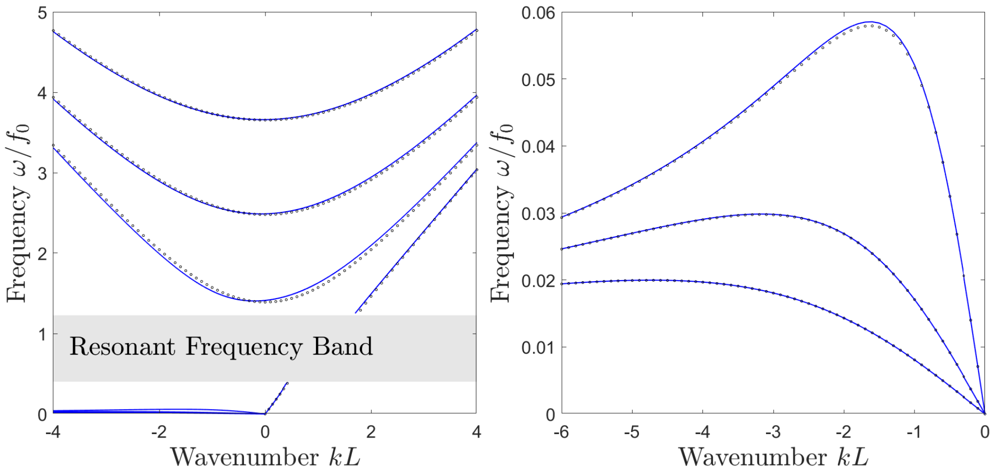

Figure 3.6: Frequency plotted against wavenumber for the Kelvin wave, and the first three modes $(n = 1, 2, 3)$ of the Rossby waves and Poincaré waves for $b = 0.5$, $h_+ = 1$ and cylinder height $h_t = h_+ - h_- = 0.9$. Shown here is the full numerical solution to (3.18) (blue lines), and the leading-order asymptotics (3.40), (3.42) and (3.45), using the approximants $H_{\text{eff}}^{(2)}$, $K_{1,2}^{(2)}(\alpha)$ (black circles). The left panel shows the dispersion relations of all three wave types, and the right panel shows only a close-up of the Rossby waves.

The function $\tilde{K}(\alpha)$ is defined using the solution of the quasi-geostrophic cell problem (3.24), and is the quasi-geostrophic analogue of K_1 ($K_2 \to 0$ in the quasi-geostrophic limit). The first three approximants are given by (E.10). Using the zeroth-order approximant in (3.46) recovers the dispersion relation found in Vanneste (2000b) and Benilov (2000) for widely separated seamounts. The use of more accurate approximants for $\tilde{K}$ in (E.10) therefore extends these previous results to the case of more densely packed regular topography.

It is interesting that the quasi-geostrophic limit where $h_t = O(b)$ results in a qualitatively different formula (3.46) for the Rossby wave dispersion relation compared with the finite topography limit (3.45) where $h_t = O(1)$. Specifically, the quasi-geostrophic formula allows for the possibility of resonant behaviour, while the finite topography formula involves just a quantitative modification of the flat-bottomed formula. The explanation is that the finite topography, $b \ll 1$ limit *excludes* resonance because the long Rossby wave frequency becomes $O(b)$ while the trapped topographic Rossby waves retain $O(1)$ frequency. In the quasi-geostrophic limit, by contrast, both the long waves and the trapped waves have $O(b)$ frequency,

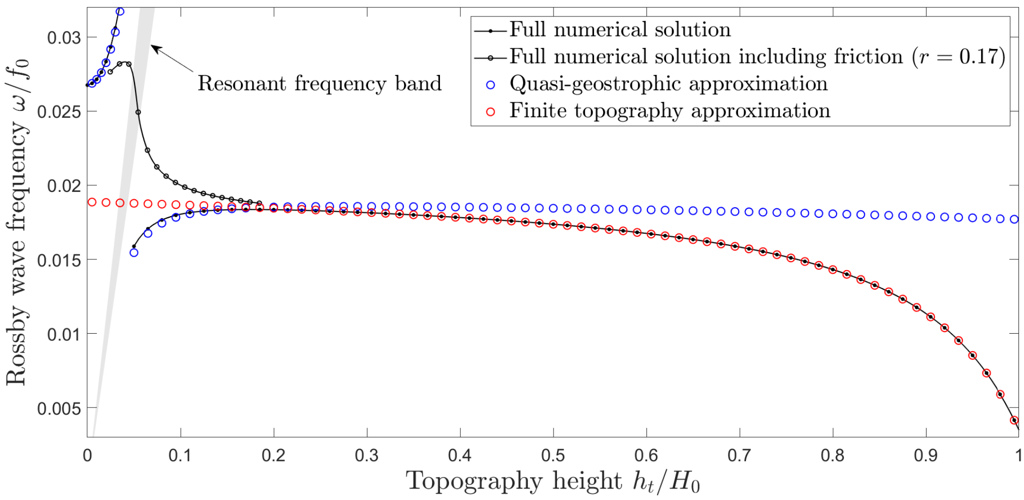

Figure 3.7: Rossby wave frequency against topographic depth for a fixed wavenumber $(k, l) = (-\pi/2, \pi/2)$, $b = 0.1$ and area fraction $1/\pi$. Shown are the full numerical solution (black curves), the finite topography approximation calculated using $K_{1,2}^{(2)}(\alpha)$ (red circles), and the quasi-geostrophic approximation calculated using $\tilde{K}^{(2)}(\alpha)$ (blue circles). The shaded region indicates the range of frequencies which are prohibited by resonance, and the numerical solution including friction ($r = 0.17$) is included, joining the two solution regions.

and therefore resonance remains possible.

To investigate the regimes of validity of the quasi-geostrophic and finite topography approximations, figure 3.7 compares the calculated frequencies to those of the full rSWE, obtained from numerical solutions of (3.18). The comparison is for $b = 0.1$, and a topography of regular periodic cylinders across the full range of topographic heights h_t, with cylinder area fraction $A = 1/\pi$. In the full system resonance is found to occur when h_t is around 0.04 to 0.06, which can be regularised with e.g. Ekman friction. The quasi-geostrophic formula (3.46) captures the full dispersion curve behaviour quite accurately close to the resonance, while the finite topography result (3.45) evidently does not. As the topography amplitude is increased beyond $h_t \approx 0.3$, however, the quasi-geostrophic approximation is increasingly inaccurate, and the finite topography result captures the full rSWE behaviour well. In practice, therefore, each approximation has its own domain of validity.

3.3 Randomly distributed seamounts

The regular periodic seamounts covered in the previous section have the advantage that the rSWE dispersion relations can be calculated accurately for arbitrary seamount height h_t and area coverage A. However, with respect to the ocean this 'regular array' topography is obviously artificial. In particular, resonance effects will be unduly amplified, because the topographic Rossby wave at every seamount (at the same latitude y) has the same frequency. It is evidently worthwhile to compare the results above with those for a randomised topography in which seamount location, height and radius are governed by a specified distribution. The drawback of considering a randomised distribution, as shown previously in the quasi-geostrophic case (Vanneste, 2000b; Benilov, 2000), is that in order for the problem to be tractable an assumption of widely separated seamounts must be made, i.e. the area fraction $A \ll 1$. As will be shown, this approximation turns out to be equivalent to using the zeroth-order approximants $H_{\text{eff}}^{(0)}$, $K_i^{(0)}$ for the effective depth and topographic resonance functions which, as can be seen in figure 3.3 and figure 3.4, become inaccurate at finite A.

To examine the effect of randomly distributed seamounts the averaging operator (3.3) needs careful interpretation. The region $\Omega = \Omega(\boldsymbol{x})$ formally becomes a region centred on $\boldsymbol{x}$ that is asymptotically intermediate in scale between the large and small length scales. In this asymptotic regime, for a suitable randomly generated field g in (3.3), the averaged field $\langle g \rangle$ will be independent of the details of Ω. In practice, it is not straightforward to make calculations with (3.3) unless the function g can be linearly decomposed into contributions from each mountain in Ω, i.e. interactions between mountains can be neglected so that (suppressing $\boldsymbol{x}$-dependency)

$$g(\boldsymbol{X}) \approx \sum_{i=1}^{N} g_1(\boldsymbol{X} - \boldsymbol{X}_i, R_i, \gamma_i) \tag{3.47}$$

where $\boldsymbol{X}_i$ is the location of the ith mountain, and $g_1(\boldsymbol{X}, R, \gamma)$ is the contribution to g from a single seamount of radius R and topography parameter γ at the origin. Inserting (3.47) into (3.3), and exploiting the fact the region Ω is large, allows the joint limit $N \to \infty$, $\Omega \to \infty$ to be taken. A number density $n(R, \gamma)$ can now be introduced, defined so that the number of seamounts with radius $\in [R, R + \mathrm{d}R)$ and topography parameter $\in [\gamma, \gamma + \mathrm{d}\gamma)$ in a small area $\mathrm{d}\boldsymbol{X}$ is $n(R, \gamma)\,\mathrm{d}R\,\mathrm{d}\gamma\,\mathrm{d}\boldsymbol{X}$. This allows the sum in (3.47) to be replaced with integrals in (3.3), which can each be centred on the origin by change of variables so that

$$\langle g \rangle = \int_{-1}^{1} \int_{0}^{\infty} \int_{\mathbb{R}^2} g_1(\boldsymbol{X}, R, \gamma)\, n(R, \gamma)\, \mathrm{d}\boldsymbol{X}\, \mathrm{d}R\, \mathrm{d}\gamma. \tag{3.48}$$

Next, consider the averaging operator (3.48) as applied to equation (3.17) to determine H_{eff} for the case of cylindrical topography distributed according to $n(R, \gamma)$. The first cell problem (3.29-3.30) is greatly simplified compared with the doubly periodic case, as it need only be solved in $\mathbb{R}^2$, using standard polar coordinates. The solution ($\Phi^+ = \gamma R^2 \cos\theta/\rho$, $\Phi^- = \gamma\rho\cos\theta$) is equal to the zeroth-order solution for seamounts in the doubly-periodic domain given in Appendix E.1. In other words, the zeroth-order small R approximation in the doubly periodic case and the non-interacting seamount approximation in (3.47) are equivalent. Inserting the solutions into (3.17) gives

$$H_{\text{eff}} = h_+ \left(1 - 2 \int_{-1}^{1} \int_{0}^{\infty} \pi R^2 \gamma\, n(R, \gamma)\, \mathrm{d}R\, \mathrm{d}\gamma\right). \tag{3.49}$$

The expression (3.49) for H_{eff} simplifies further if it is assumed that $n(R, \gamma)$ is separable, i.e.

$$n(R, \gamma) = \frac{A}{a_0}\, p_R(R)\, p_\gamma(\gamma), \tag{3.50}$$

where $A \ll 1$ is the area fraction covered by seamounts as above, $a_0 = \int_0^\infty \pi R^2 p_R(R)\, \mathrm{d}R$ is the average seamount area, $p_R(R)$ is the probability density function of the cylinder radii and $p_\gamma(\gamma)$ is the probability density function of the height parameter. In this case

$$H_{\text{eff}} = h_+ \left(1 - 2A \int_{-1}^{1} \gamma\, p_\gamma(\gamma)\, \mathrm{d}\gamma\right), \tag{3.51}$$

from which the zeroth-order doubly periodic result in (3.31) is recovered, independently of the choice of $p_R(R)$, by setting the heights of all cylinders to be equal, i.e. $p_\gamma(\gamma) = \delta(\gamma - \gamma_0)$ for constant γ_0.

The topographic resonance functions can be calculated similarly, and the results are

$$\begin{aligned} K_1(\alpha) &= -\int_{-1}^{1}\int_0^\infty \frac{2\pi R^2\gamma^2}{1-\alpha^2\gamma^2}\, n(R,\gamma)\, \mathrm{d}R\, \mathrm{d}\gamma \quad \left(= -2A\int_{-1}^{1} \frac{\gamma^2 p_\gamma(\gamma)}{1-\alpha^2\gamma^2}\, \mathrm{d}\gamma\right) \\ K_2(\alpha) &= \alpha\int_{-1}^{1}\int_0^\infty \frac{2\pi R^2\gamma^3}{1-\alpha^2\gamma^2}\, n(R,\gamma)\, \mathrm{d}R\, \mathrm{d}\gamma \quad \left(= 2\alpha A\int_{-1}^{1} \frac{\gamma^3 p_\gamma(\gamma)}{1-\alpha^2\gamma^2}\, \mathrm{d}\gamma\right). \end{aligned} \tag{3.52}$$

The terms in brackets show the results for the separable case, which reduce to the zeroth-order expressions in (E.8-E.9) for seamounts of constant height.

The results (3.49-3.52) allow (3.18) to be solved numerically using the methods of section 3.2 above. It is also possible to obtain analytical results by exploiting the smallness of A, employing a regular expansion for the frequency of the form

$$\omega = \omega_0 + A\omega_1 + O(A^2), \tag{3.53}$$

and thereby obtaining the leading-order corrections to the dispersion relations (cf. Vanneste, 2000b, for the quasi-geostrophic case). Here, we present numerical results for cylindrical seamounts which are uniformly distributed in height, with the depth over the seamounts in the range $h_{\min} < h_- < h_{\max}$, and with a separable number density (3.50). This situation corresponds to

$$p_\gamma(\gamma) = \begin{cases} \dfrac{(1+\gamma_+)(1+\gamma_-)}{(\gamma_+ - \gamma_-)}\dfrac{1}{(\gamma+1)^2} & \gamma_- < \gamma < \gamma_+ \\ 0 & \text{otherwise} \end{cases}, \tag{3.54}$$

where $\gamma_- = (h_+ - h_{\max})/(h_+ + h_{\max})$ and $\gamma_+ = (h_+ - h_{\min})/(h_+ + h_{\min})$. Recall that $p_R(R)$ is arbitrary in this set-up, because the results depend only on the area fraction A.

Figure 3.8 shows results for the distribution (3.54) with $h_{\min} = 0.1$ and

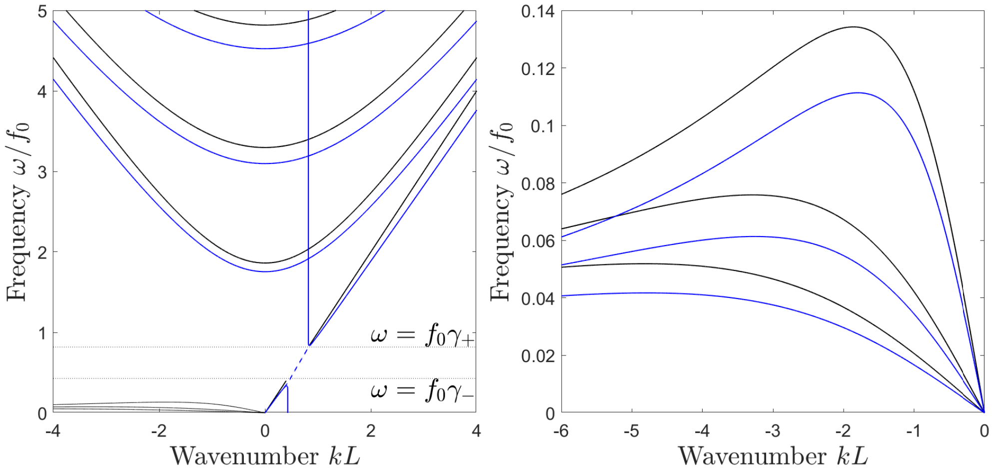

Figure 3.8: Dispersion relations for mountains distributed according to (3.54) with $h_{\min} = 0.1$ and $h_{\max} = 0.4$. The beta parameter $b = 0.5$ and area coverage $A = 0.1$. Black curves show the flat-bottomed solution and blue curves show the solution with topography present. The dashed blue curve shows the solution when friction is present, and is plotted only between the two logarithmic resonances, indicated by the dotted lines. The left panel shows the dispersion relations of all three wave types, and the right panel shows only a close-up of the Rossby waves.

$h_{\max} = 0.4$, and $A = 0.1$, which represents a range of tall cylindrical seamounts which, compared with the scenario shown in figure 3.1 (where $A = 1/\pi$), have a significantly lower area coverage. Qualitatively, the effect of the topography is similar (although weaker) compared to the constant height case nearly everywhere, except close to the resonant region for the Kelvin waves. In the Kelvin wave dispersion relation, singularities are present at $\omega = \gamma_\pm$ (dimensionally $f_0\gamma_\pm$). It is perhaps surprising that the dispersion relation contains any singularities at all when the heights of the seamounts are distributed, but as shown by Benilov (2000) for Rossby waves in the quasi-geostrophic case, the integrals in (3.52) result in logarithmic singularities at the endpoints of the distribution at $\gamma_\pm$. This translates into *logarithmic* singularities in the dispersion relations at $\omega = \gamma_\pm$, which, much more than the algebraic singularities which occur when the seamount heights are constant, are smoothly regularised by the addition of relatively weak Ekman friction. The dashed blue curve shows the solution of the extended system (B.14) with Ekman friction parameter $r = 0.1$.

3.4 Discussion

The main results of this chapter are summarised in figures 3.1, 3.2 and 3.8, which shows the extent to which finite-amplitude topography can influence Rossby, Kelvin and Poincaré wave speeds compared to the flat-bottomed case. Our results have been presented to illustrate the extent of the error that will necessarily be introduced in ocean general circulation models, due to using the mean ocean depth in place of the fully resolved small-scale topography. Clearly, significant errors in Rossby wave speeds in particular are possible, due either to large-amplitude topography with significant area coverage, or due to resonance between the Rossby wave and trapped topographic Rossby waves over seamounts. How significant the latter effect is in the ocean (also for Kelvin waves) remains an open question. Certainly the impact of resonance is reduced, although not removed entirely, by using a distribution of topographic heights in place of topography with a single height. Another reason resonance may not be so important in practice is that, as noted in the conclusions of Vanneste (2000b), in the typical ocean situation the frequency of the trapped topographic Rossby waves will usually be higher than that of the propagating Rossby waves, meaning the topography will not resonate but will act to slow the Rossby wave propagation speed. The corrected dispersion relation (3.45), which quantifies this effect in the finite-amplitude ($b \ll 1$) regime, gives a useful insight into its magnitude.

As a final comment, it is worth emphasising that the value of the results presented here is not limited to oceanography. The rSWE are used in many other fields, perhaps most relevantly in atmospheric science, where they provide a valuable reduced model describing wave propagation through a stably stratified atmosphere. In this perspective, the 'topography' can represent not physical topography per se, but small-scale regions of reduced stratification due to the presence of e.g. distributions of convective clouds. The approach taken here may therefore be of value in quantifying how, for example, equatorial wave speeds are modified by unresolved cloud fields (see also e.g. Biello and Majda, 2005), with implications for their parametrisation.

Chapter 4

Wave propagation in a stratified atmosphere in the presence of small-scale, convective clouds

In this chapter we investigate how the method of homogenisation may be used to study the propagation of waves in a stratified atmosphere in the presence of a small-scale, convective cloud field. Whilst chapter 3 which studies how obstacles may influence wave propagation in a vertically homogenous, shallow fluid layer has implications and consequences for the atmosphere, a fuller picture of atmospheric dynamics may be established by considering additional physical phenomena. The following study focusses on wave propagation in a stably stratified, Boussinesq atmosphere (see section 2.2.3 for details).

The multi-scale interaction between long waves and convection has previously been studied by Biello and Majda (2010, 2005) and Majda and Klein (2003). In these works, the focus has been on tropical waves interacting with synoptic-scale convective structures (with horizontal scale $\sim$ 1500km). In this regime, the structures of interest are convective, intraseasonal oscillations such as the Madden-Julian Oscillation. As such, the multi-scale asymptotic procedures focus on the case in which the structures are hydrostatic and small-scale only in the latitudinal direction, and enter the large-scale equations through forcing terms as in Gill (1980). In contrast, we focus on the interaction between long waves and far smaller convective structures (with horizontal scale $\sim$ 10km) corresponding to cumulus clouds. Here, axisymmetric ‘cloud-like’ circulations are found as solutions to the nonlinear, non-hydrostatic Boussinesq equations driven by steady, localised heating. Similar (larger-scale) axisymmetric flows in the atmosphere have been studied by Wirth (1998); Wirth and Dunkerton (2006); Plumb and Hou (1992) with implications for the development of monsoons and hurricanes, as well as large-scale meridional circulation. In our set-up, the localised heating is small-scale in all horizontal directions so that the circulation generated is qualitatively similar to a cumulus type cloud.

With the flow representing a convective cloud field established, the interaction between large-scale waves and small-scale clouds is investigated through the method of homogenisation. By linearising the Boussinesq equations about the cloud field variables, a spatial variable on the scale of the Rossby radius is introduced (large-scale compared to the cloud scale), and a multiple-scales analysis may be performed. The outcome of this analysis is a system of homogenised integro-differential equations, valid on the large-scale, which include terms that capture the leading-order interaction between the large-scale waves and small-scale cloud circulations. These new equations do not require the fine grid spacing used in numerical weather simulations in order to capture both small- and large-scale features of the atmosphere, and provide a non-heuristic parameterisation of convective processes.

This study draws a direct link to the previous chapter and the dynamics of the shallow water equations in the presence of topography. Firstly, it is well known that modal decompositions of the atmosphere, which is now a standard textbook topic (see e.g. Gill, 1982, §6.11; Olbers et al., 2012, Ch. 8) and which has origins dating back as far as Laplace (1776), allows the atmosphere to be represented as individual modes with horizontal structures governed by the shallow water equations. In an unforced atmosphere these modes are decoupled; however, as is seen in our analysis, the presence of a cloud field introduces extra terms into the modal decomposition which couples the wave modes to one another. Coupling of modes in this manner is seen in the literature in cases where the fluid is considered to propagate over topography (Craig, 1987; Smith and Young, 2002; Kelly et al., 2010; Kelly, 2016; Garrett and Kunze, 2007). Here, the interaction between a gently sloping seabed and surface waves in a stratified ocean excites internal waves within the fluid. The fact that the coupling between wave modes through convection is somewhat analogous to that caused by topographically induced tidal conversion strengthens the links between this section and the material discussed in chapter 3.

The manner in which wave modes in our problem are coupled is linked to another important body of work from the literature, namely the theory of *transilient matrices*. Originating in turbulence theory (Stull, 1984; Romps and Kuang, 2011), transilient matrices are used to model the non-local redistribution in the vertical of a tracer due to the rapid turbulent rearrangement of fluid parcels. These matrices have more recently been utilised in the theory of convective transport processes (see e.g. Cheng et al., 2017), where the rearrangement of fluid parcels from an initial height to a final height through convective adjustment is determined by a non-local integral operator. Likewise, in this paper, the effect of a small-scale convective cloud field on long wave propagation is seen to be a continuous-in-time, non-local, vertical rearrangement of horizontal momentum and buoyancy profiles. In the continuum limit, the transilient matrices become integral operators involving *transilient kernels* which quantify the non-local rearrangements. One of the main outcomes of this work is a method by which transilient kernels can be explicitly diagnosed for any given cloud field for use in NWP simulations - an area of research where the utility of transilient operators as a means of parameterising turbulence and convection is already being realised (see e.g. Forster et al., 2007; Kuell and Bott, 2022).

To allow for a straightforward presentation of the key concepts and main qualitative results, a number of simplifying assumptions are made. In particular, the clouds are assumed to be sufficiently well-separated so that the circulations due to each individual cloud, despite being strongly nonlinear in the cloud core region, interact only linearly where they overlap. For simplicity, the cloud circulations are driven by imposed steady heating fields, which represent the release of latent heat of condensation in cumulus cloud updrafts. Admittedly, the lack of time dependence in the cloud circulation is a weak assumption when considered alongside time-scales associated with long wave propagation. In reality, cumulus clouds evolve over the diurnal cycle due to local variations in the solar heat flux. There is also an implicit assumption here that effects due to a dynamically active moisture field will be of secondary importance. Despite this, a suitable choice of heating field can result in a plausible cloud circulation with a strong narrow updraft surrounded by a wide region of subsidence. These two assumptions should be viewed as the weakest points in our model from a physical standpoint; however, they do act as a good starting point upon which to build our asymptotic theory, and the development of models which relax these assumptions is left as a topic for future studies.

The structure of this chapter is as follows. In section 4.1 we derive the equations governing long wave propagation in the presence of clouds in an incompressible, stratified atmosphere using the method of homogenisation. A detailed review of wave dynamics in the absence of convection is given in section 4.2, with a particular emphasis on how the vertical structure of the atmosphere may be decomposed into barotropic and baroclinic modes. In section 4.3, the results are generalised to the case in which convective clouds are present. In particular, we show the method by which the background flow and the cell problems associated with homogenisation are solved. The modified, averaged equations are then derived with convection shown to enter the dynamics through terms involving integral operators which are non-local in the vertical. Finally, in section 4.4 the dispersive characteristics of waves in a mid-latitude β–channel are investigated with a view to gaining insight into how atmospheric waves are affected by the presence of a stationary convective cloud field.

4.1 Homogenisation of the Boussinesq Equations

We begin with the fully nonlinear, non-hydrostatic Boussinesq equations (2.72-2.75), which are given by

$$\frac{\partial \boldsymbol{v}}{\partial t} + f\boldsymbol{k} \times \boldsymbol{v} + (\boldsymbol{v} \cdot \nabla)\,\boldsymbol{v} = -\nabla p + b\boldsymbol{k} + \nabla \cdot (\nu \nabla \boldsymbol{v})\,, \tag{4.1}$$

$$\nabla \cdot \boldsymbol{v} = 0, \tag{4.2}$$

$$\frac{\partial b}{\partial t} + (\boldsymbol{v} \cdot \nabla)\, b + N^2 w = \dot{Q} + \nabla \cdot (\kappa \nabla b)\,. \tag{4.3}$$

The final terms in equations (4.1) and (4.3) parameterise the turbulent diffusion of momentum and buoyancy with eddy viscosity ν and diffusivity κ respectively. (These parameterisations are based on a Reynolds averaging procedure, for which the interested reader is referred to e.g. Bauer et al. (1999); Ting (2016); Pedlosky (1987) §4.2 for more detail). Throughout this chapter, the vector $\boldsymbol{v} = (u, v, w)^T$ is the full 3-dimensional velocity field, and $\nabla = (\partial_x, \partial_y, \partial_z)$ is the 3-dimensional gradient operator. For generality, we allow $N^2 = N^2(z)$ to vary with z and note that the variable Coriolis parameter $f = f_0 + \beta y$ means that the result may apply to both mid-latitude and equatorial regions depending on the value of f_0. In the present context, $\dot{Q}$ should be understood as a diabatic heat source parameterising latent heat release as moisture in the atmosphere condenses (see e.g. Ogura and Phillips, 1962; Ling and Zhang, 2013; Holton and Hakim, 2013, Ch. 11).

Since we will ultimately be concerned with long wave propagation in the presence of steady, cumulus convection, it is helpful to non-dimensionalise (4.1–4.3) on the scale of an individual convective cloud. Assuming that the height and horizontal extent of a cumulus circulation are of the same order, we take the tropopause height H_T as a typical length scale and N_0 as a typical scale for the buoyancy frequency. We then have $N_0 H_T$ as the velocity scale, $N_0^2 H_T^2$ as the perturbation pressure scale, and $N_0^2 H_T$ as the buoyancy scale. Correspondingly, the eddy viscosity ν and diffusivity κ are both scaled as $N_0 H_T^2$, and the heating is scaled as $N_0^3 H_T$. The time scale T associated with the temporal variable t and the Coriolis parameter f is taken to be that of the long waves, which is indeed much greater than the time scale N_0^{-1}.

Consequently, the equations may be written in non-dimensional form as

$$\varepsilon\left(\frac{\partial \boldsymbol{v}}{\partial t}+f\boldsymbol{k}\times\boldsymbol{v}\right)+\left(\boldsymbol{v}\cdot\nabla\right)\boldsymbol{v}=-\nabla p+b\boldsymbol{k}+\nabla\cdot\left(\nu\nabla\boldsymbol{v}\right), \tag{4.4}$$

$$\nabla\cdot\boldsymbol{v}=0, \tag{4.5}$$

$$\varepsilon\frac{\partial b}{\partial t}+\left(\boldsymbol{v}\cdot\nabla\right)b+N^2w=\dot{Q}+\nabla\cdot\left(\kappa\nabla b\right), \tag{4.6}$$

where variable names are retained for the non-dimensional quantities, and where $\varepsilon = 1/N_0T$. In the case where waves are considered in mid-latitudes, we may take $T = f_0^{-1}$ as an appropriate time scale. In this case, the non-dimensional Coriolis parameter becomes $f = 1 + \varepsilon\bar{\beta}Y$ where $\bar{\beta} = \beta L_R/f_0$ is the rescaled beta parameter, with $L_R = N_0H_T/f_0$ being the Rossby radius of deformation appropriate to the mid-latitude atmosphere. Using typical values of the buoyancy frequency and Coriolis parameter for the mid-latitude troposphere ($N_0 = 10^{-2}\mathrm{s}^{-1}$, $f_0 = 10^{-4}\mathrm{s}^{-1}$) results in a value of $\varepsilon \approx 0.01$. Note that here, and throughout, we use capital letters $\boldsymbol{X} = (X, Y, 0)^T$ to denote the horizontal spatial coordinates on the small-scales, reserving the lower case notation $\boldsymbol{x} = (x, y, 0)^T$ for the large-scales to be introduced later on.

We are interested in the propagation of long waves in (4.4–4.6) through a steady background flow $\left\{\overline{\boldsymbol{v}}, \overline{p}, \overline{b}\right\}$. This steady flow is defined as the leading-order solution to (4.4–4.6) in the presence of a specified heating $\dot{Q}$ which determines the cloud field. We are also interested in arrays of weakly-interacting clouds - that is, clouds which are spaced at a great enough distance that the interaction of their downwelling regions have a negligible effect on the dynamics. Under such assumptions, the heating may be expressed as a linear combination of the contributions from each individual cloud centered at $(X^{(i)}, Y^{(i)})$ as

$$\dot{Q}=\sum_{i=1}^{\infty}\dot{Q}_0(r^{(i)},z), \tag{4.7}$$

where $r^{(i)} \equiv |\boldsymbol{X}-\boldsymbol{X}^{(i)}| = \sqrt{(X-X^{(i)})^2+(Y-Y^{(i)})^2}$. In the above decomposition and from hereon, variables subscripted with a 0 indicate the contribution from a single cloud centred at the origin. We are then able to assume that the response to the heating may be expressed similarly, as

$$\overline{\boldsymbol{v}} = \sum_{i=1}^{\infty} \overline{\boldsymbol{v}}_0(r^{(i)}, z), \quad \overline{p} = \sum_{i=1}^{\infty} \overline{p}_0(r^{(i)}, z), \quad \overline{b} = \sum_{i=1}^{\infty} \overline{b}_0(r^{(i)}, z). \tag{4.8}$$

Finally, in order to ensure that the effects of turbulence are confined to regions in and around the clouds, both ν and κ are allowed to vary with distance from the cloud core, and are assumed to have similar decompositions, so that

$$\nu = \sum_{i=1}^{\infty} \nu_0(r^{(i)}), \quad \kappa = \sum_{i=1}^{\infty} \kappa_0(r^{(i)}). \tag{4.9}$$

This is a reasonable assumption from a physical standpoint, since the effects of turbulence are minimal outside of the atmospheric boundary layer, except for in regions of high convective activity (Holtslag, 2003). The background flow is therefore found from the 'cloud circulation problem' (CCP hereafter), given by

$$\left(\overline{\boldsymbol{v}}_0 \cdot \nabla\right) \overline{\boldsymbol{v}}_0 = -\nabla \overline{p}_0 + \overline{b}_0 \boldsymbol{k} + \nabla \cdot \left(\nu_0 \nabla \overline{\boldsymbol{v}}_0\right), \tag{4.10}$$

$$\nabla \cdot \overline{\boldsymbol{v}}_0 = 0, \tag{4.11}$$

$$\left(\overline{\boldsymbol{v}}_0 \cdot \nabla\right) \overline{b}_0 + N^2 \overline{w}_0 = \dot{Q}_0 + \nabla \cdot \left(\kappa_0 \nabla \overline{b}_0\right), \tag{4.12}$$

where the single source $\dot{Q}_0 = \dot{Q}_0(r, z)$ is centred on the origin. Consequently the solutions to the CCP (4.10–4.12) are axisymmetric functions, i.e. $\left\{\overline{\boldsymbol{v}}_0, \overline{p}_0, \overline{b}_0\right\} = \left\{\overline{\boldsymbol{v}}_0(r, z), \overline{p}_0(r, z), \overline{b}_0(r, z)\right\}$.

We are interested in linear waves with horizontal wavelengths at the order of the Rossby radius L_R propagating on the background flow. Therefore, in order to examine interactions across spatial scales, we introduce the large, horizontal spatial variable $\boldsymbol{x} = \varepsilon \boldsymbol{X}$, with $\boldsymbol{x} = (x, y, 0)^T$ and expand the gradient operator according to the multiple-scales formalism as

$$\nabla \to \varepsilon \nabla_{\boldsymbol{x}} + \nabla, \tag{4.13}$$

where $\nabla_{\boldsymbol{x}} = (\partial_x, \partial_y, 0)^T$. In conjunction with this, we introduce a horizontal averaging operator over the small scales $\langle \cdot \rangle$ as is typical in the method of homogenisation. For a function $g(\boldsymbol{X})$ which may be decomposed as in (4.7), this operator acts as

$$\begin{aligned} \langle g \rangle &= \frac{1}{|\Omega|} \int_\Omega g(\boldsymbol{X}) \, \mathrm{d}\boldsymbol{X} \\ &= \frac{1}{|\Omega|} \int_\Omega \sum_{i=1}^{\infty} g_0 \left(|\boldsymbol{X} - \boldsymbol{X}^{(i)}|, \theta \right) \, \mathrm{d}\boldsymbol{X} \\ &= \overline{n} \langle g_0 \rangle_0, \end{aligned} \tag{4.14}$$

where

$$\langle g_0 \rangle_0 = \int_0^\infty \int_0^{2\pi} g_0(r, \theta) r \, \mathrm{d}\theta \mathrm{d}r, \tag{4.15}$$

and $\overline{n}$ is the number density of clouds per unit area in Ω. Throughout this chapter we will focus on the situation where the number density is of order ε, in which case we may write $\overline{n} = \varepsilon n$ where n is of order unity. Inserting (4.13) into (4.4–4.6) and linearising about the background flow using

$$\boldsymbol{v} \to \overline{\boldsymbol{v}} + \delta \boldsymbol{v}, \quad p \to \overline{p} + \delta p, \quad b \to \overline{b} + \delta b,$$

where $\delta \ll \varepsilon \ll 1$ and un-barred variables now correspond to perturbations about the background flow, gives

$$\begin{aligned} \varepsilon \left(\frac{\partial \boldsymbol{v}}{\partial t} + f\boldsymbol{k} \times \boldsymbol{v} + (\overline{\boldsymbol{v}} \cdot \nabla_{\boldsymbol{x}}) \boldsymbol{v} \right) + (\overline{\boldsymbol{v}} \cdot \nabla) \boldsymbol{v} + (\boldsymbol{v} \cdot \nabla) \overline{\boldsymbol{v}} &= -\varepsilon \nabla_{\boldsymbol{x}} p - \nabla p + b\boldsymbol{k} \\ +\varepsilon^2 \nu \nabla_{\boldsymbol{x}}^2 \boldsymbol{v} + \varepsilon \nu \nabla_{\boldsymbol{x}} \cdot \nabla \boldsymbol{v} + \varepsilon \nabla \cdot (\nu \nabla_{\boldsymbol{x}} \boldsymbol{v}) &+ \nabla \cdot (\nu \nabla \boldsymbol{v}), \end{aligned} \tag{4.16}$$

$$\varepsilon \nabla_{\boldsymbol{x}} \cdot \boldsymbol{v} + \nabla \cdot \boldsymbol{v} = 0, \tag{4.17}$$

$$\begin{aligned} \varepsilon \left(\frac{\partial b}{\partial t} + (\overline{\boldsymbol{v}} \cdot \nabla_{\boldsymbol{x}}) b \right) + (\overline{\boldsymbol{v}} \cdot \nabla) b + (\boldsymbol{v} \cdot \nabla) \overline{b} + N^2 w &= \\ \varepsilon^2 \kappa \nabla_{\boldsymbol{x}}^2 b + \varepsilon \kappa \nabla_{\boldsymbol{x}} \cdot \nabla b + \varepsilon \nabla \cdot (\kappa \nabla_{\boldsymbol{x}} b) &+ \nabla \cdot (\kappa \nabla b). \end{aligned} \tag{4.18}$$

We decompose the time dependent, un-barred variables in (4.16–4.18) into their averaged parts (denoted by capitals) and fluctuations (denoted with tildes) as

$$\boldsymbol{v} = \boldsymbol{U}(\boldsymbol{x}, z, t) + \varepsilon W(\boldsymbol{x}, z, t)\boldsymbol{k} + \tilde{\boldsymbol{v}}(\boldsymbol{x}, \boldsymbol{X}, z, t), \tag{4.19}$$

$$p = P(\boldsymbol{x}, z, t) + \tilde{p}(\boldsymbol{x}, \boldsymbol{X}, z, t), \tag{4.20}$$

$$b = B(\boldsymbol{x}, z, t) + \tilde{b}(\boldsymbol{x}, \boldsymbol{X}, z, t). \tag{4.21}$$

Note here, that the hydrostatic approximation has been made implicitly at this step, as the averaged vertical velocity appears only at order ε. Correspondingly, $\boldsymbol{U} = (U, V, 0)^T$ constitutes only the averaged horizontal velocity. The fluctuating components in the above expansions must all have zero horizontal average, i.e. $\langle \tilde{\boldsymbol{v}} \rangle = 0$ and $\langle \tilde{p} \rangle = \langle \tilde{b} \rangle = 0$.

Inserting (4.19–4.21) into equations (4.16–4.18) and applying the averaging operator, we find at order ε

$$\begin{aligned} \frac{\partial \boldsymbol{U}}{\partial t} + f\boldsymbol{k} \times \boldsymbol{U} + n\partial_z \left\langle \overline{w}_0 \tilde{\boldsymbol{u}}_0 + \tilde{w}_0 \overline{\boldsymbol{u}}_0 \right\rangle_0 &= -\nabla_{\boldsymbol{x}} P \\ &\quad + \left\{ n\langle \nu_0 \rangle_0 \partial^2_{zz} \boldsymbol{U} + n\partial_z \langle \nu_0 \nabla \tilde{\boldsymbol{u}}_0 \rangle_0 \right\}, \end{aligned} \tag{4.22}$$

$$\frac{\partial P}{\partial z} = B, \tag{4.23}$$

$$\nabla_{\boldsymbol{x}} \cdot \boldsymbol{U} + \frac{\partial W}{\partial z} = 0, \tag{4.24}$$

$$\frac{\partial B}{\partial t} + n\partial_z \left\langle \overline{w}_0 \tilde{b}_0 + \tilde{w}_0 \overline{b}_0 \right\rangle_0 + N^2 W = \left\{ n\langle \kappa_0 \rangle_0 \partial^2_{zz} B + n\partial_z \langle \kappa_0 \nabla \tilde{b}_0 \rangle_0 \right\}. \tag{4.25}$$

The quantities surrounded by curly brackets are the terms introduced through the presence of turbulence in the system. For our purposes, these are of little interest, and we take $\nu_0, \kappa_0 \ll 1$ everywhere, since turbulence is assumed to play an insignificant role at leading order. Therefore, in future calculations, the terms in curly brackets are omitted. The quantities denoted with a tilde are found from the terms in (4.16–4.18) at order $O(1)$, which are

$$\begin{aligned}
\left(\overline{\boldsymbol{v}}_0 \cdot \nabla\right)\tilde{\boldsymbol{v}}_0 + \left(\tilde{\boldsymbol{v}}_0 \cdot \nabla\right)\overline{\boldsymbol{v}}_0 + \nabla\tilde{p}_0 - \tilde{b}_0\boldsymbol{k} - \nabla\cdot\left(\nu_0\nabla\tilde{\boldsymbol{v}}_0\right) &= \qquad (4.26)\\
-\left(\boldsymbol{U}\cdot\nabla\right)\overline{\boldsymbol{v}}_0 - \overline{w}_0\partial_z\boldsymbol{U} + \left\{\nu_0\partial_{zz}^2\boldsymbol{U}\right\}&,\\
\nabla\cdot\tilde{\boldsymbol{v}}_0 = 0&, \qquad (4.27)\\
\left(\overline{\boldsymbol{v}}_0 \cdot \nabla\right)\tilde{b}_0 + \left(\tilde{\boldsymbol{v}}_0 \cdot \nabla\right)\overline{b}_0 + N^2\tilde{w}_0 - \nabla\cdot\left(\kappa_0\nabla\tilde{b}_0\right) &= \qquad (4.28)\\
-\left(\boldsymbol{U}\cdot\nabla\right)\overline{b}_0 - \overline{w}_0\partial_z B + \left\{\kappa_0\partial_{zz}^2 B\right\}&.
\end{aligned}$$

Equations (4.26–4.28), termed the 'cell problem equations' (CPE hereafter), are a linear, elliptic system of partial differential equations which may be inverted to find $\tilde{\boldsymbol{v}}_0$, $\tilde{p}_0$ and $\tilde{b}_0$ in terms of the averaged quantities $\boldsymbol{U}$ and B. The terms on the right-hand side should be viewed as source terms driving the response of the fluid to the imposed background flow. The terms on the left hand side involving ν_0 and κ_0 have an important regularising effect on the system, and must be retained in order to invert them numerically. On the other hand, the source terms involving turbulent dissipation are of little importance, since $\nu_0, \kappa_0 \ll 1$. Therefore, in future calculations the terms in curly brackets will be omitted.

Equations (4.22–4.25) are none other than the linearised, hydrostatic Boussinesq equations with additional correlation terms involving the background flow and the time-dependent response. These terms are seen to be the divergences of the vertical momentum and buoyancy fluxes due to the presence of the clouds. In the absence of clouds, these terms disappear and we are left with a closed system in $\boldsymbol{U}, W, P$ and B. Before considering the effect of a cloud field on the propagation of waves, it is first helpful to review the problem when $n = 0$, as it provides significant insight into how more complex dynamics may be understood.

4.2 Vertical mode decomposition for $n = 0$

Decomposition of the atmosphere into vertical modes is now a standard method found in mathematical literature. Its origins date back as far as Laplace (1776), and later was a key idea utilised in the Matsuno-Gill model (Matsuno, 1966; Gill, 1980) as a means to study the heat-induced circulation of the atmosphere. Consequently, much of the mathematics covered in this section may be found in textbooks such as Gill (1982), §6.11 and Olbers et al. (2012), Ch. 8. It is however worth revisiting this topic in detail, since many of the ideas will be generalised for our purposes in later sections.

Before returning to the problem involving the response of the large-scale atmosphere to small-scale clouds, it is first helpful to analyse the problem in the absence of heating. Importantly, by first considering the situation in which the boundary between the troposphere and stratosphere is a free surface, we are able to decompose the averaged variables into vertical modes with horizontal structures obeying equations analogous to those obeyed by a vertically homogeneous fluid. These modes may be classified into a *barotropic* and and a countably infinite set of *baroclinic* modes. The free surface view of the tropopause naturally introduces a number of complex, physical phenomena which are beyond the scope of this work, however the results are readily adapted to the rigid lid view of the tropopause. Indeed, retaining the free surface dynamics only when considering the barotropic mode allows us to establish a relatively complete picture of long atmospheric waves, whilst introducing only minimal errors (Kelly et al., 2010).

4.2.1 Free surface dynamics

Consider the averaged equations (4.22–4.25) in the absence of a cloud field, so that $n = 0$. This yields the linearised system

$$\frac{\partial \boldsymbol{U}}{\partial t} + f\boldsymbol{k} \times \boldsymbol{U} = -\nabla P, \tag{4.29}$$

$$\frac{\partial P}{\partial z} = B, \tag{4.30}$$

$$\nabla \cdot \boldsymbol{U} + \frac{\partial W}{\partial z} = 0, \tag{4.31}$$

$$\frac{\partial B}{\partial t} + W = 0, \tag{4.32}$$

in non-dimensional form, where we have also taken $N^2(z) = 1$ for simplicity (the case of a varying N^2 is dealt with in Appendix F). The domain in this problem is taken to be infinite in the horizontal directions, with the vertical spatial variable $z \in [0, 1]$ so that the non-dimensional depth of the fluid is 1. That is, the boundary between the (flat) ground and the troposphere is at $z = 0$ and the boundary between the troposphere and stratosphere (the tropopause) is at $z = 1$. These equations are equipped with the boundary conditions

$$W = 0, \quad \text{at} \quad z = 0, \tag{4.33}$$

$$W = \frac{\partial \eta}{\partial t}, \quad \text{at} \quad z = 1, \tag{4.34}$$

corresponding to no normal flow at the ground, and a free surface condition at $z = 1$ where $\eta(\boldsymbol{x}, t) = \alpha P(\boldsymbol{x}, 1, t)$ is the non-dimensional free surface displacement above the resting tropopause, and $\alpha = N_0^2 H_T / g$ (see Olbers et al., 2012, §5.2.4). Taking values of $N_0 \approx 0.01\mathrm{s}^{-1}$, $H_T \approx 10^4\mathrm{m}$ and $g \approx 10\mathrm{ms}^{-2}$, appropriate to the atmosphere gives $\alpha \approx 0.1$, which may be considered a small parameter. It is important to emphasise that the free surface boundary condition is not entirely physical, but rather a crude model which assumes that the jump in stratification between the troposphere and stratosphere causes the tropopause to behave in a manner analogous to the free surface of the ocean, for example.

It is shown in Appendix F that the solutions to (4.29–4.32) may be written as

$$[\boldsymbol{U}(\boldsymbol{x}, z, t), P(\boldsymbol{x}, z, t)] = \sum_{n=0}^{\infty} \left[\tilde{\boldsymbol{U}}_n(\boldsymbol{x}, t), \tilde{P}_n(\boldsymbol{x}, t)\right] \phi_n(z), \tag{4.35}$$

$$[W(\boldsymbol{x}, z, t), B(\boldsymbol{x}, z, t)] = \sum_{n=0}^{\infty} \left[\tilde{W}_n(\boldsymbol{x}, t), \tilde{B}_n(\boldsymbol{x}, t)\right] \Phi_n(z), \tag{4.36}$$

where $\phi_n(z)$ and $\Phi_n(z)$ obey

$$\frac{d\Phi_n}{dz} = \phi_n, \tag{4.37}$$

as well as the Sturm-Liouville problems

$$\frac{d^2\phi_n}{dz^2} + \frac{1}{c_n^2}\phi_n = 0, \tag{4.38}$$

$$\frac{d\phi_n}{dz} = 0, \quad \text{on} \quad z = 0 \tag{4.39}$$

$$\frac{d\phi_n}{dz} + \alpha\phi_n = 0, \quad \text{on} \quad z = 1, \tag{4.40}$$

and

$$\frac{d^2\Phi_n}{dz^2} + \frac{1}{c_n^2}\Phi_n = 0, \tag{4.41}$$

$$\Phi_n = 0, \quad \text{on} \quad z = 0 \tag{4.42}$$

$$\alpha\frac{d\Phi_n}{dz} = \frac{1}{c_n^2}\Phi_n, \quad \text{on} \quad z = 1. \tag{4.43}$$

The leading order solutions to this problem are therefore found by setting $\alpha = 0$, giving

$$\phi_n(z) = \sqrt{2}\cos(n\pi z), \quad \Phi_n(z) = \frac{\sqrt{2}}{n\pi}\sin(n\pi z), \quad c_n = \frac{1}{n\pi}, \tag{4.44}$$

for $n = 1, 2, 3, ...$, where we have identified these solutions with the positive values of n. Here, the factors of $\sqrt{2}$ arise from imposing the orthogonality condition

$$\int_0^1 \phi_m(z)\phi_n(z)\,\mathrm{d}z = \delta_{mn}, \tag{4.45}$$

where δ_{mn} is the Kronecker delta function.

These wave modes are known as *baroclinic modes*, since the eigenvalues c_n^{-2} quantify the vertical density variations within the fluid confined between two unmoving boundaries. They do not constitute a complete picture of atmospheric dynamics, however. Indeed, it is readily seen that at leading order there is a trivial solution of (4.38–4.40) satisfying (4.45) given by

$$\phi_0(z) = 1, \quad \frac{1}{c_n} = 0. \tag{4.46}$$

Whilst the approximate value of $\phi_0 = 1$ is sufficient for our purposes, the approximation of the eigenvalue implies that c_0 is infinite. Therefore, a higher order approximation must be made. This is achieved after multiplying (4.38) by ϕ_n, and integrating by parts to find an approximation for the eigenvalues which is correct up to order α^2. Thus, we have

$$c_n^2 = \frac{\int_0^1 \phi_n^2 \, \mathrm{d}z}{\alpha\phi_n(1)^2 + \int_0^1 \left(\frac{d\phi_n}{dz}\right)^2 \, \mathrm{d}z}, \tag{4.47}$$

which after inserting the value of $\phi_0 = 1$ yields $c_0 = 1/\sqrt{\alpha}$. This wave mode is known as the *barotropic mode* since the eigenvalue in this case quantifies the vertical free surface displacement rather than the internal variations in stratification.

The analogue of condition (4.45) for the Φ_n functions is slightly more complicated, and is found as in Kelly (2016) by multiplying (4.41) by Φ_m and integrating. Thus we have

$$\begin{aligned} 0 &= \int_0^1 \Phi_m \frac{d^2\Phi_n}{dz^2} + \frac{1}{c_n^2}\Phi_m\Phi_n \, \mathrm{d}z && (4.48) \\ &= \int_0^1 \frac{d}{dz}\left(\Phi_m \frac{d\Phi_n}{dz}\right) - \frac{d\Phi_m}{dz}\frac{d\Phi_n}{dz} + \frac{1}{c_n^2}\Phi_m\Phi_n \, \mathrm{d}z && (4.49) \\ &= \frac{1}{\alpha c_n^2}\Phi_m(1)\Phi_n(1) - \int_0^1 \phi_m\phi_n \, \mathrm{d}z + \frac{1}{c_n^2}\int_0^1 \Phi_m\Phi_n \, \mathrm{d}z, && (4.50) \end{aligned}$$

where in the last line we have used (4.37) and the boundary condition (4.43). Using (4.45), we may write the condition for Φ_n as

$$\int_0^1 \Phi_m(z)\Phi_n(z) \, \mathrm{d}z = c_m c_n \delta_{mn} - \frac{1}{\alpha}\Phi_m(1)\Phi_n(1), \tag{4.51}$$

where we note that interchanging c_m and c_n has no effect on the result. This is of course not an orthogonality condition, but rather an integral property of the basis functions. Collectively, we will refer to (4.45) and (4.51) as *integral properties* of the basis functions, even though the first is in fact a true orthogonality condition.

Finally, we recall (as is shown in Appendix F) that the horizontal structure of each mode in the decomposition obeys the shallow water equations

$$\frac{\partial \tilde{\boldsymbol{U}}_n}{\partial t} + f\boldsymbol{k} \times \tilde{\boldsymbol{U}}_n = -\nabla \tilde{P}_n, \tag{4.52}$$

$$\frac{\partial \tilde{P}_n}{\partial t} + c_n^2 \nabla \cdot \tilde{\boldsymbol{U}}_n = 0. \tag{4.53}$$

4.2.2 Rigid lid dynamics

In the previous section we dealt with an atmosphere obeying a free surface boundary condition at $z = 1$. We now consider the case where the free surface is replaced with a rigid lid condition - that is, $W = 0$ at $z = 1$. Under this assumption, the boundary conditions (4.40) and (4.43) are replaced with $d\phi_n/dz = 0$ and $\Phi_n = 0$ at $z = 1$ respectively. In the free surface approximation, the baroclinic modes were found at $O(1)$ in the $\alpha \ll 1$ regime to a good accuracy, and so they remain unchanged at leading order under the rigid lid boundary conditions. Consequently, the leading order approximations to the wave speed $c_n = 1/n\pi$ and the relation $\phi_n = d\Phi_n/dz$ still applies for $n = 1, 2, 3....$

The barotropic mode, (the eigenvalue of which is found at order α under the free surface approximation) cannot be captured using rigid lid boundary conditions, since now $1/c_0 = 0$ is an exact eigenvalue. Similarly, $\phi_0 = d\Phi_0/dz$ must not apply, since Φ_0 would not be able to satisfy the boundary conditions if it were a linear function of z. Therefore, under the rigid lid approximation, it is conventional to replace c_0 with the free surface analogue $c_0 = 1/\sqrt{\alpha}$ and to take $\Phi_0 = 0$, satisfying the boundary conditions, a posteriori. This approach is an approximation correct at leading order in α for all modes. The integral properties in this case become

$$\int_0^1 \phi_m(z)\phi_n(z)\ \mathrm{d}z = \delta_{mn}, \tag{4.54}$$

$$\int_0^1 \Phi_m(z)\Phi_n(z)\ \mathrm{d}z = c_m c_n \delta_{mn}, \tag{4.55}$$

where the latter condition only applies when m and n are not both zero. In practice, when applying the convention of using the post hoc barotropic wave speed, we perform all calculations using the free surface integral property for Φ_n (4.51), and use the rigid lid approximations for the basis functions afterwards, omitting the boundary terms in (4.51). This allows us to retain an approximation for the barotropic mode with a finite wave speed, with only small errors introduced (Kelly et al., 2010; Kelly, 2016). We re-emphasise that this is not equivalent to applying (4.55) at every step, since the $m = n = 0$ case cannot be dealt with properly. In the following sections, we will be concerned with the rigid lid boundary conditions and so will use this convention.

4.3 The effect of clouds on the large-scale dynamics

Our analysis so far has shown that in the absence of a cloud field, the equations governing long waves in a stratified atmosphere may be decomposed into vertical modes, with a horizontal structure obeying a system of shallow water equations with a mode-dependent equivalent wave speed. In this section, the analysis is generalised to understand how these waves are modified in the presence of a cloud field. To achieve this, the correlation terms in (4.22–4.25) must be fully determined in order to close the system of averaged equations in terms of the large-scale variables at leading order. This involves solving two additional systems of equations, namely the CCP (4.10–4.12) in the presence of a specified diabatic heating profile, and the CPE (4.26–4.28) determining the time-dependent response.

In the present set-up, the CCP and CPE are defined on a domain which extends to $+\infty$ in the radial direction. Consequently, appropriate decay conditions must be imposed on their solutions as $r \to \infty$. A key step common to the numerical implementation of both the CCP and CPE which follows, is to truncate the domain in the radial direction at a value $r = r_{\text{out}}$ and replace the decay conditions with appropriate boundary conditions on $r = r_{\text{out}}$. Since the solutions to the CCP and CPE are assumed to decay away from the origin, r_{out} should be chosen so that they do not depend sensitively on its value - that is, the solutions do not change significantly as r_{out} is increased.

Following the domain truncation, a further simplifying assumption may be made about the eddy diffusion coefficients. That is, the radial dependence of ν_0 and

κ_0 are assumed to be piecewise constant, taking a finite value in the region $r \leq r_{\text{out}}$, and 0 in $r > r_{\text{out}}$. This allows us to take ν_0 and κ_0 as constants in the solutions to the CCP and CPE which follow, whilst maintaining the physical requirement that the effects of turbulent diffusion are localised around individual clouds. The values of $\nu_0 = \kappa_0 = 0.05$ are used for the rest of the chapter.

4.3.1 Solution of the CCP

Consider equations (4.10–4.12) where $\dot{Q}_0(r, z)$ is a known, axisymmetric function. Under this assumption, and the lack of rotation in the CCP, it follows that the components of the velocity vector are independent of the azimuthal coordinate θ, and that the azimuthal component of velocity is identically zero. The background flow may therefore be expressed as

$$\overline{\boldsymbol{v}}_0 = \overline{u}_0^r(r, z)\boldsymbol{e}_r + \overline{w}_0(r, z)\boldsymbol{k}, \tag{4.56}$$

where $\overline{u}_0^r$ is the radial component of velocity, and $\boldsymbol{e}_r$ and $\boldsymbol{k}$ are the cylindrical polar coordinate basis vectors in the radial and vertical directions respectively. Since the flow is incompressible, it can be described completely in terms of a streamfunction $\overline{\psi}_0$ satisfying

$$\overline{u}_0^r = -\frac{1}{r}\frac{\partial \overline{\psi}_0}{\partial z}, \quad \overline{w}_0 = \frac{1}{r}\frac{\partial \overline{\psi}_0}{\partial r}, \tag{4.57}$$

so that the continuity equation (4.11) is automatically satisfied. Note that we retain the overline and subscript 0 notation here for clarity when referring to solutions of the CCP. Introducing the azimuthal component of vorticity $\overline{\zeta}_0$ which is defined as

$$\overline{\zeta}_0 = \frac{\partial \overline{w}_0}{\partial r} - \frac{\partial \overline{u}_0^r}{\partial z}, \tag{4.58}$$

the governing equations may be expressed in streamfunction-vorticity form as

$$\mathcal{J}\left(\overline{\psi}_0, \overline{\zeta}_0/r\right) - \frac{\partial \overline{b}_0}{\partial r} = \nu_0 \left(\nabla^2 \overline{\zeta}_0 - \frac{\overline{\zeta}_0}{r^2}\right), \tag{4.59}$$

$$\overline{\zeta}_0 = \frac{1}{r}\left(\frac{\partial^2 \overline{\psi}_0}{\partial r^2} - \frac{1}{r}\frac{\partial \overline{\psi}_0}{\partial r} + \frac{\partial^2 \overline{\psi}_0}{\partial z^2}\right), \tag{4.60}$$

$$\frac{1}{r}\mathcal{J}\left(\overline{\psi}_0, \overline{b}_0\right) + \frac{N^2}{r}\frac{\partial \overline{\psi}_0}{\partial r} = \dot{Q}_0 + \kappa_0 \nabla^2 \overline{b}_0. \tag{4.61}$$

Here, $\mathcal{J}$ is the Jacobian operator, which acts on functions $c(r,z), d(r,z)$, as $\mathcal{J}(c,d) = \partial_r c \partial_z d - \partial_z c \partial_r d$. The above problem is a nonlinear system of equations in the three variables $\overline{\psi}_0, \overline{\zeta}_0, \overline{b}_0$ which must be solved in the domain $(r,z) \in (0, r_{\text{out}}) \times (0,1)$ subject to appropriate boundary conditions on $r = 0, r_{\text{out}}$ and $z = 0, 1$.

In the presence of a rigid lid at $z = 1$, the boundary conditions for a closed circulation are

$$\overline{\psi}_0 = \overline{\zeta}_0 = \overline{b}_0 = 0, \quad \text{on} \quad z = 0, 1, \tag{4.62}$$

$$\overline{\psi}_0 = \overline{\zeta}_0 = \partial_r \overline{b}_0 = 0, \quad \text{on} \quad r = 0, \tag{4.63}$$

$$\overline{\psi}_0 = \overline{\zeta}_0 = \overline{b}_0 = 0, \quad \text{on} \quad r = r_{\text{out}}. \tag{4.64}$$

It is also helpful (though not strictly necessary) to impose the condition

$$\int_0^1 \int_0^{r_{\text{out}}} \dot{Q}_0 \; r \mathrm{d}r \mathrm{d}z = 0, \tag{4.65}$$

so that there is no source or sink of buoyancy in the system. This is not a strict condition in order to make the system solvable, however in the limit that turbulent diffusion becomes negligible it is needed to ensure that a steady state solution exists. We retain it so that the turbulent terms in the system act primarily to ensure the system is well posed, and not in order to disperse excess buoyancy. This may also be enforced through requiring that $\langle \dot{Q}_0 \rangle_0 = 0$, which can be imposed through our choice of $\dot{Q}_0$ with little difficulty. The following section covers the numerical solution of equations (4.59–4.61) subject to the boundary conditions (4.62–4.64).

4.3.1.1 Numerical solutions to the CCP

The nonlinear system (4.59–4.61) is solved using an iterative procedure based on the quasi-linearisation method (see e.g. Motsa et al., 2014; Muzara et al., 2018). We begin by assuming there exist sequences of approximants for $\overline{\psi}_0, \overline{\zeta}_0, \overline{b}_0$, with the mth iterates denoted by $\overline{\psi}_0^{(m)}, \overline{\zeta}_0^{(m)}, \overline{b}_0^{(m)}$, such that

$$\left\{\overline{\psi}_0^{(m)}, \overline{\zeta}_0^{(m)}, \overline{b}_0^{(m)}\right\} \rightarrow \left\{\overline{\psi}_0, \overline{\zeta}_0, \overline{b}_0\right\} \qquad \text{as} \qquad m \rightarrow \infty. \tag{4.66}$$

The method is based on approximating the nonlinear terms at the $(m+1)$th iteration in the CCP as

$$\mathcal{J}\left(c^{(m+1)}, d^{(m+1)}\right) \approx \mathcal{J}\left(c^{(m+1)}, d^{(m)}\right) + \mathcal{J}\left(c^{(m)}, d^{(m+1)}\right) - \mathcal{J}\left(c^{(m)}, d^{(m)}\right), \tag{4.67}$$

where for generality, we have used arbitrary sequences $c^{(m)}, d^{(m)}$. Therefore, the $(m+1)$th iteration is found in terms of the mth iterate (which is assumed known) from the solution to the linear system

$$\begin{aligned}
\mathcal{J}\left(\overline{\psi}_0^{(m+1)}, \overline{\zeta}_0^{(m)}/r\right) + \mathcal{J}\left(\overline{\psi}_0^{(m)}, \overline{\zeta}_0^{(m+1)}/r\right) - \frac{\partial \overline{b}_0^{(m+1)}}{\partial r}& \qquad (4.68)\\
= \nu_0\left(\nabla^2\overline{\zeta}_0^{(m+1)} - \frac{\overline{\zeta}_0^{(m+1)}}{r^2}\right) - \mathcal{J}\left(\overline{\psi}_0^{(m)}, \overline{\zeta}_0^{(m)}/r\right)&,\\
\overline{\zeta}_0^{(m+1)} = \frac{1}{r}\left(\frac{\partial^2\overline{\psi}_0^{(m+1)}}{\partial r^2} - \frac{1}{r}\frac{\partial\overline{\psi}_0^{(m+1)}}{\partial r} + \frac{\partial^2\overline{\psi}_0^{(m+1)}}{\partial z^2}\right)&, \qquad (4.69)\\
\frac{1}{r}\mathcal{J}\left(\overline{\psi}_0^{(m+1)}, \overline{b}_0^{(m)}\right) + \frac{1}{r}\mathcal{J}\left(\overline{\psi}_0^{(m)}, \overline{b}_0^{(m+1)}\right) + \frac{N^2}{r}\frac{\partial\psi_0^{(m+1)}}{\partial r}& \qquad (4.70)\\
= \dot{Q}_0 + \kappa_0\nabla^2\overline{b}_0^{(m+1)} - \frac{1}{r}\mathcal{J}\left(\overline{\psi}_0^{(m)}, \overline{b}_0^{(m)}\right)&.
\end{aligned}$$

Note that this system of equations is linear in the unknown $(m+1)$th iterates, since at each step the mth iterates are known quantities. The 0th iterate is taken to be the solution to the original linear system (i.e. the solution to (4.59–4.61) in the absence of the nonlinear terms). This linear solution is most easily found numerically using the following spectral discretisation method; however, it is also possible to solve it

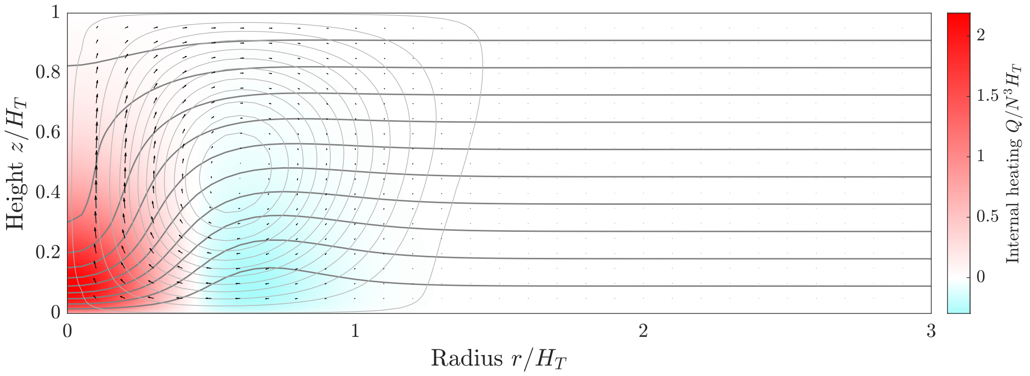

Figure 4.1: Numerical solutions to (4.59–4.61) for the specified heat distribution given in (4.71) and $\nu_0 = \kappa_0 = 0.05$. The streamlines of $\overline{\psi}_0$ are shown as closed, grey curves, and the contours of the total buoyancy $b_{\text{tot}} = \overline{b}_0 + z$ are shown as black curves. The heat distribution is shown using colour, with red and blue representing regions of heating and cooling respectively. Arrows are included showing the direction of cloud circulation.

analytically using integral transforms.

With the problem now specified on a finite domain $(r, z) \in [0, r_{\text{out}}] \times [0, 1]$, equations (4.68–4.70) are discretised using a Chebyshev collocation method, using $N_r = 31$ points in the radial, and $N_z = 81$ points in the vertical directions. The boundary conditions (4.62–4.64) are implemented in this formulation by altering the outer rows and columns in each block of the resulting block matrix (details omitted), and it is found that using $r_{\text{out}} = 5$ is sufficient to approximate the decay conditions. Discussions about the numerical convergence of the Chebyshev collocation method are postponed until section 4.3.3.3.

Figure 4.1 shows the solutions to the numerical procedure solving (4.59–4.61) for the heat distribution given by

$$\dot{Q}_0(r, z) = 12\mathrm{e}^{-5(r^2+z)}(1 - 5r^2)\sqrt{z(1 - z)}. \tag{4.71}$$

As previously stated, the numerical parameters used are $N_r = 31, N_z = 81$ and $r_{\text{out}} = 5$, with machine precision achieved after 5 iterations. The solutions appear to capture the basic features of the circulation surrounding a convecting cumulus cloud - that is, the circulation occupies the full height of the troposphere, with a narrow, localised updraft region at $r = 0$, and a much broader and less intense subsidence away from the cloud core. For typical values of the dimensional buoyancy frequency $N_0 = 0.01\text{s}^{-1}$, and tropopause height $H_T = 10^4\text{m}$, the maximum horizontal and vertical velocities of the fluid are approximately $w_{\max} \approx 10\text{ms}^{-1}$ and $u_{\max} \approx 5\text{ms}^{-1}$, broadly consistent with measurements of cumulus convection. The buoyancy perturbations are localised near to the heat source, and have a maximum dimensional value of approximately 0.65ms^{-2}. Note also that using the maximum horizontal velocity as a reference, and recalling that the local horizontal scale of motion in the cloud is given by $L_c = H_T \approx 10^4\text{m}$, the local Rossby number is given by $\text{Ro} = u_{\max}/L_c f_0 \approx 5$, indicating that the lack of rotation present in the equations governing the CCP is justified.

Another important quantity in this cloud model is the vertical gradient in total buoyancy, which is given in non-dimensional form as

$$N^2_{\text{tot}}(r,z) \equiv \partial_z b_{\text{tot}}(r,z) = 1 + \partial_z \bar{b}_0(r,z). \tag{4.72}$$

Whereas in a quiescent atmosphere, a stably stratified fluid must have $N^2 > 0$ everywhere, in our model it is required that $N^2_{\text{tot}} > 0$ so that instabilities caused by heavy air rising above light air do not occur. Another important aspect of deep convection is that the vertical gradient in the total buoyancy is significantly reduced in the cloud core compared with the background atmosphere. Contours of N^2_{tot} are shown in figure 4.2 which reflect this fact.

4.3.2 Solutions to the CPE

With the CCP solved, the only undetermined quantities in the correlation terms of (4.22–4.25) are the solutions of the cell problem $\tilde{\boldsymbol{u}}_0, \tilde{w}_0, \tilde{b}_0$. These are determined from the CPE (4.26–4.28) and can be expressed in terms of the solutions to the CCP (calculated in the previous section) and the large-scale variables $\boldsymbol{U}$ and B. Recalling that the large-scale quantities may be expanded in terms of the complete vertical basis functions $\phi_n(z), \Phi_n(z)$ for $n = 0, 1, 2, ...$ the cell problem governing

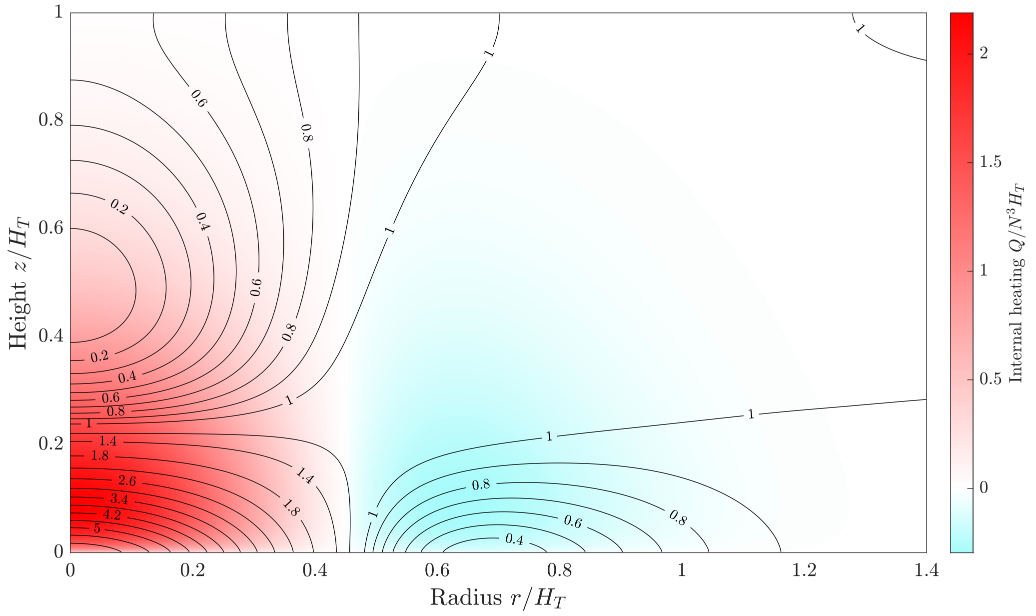

Figure 4.2: Contours of $N^2_{\text{tot}}(r,z)$ for the circulation driven by the heating profile (4.71) represented using colour.

the response of the fluid to the cloud field (4.26–4.28) may be written as

$$\begin{aligned}(\overline{\boldsymbol{v}}_0 \cdot \nabla)\,\tilde{\boldsymbol{v}}_0 + (\tilde{\boldsymbol{v}}_0 \cdot \nabla)\,\overline{\boldsymbol{v}}_0 + \nabla \tilde{p}_0 - \tilde{b}_0 \boldsymbol{k} - \nu_0 \nabla^2 \tilde{\boldsymbol{v}}_0 = \\ -\sum_{j=0}^{\infty} \left(\tilde{\boldsymbol{U}}_j \cdot \nabla\right) \overline{\boldsymbol{v}}_0 \phi_j - \sum_{j=0}^{\infty} \overline{w}_0 \tilde{\boldsymbol{U}}_j' \Phi_j,\end{aligned} \tag{4.73}$$

$$\nabla \cdot \tilde{\boldsymbol{v}}_0 = 0, \tag{4.74}$$

$$\begin{aligned}(\overline{\boldsymbol{v}}_0 \cdot \nabla)\,\tilde{b}_0 + (\tilde{\boldsymbol{v}}_0 \cdot \nabla)\,\overline{b}_0 + N^2 \tilde{w}_0 - \kappa_0 \nabla^2 \tilde{b}_0 = \\ -\sum_{j=0}^{\infty} \left(\tilde{\boldsymbol{U}}_j \cdot \nabla\right) \overline{b}_0 \phi_j - \sum_{j=0}^{\infty} \overline{w}_0 \tilde{B}_j' \phi_j.\end{aligned} \tag{4.75}$$

In the above equations we have expanded the terms involving the vertical gradient of the large-scale horizontal velocity and buoyancy using

$$\partial_z \boldsymbol{U}(\boldsymbol{x}, z, t) = \sum_{j=0}^{\infty} \tilde{\boldsymbol{U}}_j'(\boldsymbol{x}, t) \Phi_j(z), \tag{4.76}$$

$$\partial_z B(\boldsymbol{x}, z, t) = \sum_{j=0}^{\infty} \tilde{B}_j'(\boldsymbol{x}, t) \phi_j(z). \tag{4.77}$$

Whilst it is of course possible to carry the differential operator through the sum to act upon the basis functions in the modal decompositions of $\boldsymbol{U}$ and B, it is convenient for presentational purposes to keep track of coefficients in the expansions of $\partial_z \boldsymbol{U}$ and $\partial_z B$ explicitly. That is to say, it is more convenient to think of the coefficients in (4.76) and (4.77) as

$$\boldsymbol{U}_j'(\boldsymbol{x},t) = \frac{1}{c_j^2}\left[\int_0^1 \partial_z \boldsymbol{U}(\boldsymbol{x},z',t)\Phi_j('z)\,\mathrm{d}z' + \frac{1}{\alpha}\partial_z \boldsymbol{U}(x,1,t)\Phi_j(1)\right], \tag{4.78}$$

$$B_j'(\boldsymbol{x},t) = \int_0^1 \partial_z B(\boldsymbol{x},z',t)\phi_j(z')\,\mathrm{d}z', \tag{4.79}$$

rather than their counterparts involving integrals of $\boldsymbol{U}$ and B (which may indeed be recovered through integration by parts).

The solutions to the cell problem in the form (4.73–4.75), which are linear combinations of the basis coefficients $\tilde{\boldsymbol{U}}_j$, $\tilde{\boldsymbol{U}}_j'$ and $\tilde{B}_j'$, may be expressed as

$$\begin{aligned}\tilde{\boldsymbol{v}}_0 = \sum_{j=0}^{\infty} &\boldsymbol{e}_r\left[\hat{u}^r_{1,j}\left(\tilde{\boldsymbol{U}}_j\cdot\boldsymbol{e}_r\right) + \hat{u}^r_{2,j}\left(\tilde{\boldsymbol{U}}_j'\cdot\boldsymbol{e}_r\right) + \hat{u}^r_{3,j}\tilde{B}_j'\right] \\ &+ \boldsymbol{e}_\theta\left[\hat{u}^\theta_{1,j}\left(\tilde{\boldsymbol{U}}_j\cdot\boldsymbol{e}_\theta\right) + \hat{u}^\theta_{2,j}\left(\tilde{\boldsymbol{U}}_j'\cdot\boldsymbol{e}_\theta\right)\right] \\ &+ \boldsymbol{k}\left[\hat{w}_{1,j}\left(\tilde{\boldsymbol{U}}_j\cdot\boldsymbol{e}_r\right) + \hat{w}_{2,j}\left(\tilde{\boldsymbol{U}}_j'\cdot\boldsymbol{e}_r\right) + \hat{w}_{3,j}\tilde{B}_j'\right],\end{aligned} \tag{4.80}$$

$$\tilde{p}_0 = \sum_{j=0}^{\infty}\left[\hat{p}_{1,j}\left(\tilde{\boldsymbol{U}}_j\cdot\boldsymbol{e}_r\right) + \hat{p}_{2,j}\left(\tilde{\boldsymbol{U}}_j'\cdot\boldsymbol{e}_r\right) + \hat{p}_{3,j}\tilde{B}_j'\right], \tag{4.81}$$

$$\tilde{b}_0 = \sum_{j=0}^{\infty}\left[\hat{b}_{1,j}\left(\tilde{\boldsymbol{U}}_j\cdot\boldsymbol{e}_r\right) + \hat{b}_{2,j}\left(\tilde{\boldsymbol{U}}_j'\cdot\boldsymbol{e}_r\right) + \hat{b}_{3,j}\tilde{B}_j'\right], \tag{4.82}$$

where the variables $\{\hat{u}^r_{k,j}, \hat{u}^\theta_{k,j}, \hat{w}_{k,j}, \hat{p}_{k,j}, \hat{b}_{k,j}\}$ for $k = 1, 2, 3$ are determined by three separate 'kernel cell problems' (KCP1, KCP2, KCP3 hereafter). The advantage of using the ansatz (4.80–4.82) is that the θ dependence of $\tilde{\boldsymbol{v}}_0, \tilde{p}_0, \tilde{b}_0$ is contained entirely within the polar coordinate basis vectors $\boldsymbol{e}_r = (\cos\theta, \sin\theta, 0)^T$ and $\boldsymbol{e}_\theta = (-\sin\theta, \cos\theta, 0)^T$, and so the resulting KCPs are axisymmetric. KCP1–KCP3 are determined by substituting (4.80–4.82) into equations (4.73–4.75) and matching the basis coefficients. The problem KCP1 for variables $\{\hat{u}^r_{1,j}, \hat{u}^\theta_{1,j}, \hat{w}_{1,j}, \hat{p}_{1,j}, \hat{b}_{1,j}\}$ is given by

$$\frac{1}{r}\partial_z\overline{\psi}_0\partial_r\hat{u}^r_{1,j}+\partial_r\left(\frac{1}{r}\partial_r\overline{\psi}_0\right)\hat{u}^r_{1,j}-\frac{1}{r}\partial_r\overline{\psi}_0\partial_z\hat{u}^r_{1,j}+\hat{w}_{1,j}\partial^2_{zz}\overline{\psi}_0-\partial_r\hat{p}_{1,j} \tag{4.83}$$

$$+\nu_0\left(\frac{1}{r}\partial_r\left(r\partial_r\hat{u}^r_{1,j}\right)-\frac{2}{r^2}\left(\hat{u}^r_{1,j}-\hat{u}^\theta_{1,j}\right)+\partial^2_{zz}\hat{u}^r_{1,j}\right)=-\,\phi_j\partial_r\left(\frac{1}{r}\partial_z\overline{\psi}_0\right),$$

$$\frac{1}{r}\partial_z\overline{\psi}_0\partial_r\hat{u}^\theta_{1,j}+\frac{\hat{u}^\theta_{1,j}}{r^2}\partial_z\overline{\psi}_0-\frac{1}{r}\partial_r\overline{\psi}_0\partial_z\hat{u}^\theta_{1,j}-\frac{1}{r}\hat{p}_{1,j} \tag{4.84}$$

$$+\nu_0\left(\frac{1}{r}\partial_r\left(r\partial_r\hat{u}^\theta_{1,j}\right)+\frac{2}{r^2}\left(\hat{u}^r_{1,j}-\hat{u}^\theta_{1,j}\right)+\partial^2_{zz}\hat{u}^r_{1,j}\right)=-\,\frac{\phi_j}{r^2}\partial_z\overline{\psi}_0,$$

$$\partial_r\left(\frac{1}{r}\partial_r\overline{\psi}_0\right)\hat{u}^r_{1,j}-\frac{1}{r}\partial_z\overline{\psi}_0\partial_r\hat{w}_{1,j}+\frac{1}{r}\partial_r\overline{\psi}_0\partial_z\hat{w}_{1,j}+\frac{\hat{w}_{1,j}}{r}\partial^2_{rz}\overline{\psi}_0 \tag{4.85}$$

$$+\partial_z\hat{p}_{1,j}-\hat{b}_{1,j}-\nu_0\left(\frac{1}{r}\partial_r\left(r\partial_r\hat{w}_{1,j}\right)-\hat{w}_{1,j}+\partial^2_{zz}\hat{w}_{1,j}\right)=-\,\phi_j\partial_r\left(\frac{1}{r}\partial_r\overline{\psi}_0\right),$$

$$\frac{1}{r}\partial_r\left(r\hat{u}^r_{1,j}\right)-\frac{\hat{u}^\theta_{1,j}}{r}+\partial_z\hat{w}_{1,j}=0, \tag{4.86}$$

$$\hat{u}^r_{1,j}\partial_r\overline{b}_0+\hat{w}_{1,j}\left(\partial_z\overline{b}_0+1\right)-\frac{1}{r}\partial_z\overline{\psi}_0\partial_r\hat{b}_{1,j}+\frac{1}{r}\partial_r\overline{\psi}_0\partial_z\hat{b}_{1,j} \tag{4.87}$$

$$-\kappa_0\left(\frac{1}{r}\partial_r\left(r\partial_r\hat{b}_{1,j}\right)-\frac{1}{r^2}\hat{b}_{1,j}+\partial^2_{zz}\hat{b}_{1,j}\right)=-\,\phi_j\partial_r\overline{b}_0.$$

The solutions of (4.83–4.87) are found using a Chebyshev collocation method with the same numerical parameters as for the CCP. The boundary conditions for this problem are

$$\frac{\partial\hat{u}^r_{1,j}}{\partial z}=\frac{\partial\hat{u}^\theta_{1,j}}{\partial z}=\hat{w}_{1,j}=\hat{b}_{1,j}=0,\qquad \text{at}\quad z=0,1, \tag{4.88}$$

$$\frac{\partial\hat{u}^r_{1,j}}{\partial r}=\frac{\partial\hat{u}^\theta_{1,j}}{\partial r}=\hat{w}_{1,j}=\hat{p}_{1,j}=\hat{b}_{1,j}=0,\qquad \text{at}\quad r=0, \tag{4.89}$$

$$\hat{u}^r_{1,j}=\frac{\partial\hat{u}^\theta_{1,j}}{\partial r}=\frac{\partial\hat{w}_{1,j}}{\partial r}=\hat{b}_{1,j}=0,\qquad \text{at}\quad r=r_{\text{out}}, \tag{4.90}$$

which, again, are straightforward to implement in the Chebyshev numerical formulation. Figure 4.3 shows contours of the solutions $\{\hat{u}^r_{1,1},\hat{u}^\theta_{1,1},\hat{w}_{1,1},\hat{p}_{1,1},\hat{b}_{1,1}\}$ to KCP1 corresponding to the first baroclinic wave mode $(j=1)$.

The problem KCP2 corresponding to the variables $\{\hat{u}^r_{2,j},\hat{u}^\theta_{2,j},\hat{w}_{2,j},\hat{p}_{2,j},\hat{b}_{2,j}\}$ is similar to KCP1, in that only the source terms are different whilst the operator

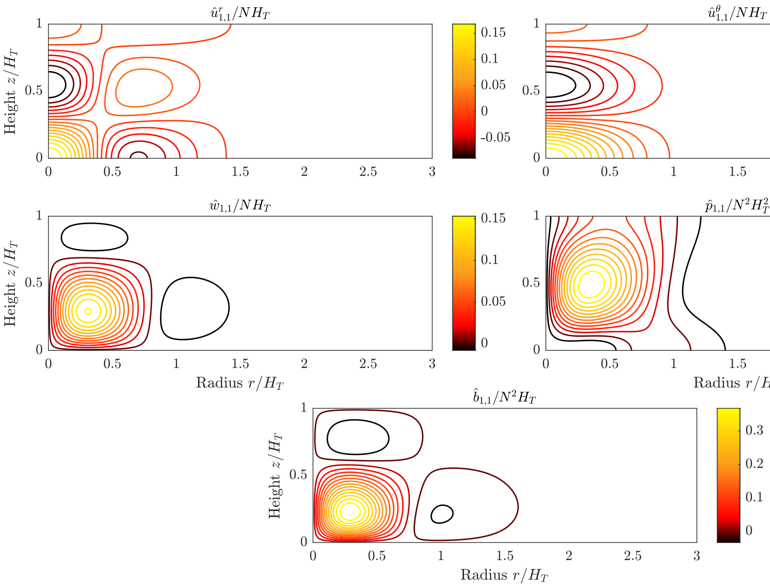

Figure 4.3: Contours of the KCP1 solutions $\{\hat{u}^r_{1,1}, \hat{u}^\theta_{1,1}, \hat{w}_{1,1}, \hat{p}_{1,1}, \hat{b}_{1,1}\}$ to (4.83–4.87) with the boundary conditions (4.88–4.90). The values $\nu_0 = \kappa_0 = 0.05$ are used.

acting on the variables remains unchanged. It is given by

$$\begin{aligned}\frac{1}{r}\partial_z\overline{\psi}_0\partial_r\hat{u}^r_{2,j} + \partial_r\left(\frac{1}{r}\partial_r\overline{\psi}_0\right)\hat{u}^r_{2,j} - \frac{1}{r}\partial_r\overline{\psi}_0\partial_z\hat{u}^r_{2,j} + \hat{w}_{2,j}\partial^2_{zz}\overline{\psi}_0 - \partial_r\hat{p}_{2,j}& \\ +\nu_0\left(\frac{1}{r}\partial_r\left(r\partial_r\hat{u}^r_{2,j}\right) - \frac{2}{r^2}\left(\hat{u}^r_{2,j} - \hat{u}^\theta_{2,j}\right) + \partial^2_{zz}\hat{u}^r_{2,j}\right) = \frac{\Phi_j}{r}\partial_r\overline{\psi}_0,&\end{aligned} \tag{4.91}$$

$$\begin{aligned}\frac{1}{r}\partial_z\overline{\psi}_0\partial_r\hat{u}^\theta_{2,j} + \frac{\hat{u}^\theta_{2,j}}{r^2}\partial_z\overline{\psi}_0 - \frac{1}{r}\partial_r\overline{\psi}_0\partial_z\hat{u}^\theta_{2,j} - \frac{1}{r}\hat{p}_{2,j}& \\ +\nu_0\left(\frac{1}{r}\partial_r\left(r\partial_r\hat{u}^\theta_{2,j}\right) + \frac{2}{r^2}\left(\hat{u}^r_{2,j} - \hat{u}^\theta_{2,j}\right) + \partial^2_{zz}\hat{u}^r_{2,j}\right) = \frac{\Phi_j}{r}\partial_r\overline{\psi}_0,&\end{aligned} \tag{4.92}$$

$$\begin{aligned}\partial_r\left(\frac{1}{r}\partial_r\overline{\psi}_0\right)\hat{u}^r_{2,j} - \frac{1}{r}\partial_z\overline{\psi}_0\partial_r\hat{w}_{2,j} + \frac{1}{r}\partial_r\overline{\psi}_0\partial_z\hat{w}_{2,j} + \frac{\hat{w}_{2,j}}{r}\partial^2_{rz}\overline{\psi}_0& \\ +\partial_z\hat{p}_{2,j} - \hat{b}_{2,j} - \nu_0\left(\frac{1}{r}\partial_r\left(r\partial_r\hat{w}_{2,j}\right) - \hat{w}_{2,j} + \partial^2_{zz}\hat{w}_{2,j}\right) = 0,&\end{aligned} \tag{4.93}$$

$$\frac{1}{r}\partial_r\left(r\hat{u}^r_{2,j}\right) - \frac{\hat{u}^\theta_{2,j}}{r} + \partial_z\hat{w}_{2,j} = 0, \tag{4.94}$$

$$\begin{aligned}\hat{u}^r_{2,j}\partial_r\overline{b}_0 + \hat{w}_{2,j}\left(\partial_z\overline{b}_0 + 1\right) - \frac{1}{r}\partial_z\overline{\psi}_0\partial_r\hat{b}_{2,j} + \frac{1}{r}\partial_r\overline{\psi}_0\partial_z\hat{b}_{2,j}& \\ -\kappa_0\left(\frac{1}{r}\partial_r\left(r\partial_r\hat{b}_{2,j}\right) - \frac{1}{r^2}\hat{b}_{2,j} + \partial^2_{zz}\hat{b}_{2,j}\right) = 0.&\end{aligned} \tag{4.95}$$

The boundary conditions for KCP2 are the same as those for KCP1, and so it is solved in exactly the same manner. Figure 4.4 shows contours of the solutions

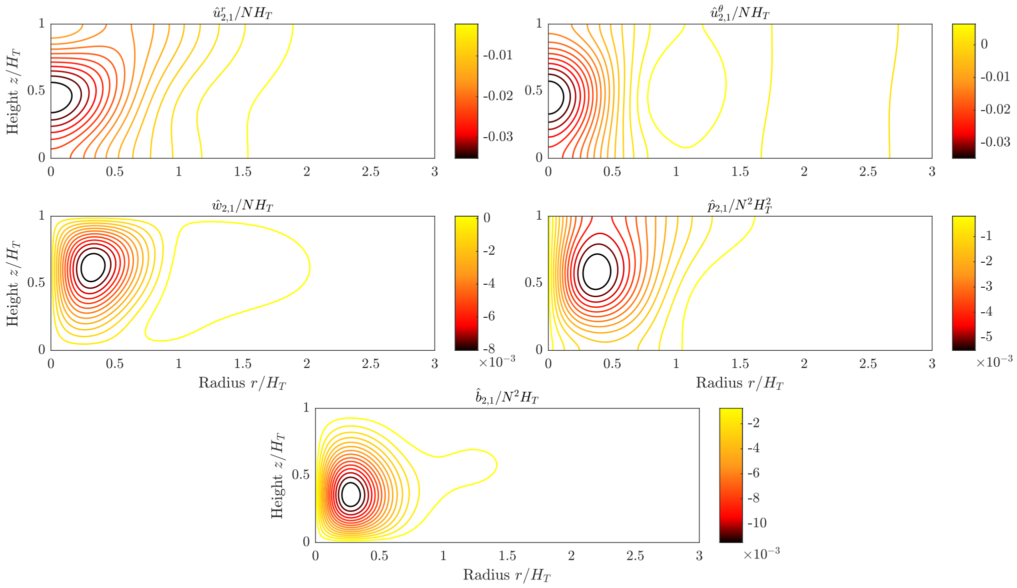

Figure 4.4: Contours of the KCP2 solutions $\{\hat{u}^r_{2,1}, \hat{u}^\theta_{2,1}, \hat{w}_{2,1}, \hat{p}_{2,1}, \hat{b}_{2,1}\}$ to (4.91–4.95) with the boundary conditions (4.88–4.90). The values $\nu_0 = \kappa_0 = 0.05$ are used.

$\{\hat{u}^r_{2,1}, \hat{u}^\theta_{2,1}, \hat{w}_{2,1}, \hat{p}_{2,1}, \hat{b}_{2,1}\}$ to KCP2 corresponding to the first baroclinic wave mode $(j = 1)$.

KCP3 is somewhat different to KCP1 and KCP2. Notably, there is no azimuthal component of velocity and so we are able to rewrite the system in streamfunction-vorticity form using the definitions

$$\hat{u}^r_{3,j} = -\frac{1}{r}\frac{\partial \hat{\psi}_{3,j}}{\partial z}, \qquad \hat{w}_{3,j} = \frac{1}{r}\frac{\partial \hat{\psi}_{3,j}}{\partial r}, \tag{4.96}$$

and

$$\hat{\zeta}_{3,j} = \frac{\partial \hat{w}_{3,j}}{\partial r} - \frac{\partial \hat{u}^r_{3,j}}{\partial z}. \tag{4.97}$$

In this formulation, KCP3 may be written in terms of the variables $\{\hat{\psi}_{3,j}, \hat{\zeta}_{3,j}, \hat{b}_{3,j}\}$

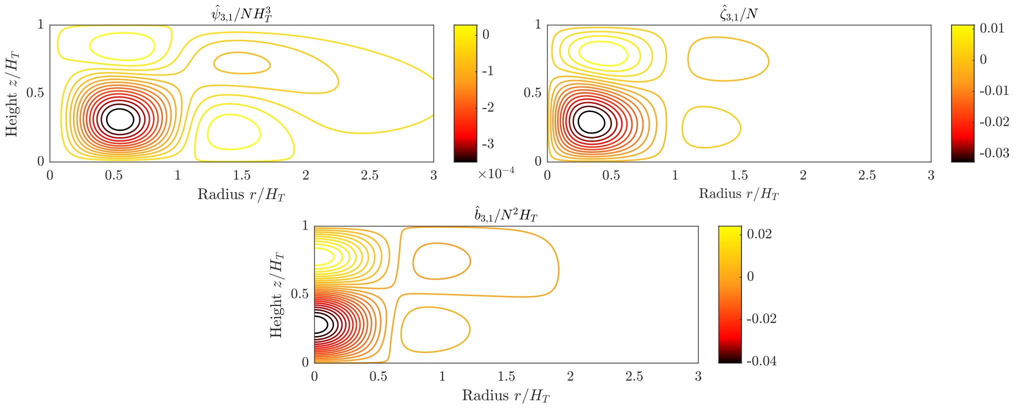

Figure 4.5: Contours of the solutions $\{\hat{\psi}_{3,1}, \hat{\zeta}_{3,1}, \hat{b}_{3,1}\}$ to (4.98–4.100) with the boundary conditions (4.62–4.64). The values $\nu_0 = \kappa_0 = 0.05$ are used.

as

$$\mathcal{J}\left(\overline{\psi}_0, \frac{\hat{\zeta}_{3,j}}{r}\right) + \mathcal{J}\left(\hat{\psi}_{3,j}, \frac{\overline{\zeta}_0}{r}\right) - \partial_r \hat{b}_{3,j} \tag{4.98}$$

$$-\nu_0\left(\frac{1}{r}\partial_r\left(r\partial_r\hat{\zeta}_{3,j}\right) - \frac{\hat{\zeta}_{3,j}}{r^2} + \partial^2_{zz}\hat{\zeta}_{3,j}\right) = 0,$$

$$\hat{\zeta}_{3,j} - \frac{1}{r}\left(\partial^2_{rr}\hat{\psi}_{3,j} - \frac{1}{r}\partial_r\hat{\psi}_{3,j} + \partial^2_{zz}\hat{\psi}_{3,j}\right) = 0, \tag{4.99}$$

$$\frac{1}{r}\mathcal{J}\left(\overline{\psi}_0, \hat{b}_{3,j}\right) + \frac{1}{r}\mathcal{J}\left(\hat{\psi}_{3,j}, \overline{b}_0\right) + \frac{1}{r}\partial_r\hat{\psi}_{3,j} \tag{4.100}$$

$$-\kappa_0\left(\frac{1}{r}\partial_r\left(r\partial_r\hat{b}_{3,j}\right) + \partial^2_{zz}\hat{b}_{3,j}\right) = -\frac{\phi_j}{r}\partial_r\overline{\psi}_0.$$

The boundary conditions are the same as (4.62–4.64) used to solve the CCP. Figure 4.5 shows contours of the solutions $\{\hat{\psi}_{3,1}, \hat{\zeta}_{3,1}, \hat{b}_{3,1}\}$ to KCP3 corresponding to the first baroclinic wave mode ($j = 1$). The variables $\{\hat{u}^r_{3,j}, \hat{w}_{3,j}, \hat{p}_{3,j}, \hat{b}_{3,j}\}$ in (4.80–4.82) can be calculated from $\{\hat{\psi}_{3,j}, \hat{\zeta}_{3,j}, \hat{b}_{3,j}\}$ by Chebyshev differentiation, however it is sufficient to leave them in their current form to calculate the correlation terms in (4.22–4.25).

4.3.3 The homogenised equations

Having established a numerical method to solve the CCP, as well as a numerical method to invert KCP1-KCP3, it is now possible to explicitly calculate the form of the correlation terms in the averaged equations (4.22–4.25). Determining the correlation terms leads to the central result of this chapter, namely a system of integro-differential equations governing the response of the large-scale variables to any imposed cloud field. We present them here along with a discussion of their implications, and postpone a formal derivation and numerical calculation of the correlation terms to later sections.

The response of the large-scale variables $\boldsymbol{U}, W, P, B$ to a convective cloud field is governed by the homogenised equations

$$\frac{\partial \boldsymbol{U}}{\partial t} + f\boldsymbol{k} \times \boldsymbol{U} + n\frac{\partial}{\partial z}\left(\mathcal{K}_1 \boldsymbol{U}\right) = -\nabla_{\boldsymbol{x}} P + n\frac{\partial}{\partial z}\left(\mathcal{K}_2 \frac{\partial \boldsymbol{U}}{\partial z}\right), \tag{4.101}$$

$$\frac{\partial P}{\partial z} = B, \tag{4.102}$$

$$\nabla_{\boldsymbol{x}} \cdot \boldsymbol{U} + \frac{\partial W}{\partial z} = 0, \tag{4.103}$$

$$\frac{\partial B}{\partial t} + W = n\frac{\partial}{\partial z}\left(\mathcal{L}\frac{\partial B}{\partial z}\right), \tag{4.104}$$

where $\mathcal{K}_1, \mathcal{K}_2$ and $\mathcal{L}$ are non-local integral operators, which act on a z-dependent function $G(z)$ as

$$\mathcal{K}_1 G = \int_0^1 K_1(z,z')G(z')\,\mathrm{d}z', \qquad \mathcal{K}_2 G = \int_0^1 K_2(z,z')G(z')\,\mathrm{d}z',$$
$$\mathcal{L} G = \int_0^1 L(z,z')G(z')\,\mathrm{d}z'. \tag{4.105}$$

The integral kernels $K_1(z,z')$, $K_2(z,z')$ and $L(z,z')$ (the form of which we derive in the following subsections) are smooth functions which are fully determined by the cloud field. These kernels bear resemblance to *transilient matrices* - a concept which has its origin in the theory of turbulence (Stull, 1984; Romps and Kuang, 2011; Bhamidipati et al., 2020) where the non-local action of the integral operators quantifies the manner in which small, turbulent eddies transport fluid particles instantaneously over a finite distance. Similar matrices have been used in Cheng et al. (2017) to model the instantaneous convective adjustment of a moist atmosphere to a statically stable equilibrium state.

In our problem, the homogenised equations (4.101–4.104) provide insight into how a convective cloud field affects the propagation of long waves. The three transilient kernels in this case quantify the vertical redistribution of horizontal momentum and buoyancy due to the large-scale flow interacting with clouds. Importantly, the non-locality of the operators reflects the fact that convection occurs over a much shorter time-scale than that upon which the large-scale flow evolves. In this sense, the integral terms in (4.101–4.104) provide a closure for a time-dependent convective adjustment problem. It is perhaps unsurprising that transilient kernels arise naturally in our problem, since thermals and large-scale convective processes are analogous to large eddies in the atmosphere. Furthermore, convection is a mixing process and so is expected to have an analogous effect on the atmosphere in many contexts.

The boundary conditions for (4.101–4.104) appropriate to an atmosphere with a rigid lid are

$$\partial_z \boldsymbol{U} = 0, \qquad W = B = 0, \qquad \text{on} \qquad z = 0, 1. \tag{4.106}$$

4.3.3.1 Derivation of the homogenised equations (4.101–4.104)

Recall that the solutions to KCP1-KCP3 in the previous section are independent of θ, and that the θ dependence of (4.80–4.82) is contained entirely within the horizontal basis vectors $\boldsymbol{e}_r = (\cos\theta, \sin\theta, 0)^T, \boldsymbol{e}_\theta = (-\sin\theta, \cos\theta, 0)^T$. As a consequence of this, and from the definition of the averaging operator (4.15), all correlation terms involving only one multiple of the horizontal basis functions vanish, since they are proportional to $\sin\theta$ or $\cos\theta$. This results in the momentum correlation term in (4.22) containing only contributions from the terms in the kernel cell problems KCP1 and KCP2 (i.e. $k = 1, 2$), and the buoyancy correlation term in (4.25) containing only contributions from the kernel cell problem KCP3 (i.e. $k = 3$). Substituting (4.80–4.82) into (4.22) and (4.25) allows the correlation terms to be written

$$\langle \overline{w}_0 \tilde{\boldsymbol{u}}_0 + \tilde{w}_0 \overline{\boldsymbol{u}}_0 \rangle_0 = \sum_{j=0}^{\infty} K_{1,j}(z) \tilde{\boldsymbol{U}}_j(\boldsymbol{x}, t) + K_{2,j}(z) \tilde{\boldsymbol{U}}'_j(\boldsymbol{x}, t), \tag{4.107}$$

$$\left\langle \overline{w}_0 \tilde{b}_0 + \tilde{w}_0 \overline{b}_0 \right\rangle_0 = \sum_{j=0}^{\infty} L_j(z) \tilde{B}'_j(\boldsymbol{x}, t), \tag{4.108}$$

where

$$K_{k,j}(z) = \pi \int_0^{\infty} \partial_r \overline{\psi}_0 \left(\hat{u}^r_{k,j} + \hat{u}^{\theta}_{k,j} \right) - \partial_z \overline{\psi}_0 \hat{w}_{k,j} \, \mathrm{d}r, \tag{4.109}$$

$$L_j(z) = 2\pi \int_0^{\infty} \partial_r \overline{\psi}_0 \hat{b}_{3,j} + \overline{b}_0 \partial_r \hat{\psi}_{3,j} \, \mathrm{d}r, \tag{4.110}$$

for $k = 1, 2$. In order to express the averaged equations in terms of the height dependent large-scale variables, we first use the integral properties (4.45) and (4.51), along with the boundary conditions (4.106) to express $\tilde{\boldsymbol{U}}_j$, $\tilde{\boldsymbol{U}}'_j$ and $\tilde{B}'_j$ as

$$\tilde{\boldsymbol{U}}_j = \int_0^1 \boldsymbol{U}(\boldsymbol{x}, z', t) \phi_j(z') \, \mathrm{d}z', \tag{4.111}$$

$$\tilde{\boldsymbol{U}}'_j = \frac{1}{c_j^2} \int_0^1 \partial_z \boldsymbol{U}(\boldsymbol{x}, z', t) \Phi_j(z') \, \mathrm{d}z', \tag{4.112}$$

$$\tilde{B}'_j = \int_0^1 \partial_z B(\boldsymbol{x}, z', t) \phi_j(z') \, \mathrm{d}z'. \tag{4.113}$$

Inserting these expressions into (4.22–4.25), we retrieve the equations(4.101–4.104), with the transilient kernels defined by

$$K_1(z, z') = \sum_{j=0}^{\infty} K_{1,j}(z) \phi_j(z'), \tag{4.114}$$

$$K_2(z, z') = -\sum_{j=0}^{\infty} \frac{1}{c_j^2} K_{2,j}(z) \Phi_j(z'), \tag{4.115}$$

$$L(z, z') = -\sum_{j=0}^{\infty} L_j(z) \phi_j(z'). \tag{4.116}$$

4.3.3.2 Properties of the transilient kernels

Consider the one dimensional non-local transport equation for a tracer with concentration $c(z, t)$, given by

$$\partial_t c + \int_0^1 K(z, z')c(z', t)\ \mathrm{d}z' = 0, \tag{4.117}$$

defined on $(z, t) \in [0, 1] \times [0, \infty)$, and where $K(z, z')$ is a transilient kernel. In this context, the value of $K(z, z')$ at a point (z, z') quantifies the rate at which fluid parcels at an initial height z' are transported to a final height z by e.g. a turbulent eddy (Romps and Kuang, 2011; Stull, 1984; Bhamidipati et al., 2020). Assuming that c is a conserved quantity, it follows that

$$\int_0^1 K(z, z')\ \mathrm{d}z = 0, \tag{4.118}$$

which ensures that the net sink of tracer concentration c over all z destinations is zero. Furthermore, it must also be true that

$$\int_0^1 K(z, z')\ \mathrm{d}z' = 0, \tag{4.119}$$

since if c is initially constant in z, the tracer concentration should remain constant for all time. This property reflects the fact that the eddies may not act to 'un-mix' the fluid (Shnirelman, 1993; Wood and Mcintyre, 2009; Shnirelman, 2013).

In our problem, the operators introduced by the presence of convection are seen to obey property (4.118). This can be shown by taking the integral in z from 0 to 1 of equations (4.101–4.104), after which the contribution of the integral operators is zero. This reflects the fact that the net sink of horizontal momentum and buoyancy over all z destinations due to the motions induced by convection is zero. Likewise, it is also seen that choosing B to have a constant vertical profile leads to the the integral operator term involving $\mathcal{L}$ vanishing. Whilst choosing $\boldsymbol{U}$ to have a constant vertical profile does cause the term involving $\mathcal{K}_2$ to vanish, the same is not true for

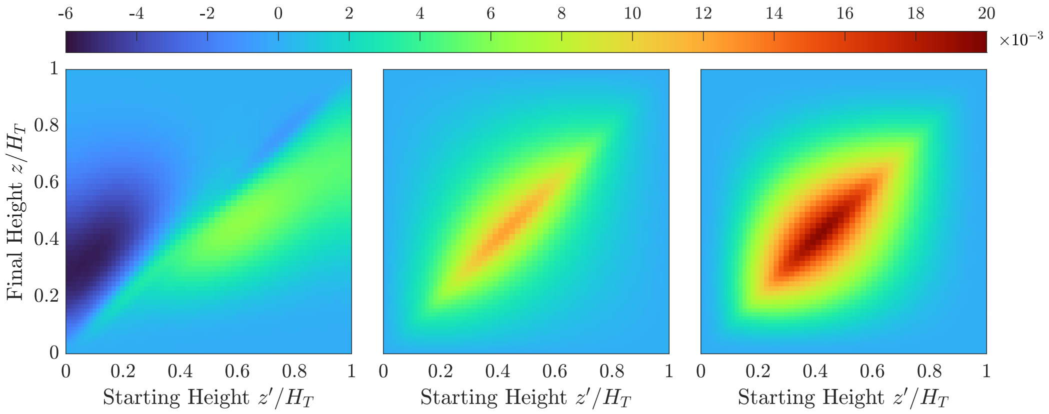

Figure 4.6: Colour plots of the transilient kernels $K_1(z,z')$, $K_2(z,z')$ and $L(z,z')$ (left to right). Both z and z' are discretised using a Chebyshev grid with 81 points, and the infinite sum is truncated at $N_s = 21$.

the term involving $\mathcal{K}_1$, which can be seen from the fact that

$$\int_0^1 \partial_z K_1(z,z')\,\mathrm{d}z' = \partial_z K_{1,0}(z)\phi_0(1) \neq 0. \tag{4.120}$$

This implies that a horizontal momentum profile which is initially constant in z may develop vertical variations in the presence of a cloud field. Importantly, horizontal momentum is not transported as a tracer in the homogenised equations (4.101–4.104), and so no physical laws are violated by this fact.

4.3.3.3 Numerical calculations of the transilient kernels

In order to calculate the transilient kernels in our numerical formulation, the vertical domain is discretised using a Chebyshev mesh with 81 points in each of z and z'. Furthermore, the infinite series definitions of the matrices may be approximated by truncating the sum at some finite number of terms, say N_s. Figure 4.6 shows a colour plot of the three transilient kernels in our problem using $N_s = 20$.

The convergence of the matrices as a function of the truncation number N_s is now investigated. Firstly, we define the truncated matrices as, for example

$$K_1^{N_s}(z,z') = \sum_{j=0}^{N_s} K_{1,j}(z)\phi_j(z'), \tag{4.121}$$

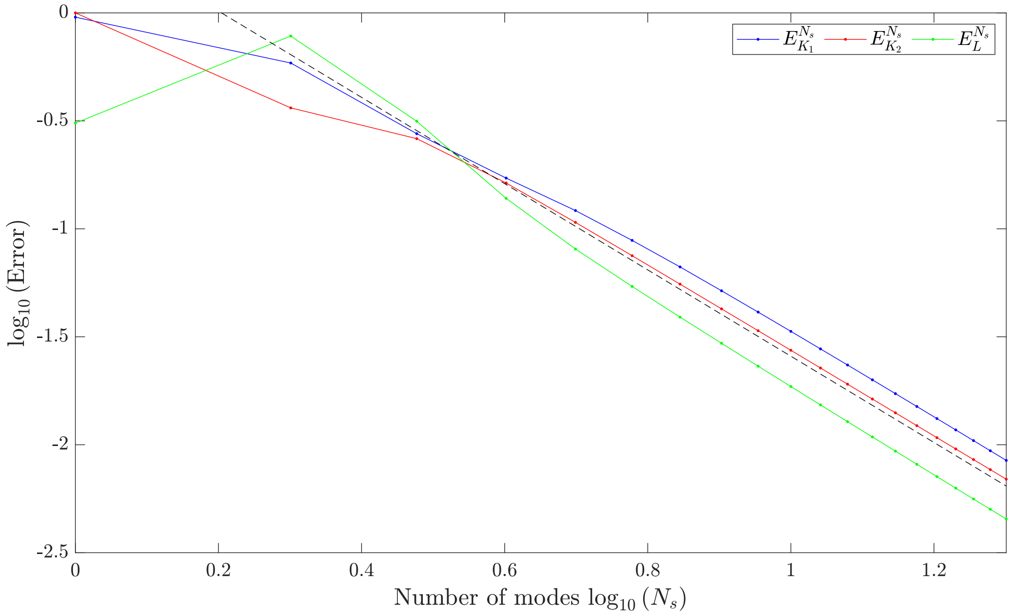

Figure 4.7: Log-log plot of the step-wise errors in the transilient kernels as a function of N_s. The parameters $N_z = 81$, $N_r = 31$ and $r_{\text{out}} = 5$ are fixed. The dashed line is a linear approximant to the average error for $N_s \geq 6$ calculated using a least squares regression method, the gradient of which is approximately -2.00.

so that we may then define a step-wise error for the matrix $K_1^{N_s}$ as

$$E_{K_1}^{N_s} = \frac{\|K_1^{N_s} - K_1^{N_s-1}\|_{L^2}}{\|K_1^{N_s}\|_{L^2}}, \tag{4.122}$$

where $\|\cdot\|_{L^2}$ is the L^2-norm. Figure 4.7 shows a log-log plot of the errors $E_{K_1}^{N_s}$, $E_{K_2}^{N_s}$ and $E_L^{N_s}$ as functions of N_s for fixed $N_z = 81$, $N_r = 31$ and $r_{\text{out}} = 5$, and where $E_{K_2}^{N_s}$ and $E_L^{N_s}$ are defined analogously to (4.122). The dashed line in the figure is calculated using a least squares regression method on the average of the three errors for mode numbers $N_s \geq 6$. The gradient of this line is found to be $\mu \approx -2.00$, indicating that the errors decay as $E_{K_1}^{N_s}, E_{K_2}^{N_s}, E_L^{N_s} \sim 1/N_s^2$. Importantly, the errors decrease at an algebraic rate faster than $1/N_s$, and therefore may not accumulate at each step so that the total error diverges as $N_s \to \infty$.

To test the convergence of the matrices as functions of both N_r and r_{out}, we define two further errors as

$$E_{K_1}^{N_r} = \frac{\|K_1^{N_r} - K_1^{N_r-2}\|_{L^2}}{\|K_1^{N_r}\|_{L^2}}, \qquad E_{K_1}^{r_{\text{out}}} = \frac{\|K_1^{r_{\text{out}}} - K_1^{r_{\text{out}}-1}\|_{L^2}}{\|K_1^{r_{\text{out}}}\|_{L^2}}, \tag{4.123}$$

where $K_1^{N_r}$ and $K_1^{r_{\text{out}}}$ are given by (4.121) with $N_s = 20$. In $K_1^{N_r}$, the $K_{1,j}$'s are calculated using N_r radial Chebyshev points with $r_{\text{out}} = 5$ fixed, and in $K_1^{r_{\text{out}}}$, the $K_{1,j}$'s are calculated using 31 Chebyshev points whilst r_{out} may vary. In both cases $N_z = 81$ is fixed.

The top panel of figure 4.8 shows log plots of $E_{K_1}^{N_r}$, $E_{K_2}^{N_r}$ and $E_L^{N_r}$ as functions of N_r. Their decay in the log plot is approximately linear, indicating that their actual decay rate is exponential and that our numerical method has spectral accuracy in the radial direction. The dashed line in this panel is calculated using a least squares regression method based on the average of the three errors, and is found to have a gradient of approximately -0.22, indicating that the errors decay as $E_{K_1}^{N_r}, E_{K_2}^{N_r}, E_L^{N_r} \sim \exp(-0.22N_r)$.

The bottom panel of figure 4.8 shows log-log plots of $E_{K_1}^{r_{\text{out}}}$, $E_{K_2}^{r_{\text{out}}}$ and $E_L^{r_{\text{out}}}$ as functions of r_{out}. The errors are seen to decrease rapidly at first (approximately linearly on the log-log plot, corresponding to an algebraic decay), followed by a small increase. Importantly, this increase only occurs after the error introduced by the discretisation of r using 31 Chebyshev points surpasses the error introduced by truncating the domain at r_{out}. This indicates that the error increase at $r_{\text{out}} \approx 5$ is due to the grid resolution on the larger domain no longer being fine enough to resolve the radial structures. It is reasonable however, to conclude that the errors decay algebraically as r_{out} is increased, assuming that we are able to resolve radial structures with a fine enough Chebyshev discretisation. The dashed line in this panel is calculated using a least squares regression method based on the average of the three errors for $r_{\text{out}} \leq 5$, and has a gradient of approximately -8.64, indicating that the errors decay as $E_{K_1}^{r_{\text{out}}}, E_{K_2}^{r_{\text{out}}}, E_L^{r_{\text{out}}} \sim r_{\text{out}}^{-8.64}$.

Demonstrating the convergence of the transilient kernels as a function of the number of vertical grid points N_z is somewhat more challenging since the size of the discretised matrices increases at each iteration. Instead, we analyse the convergence of the individual functions $K_{1,j}(z)$, $K_{2,j}(z)$ and $L_j(z)$ in the expansions (4.114–4.116) by projecting them onto a suitable basis. Since all of the functions vanish on $z = 0, 1$ for all $j = 0, 1, 2...$, we opt to use a Fourier sine series. That is, we expand

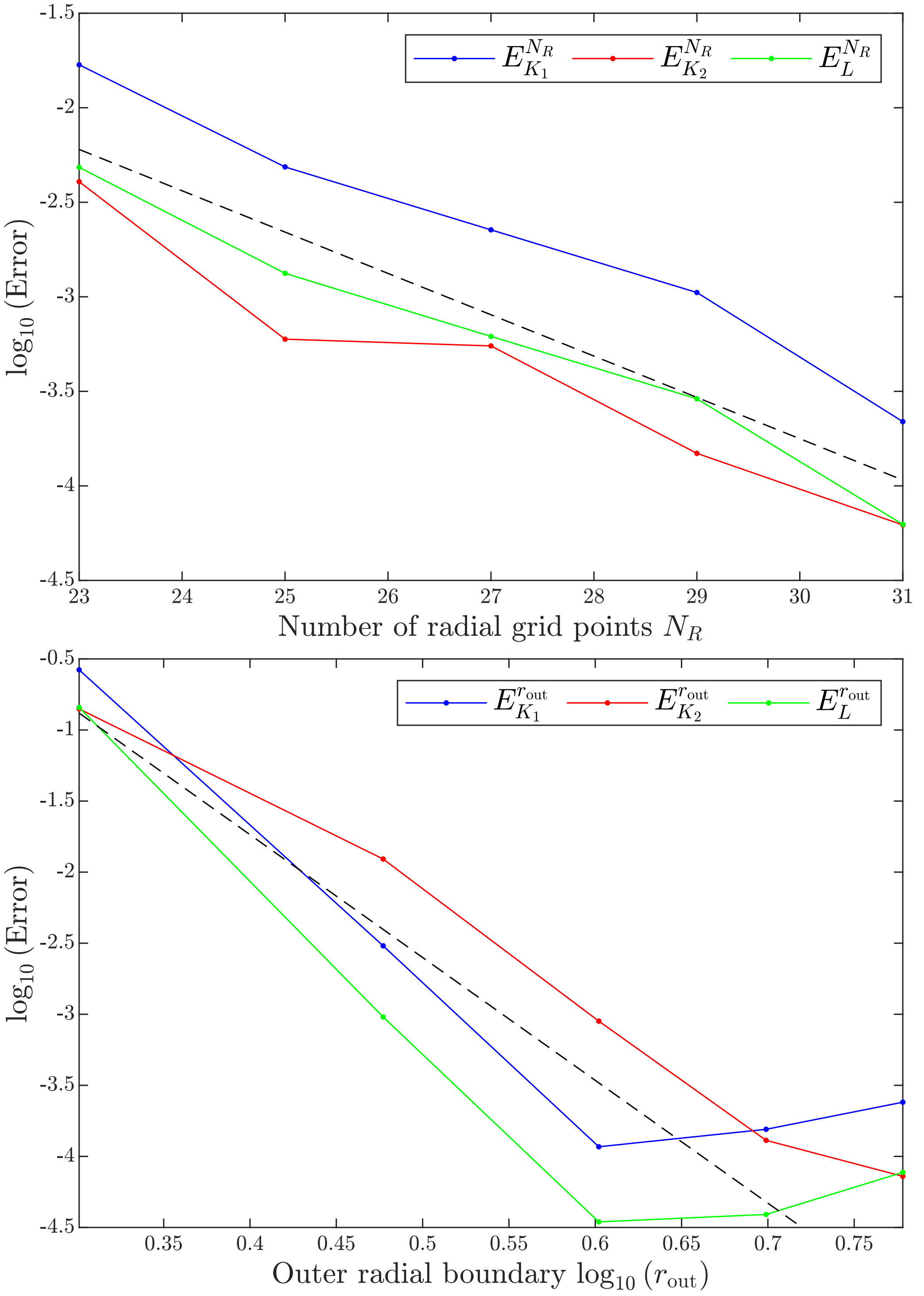

Figure 4.8: Top panel: log plots of $E_{K_1}^{N_r}$, $E_{K_2}^{N_r}$ and $E_{L}^{N_r}$ as functions of N_r. The parameters $N_z = 81$, $N_s = 20$ and $r_{\text{out}} = 5$ are fixed. The dashed line is a linear approximant to the average error calculated using a least squares regression method, the gradient of which is approximately -0.22. Bottom panel: log-log plots of $E_{K_1}^{r_{\text{out}}}$, $E_{K_2}^{r_{\text{out}}}$ and $E_{L}^{r_{\text{out}}}$ as functions of r_{out}. The parameters $N_z = 81$, $N_s = 20$ and $N_r = 31$ are fixed. The dashed line is a linear approximant to the average error for $r_{\text{out}} \leq 5$ calculated using a least squares regression method, the gradient of which is approximately -8.64.

the functions as, for example

$$K_{1,j}(z) = \sum_{n=1}^{\infty} a_{j,n} \sin(n\pi z), \tag{4.124}$$

from which the coefficients can be calculated using the orthogonality of the basis functions. Now we define

$$\boldsymbol{a}_j^{N_z} = \left(a_{j,1}, a_{j,2}, ..., a_{j,10}\right)^T , \tag{4.125}$$

as the vector of the first 10 coefficients, where each entry is calculated numerically using N_z vertical grid points. This allows us to introduce the stepwise error as

$$E_{K_{1,j}}^{N_z} = \frac{\|\boldsymbol{a}_j^{N_z} - \boldsymbol{a}_j^{N_z-4}\|_{L^2}}{\|\boldsymbol{a}_j^{N_z}\|_{L^2}}, \tag{4.126}$$

with $E_{K_{2,j}}^{N_z}$ and $E_{L_j}^{N_z}$ defined analogously.

Figure 4.9 shows log-log plots of $E_{K_{1,j}}^{N_z}$, $E_{K_{2,j}}^{N_z}$ and $E_{L_j}^{N_z}$ for $j = 1, 2, 3$, which show a clear algebraic decay in the step-wise error. All lines in the plot have a gradient of approximately -6.35 indicating that the errors decay as $E_{K_{1,j}}^{N_z}, E_{K_{2,j}}^{N_z}, E_{L_j}^{N_z} \sim N_z^{-6.35}$. This decay is also observed for values of $j > 3$, and when the number of coefficients in (4.125) is chosen to be greater than 10 (as long as the basis vectors can be resolved on the Chebyshev grid with a high enough accuracy).

4.4 Rossby and inertia-gravity wave dispersion relations in the presence of clouds

The methods of sections 4.3 allow us to calculate the transilient kernels associated with any specified cloud field. This allows us to address the key scientific question: how does the presence of a representative cloud field affect the propagation of atmospheric Rossby and inertia-gravity waves? Here, we calculate the dispersion relations for various wave modes in a mid-latitude β-channel in the presence of the cloud field shown in figure 4.1, and compare the results to the well-known dispersion relations in the absence of clouds ($n = 0$ in equations (4.101–4.104)).

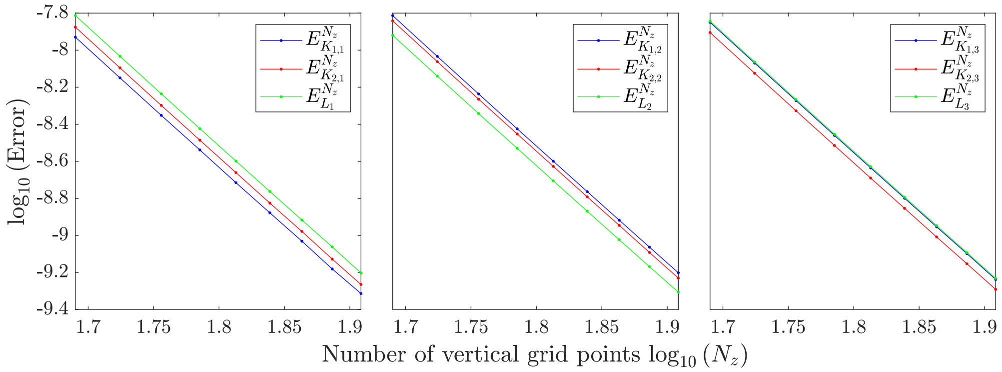

Figure 4.9: Log-log plots of the errors $E_{K_{1,j}}^{N_z}$, $E_{K_{2,j}}^{N_z}$ and $E_{L_j}^{N_z}$ for $j = 1, 2, 3$ (left-right). A least squares regression analysis shows that all curves in each plot may be approximated by a linear function with gradient -6.35 (approximants are omitted from the figures).

We consider a mid-latitude β-channel with sidewalls at $y = \pm 1$, corresponding to a dimensional half-width given by one Rossby radius. The non-dimensional β-parameter is taken to be $\bar{\beta} = 0.1$, since this corresponds to a dimensional value of $\beta \sim 10^{-11}\text{m}^{-1}\text{s}^{-1}$, which is appropriate for the mid-latitude atmosphere.

To pursue this analysis, a representative value of the cloud density $\overline{n}$ must be chosen. A value for the scaled number density $n = 5$ is used here, which in the parameter set-up for the troposphere ($\varepsilon \approx 1/100$) corresponds to a number density of $\overline{n} = 1/20$. This denotes a relatively sparse array of clouds - specifically, one cloud per 20 non-dimensional units of horizontal area so that the average spacing between clouds is $D_{\text{avg}} \sim \sqrt{20} \approx 4.47$. (This is verified in the case where the clouds are arranged using hexagonal packing so that each cloud is equidistant from all of its neighbours, and the distance between adjacent clouds can be calculated to be

$$D_{\text{hex}} = \frac{1}{3^{1/4}} \left(\frac{2}{\overline{n}} \right)^{1/2} \approx 4.81. \tag{4.127}$$

Note that hexagonal packing is used only as an intuitive illustration of cloud density, and that our analysis applies to to randomly distributed cloud fields.) In dimensional terms, this corresponds to the distance between heat sources being approximately 4.5 times the height of the tropopause ($\approx 4.5 \times 10$km). In terms of the β–channel set-up used here, this means that on average, approximately 44 clouds may span its breadth. Importantly, these average spacing distances are sufficiently large to justify the approximation in section 4.1 that individual clouds interact only linearly, since it is clear from figures 4.1 and 4.3–4.5 that the clouds have decayed substantially when $r \sim D_{\text{avg}}/2$.

4.4.1 Numerical solution of the homogenised equations

To begin this analysis, a modal decomposition of the homogenised equations (4.101–4.104) is sought using the expansions (4.35) and (4.36). Particular care must be taken when determining the coefficients in the modal decomposition of the integral terms, the details of which are found in Appendix G. The decomposition into vertical modes of the homogenised equations, after eliminating the variables $\tilde{W}_j$ and $\tilde{B}_j$, is then found to be

$$\partial_t \tilde{\boldsymbol{U}}_j + f\boldsymbol{k} \times \tilde{\boldsymbol{U}}_j + n \sum_{m=0}^{\infty} \left(\tilde{C}_{j,m} - \tilde{D}_{j,m} \right) \tilde{\boldsymbol{U}}_m = -\nabla_{\boldsymbol{x}} \tilde{P}_j, \tag{4.128}$$

$$\partial_t \tilde{P}_j + c_j^2 \nabla_{\boldsymbol{x}} \cdot \tilde{\boldsymbol{U}}_j = n \sum_{m=0}^{\infty} \left(\frac{c_j}{c_m} \right)^2 \tilde{E}_{j,m} \tilde{P}_m, \tag{4.129}$$

for $j = 0, 1, 2, ...$, where the coefficients $\tilde{C}_{j,m}$, $\tilde{D}_{j,m}$ and $\tilde{E}_{j,m}$ are given by

$$\tilde{C}_{j,m} = \int_0^1 \frac{1}{c_j^2} K_{1,m}(z) \Phi_j(z) \, \mathrm{d}z, \quad \tilde{D}_{j,m} = \int_0^1 \frac{1}{c_j^2 c_m^2} K_{2,m}(z) \Phi_j(z) \, \mathrm{d}z, \tag{4.130}$$

$$\tilde{E}_{j,m} = \int_0^1 \frac{1}{c_j^2} L_m(z) \phi_j(z) \, \mathrm{d}z. \tag{4.131}$$

Seeking plane wave solutions of the form

$$\left[\tilde{\boldsymbol{U}}_j(\boldsymbol{x}, t), \tilde{P}_j(\boldsymbol{x}, t) \right] = \left[\hat{\boldsymbol{U}}_j(y), \hat{P}_j(y) \right] \exp\left(-\mathrm{i}\omega t + \mathrm{i}kx \right), \tag{4.132}$$

leads to a coupled, linear system of ODEs given by

$$-\mathrm{i}n\sum_{m=0}^{\infty}\left(\tilde{C}_{j,m}-\tilde{D}_{j,m}\right)\hat{U}_m+\mathrm{i}f\hat{V}_j+k\hat{P}_j=\omega\hat{U}_j, \tag{4.133}$$

$$-\mathrm{i}f\hat{U}_j-\mathrm{i}n\sum_{m=0}^{\infty}\left(\tilde{C}_{j,m}-\tilde{D}_{j,m}\right)\hat{V}_m+\frac{d\hat{P}_j}{dy}=\omega\hat{V}_j, \tag{4.134}$$

$$kc_j^2\hat{U}_j-\mathrm{i}c_j^2\frac{d\hat{V}_j}{dy}+\mathrm{i}n\sum_{m=0}^{\infty}\left(\frac{c_j}{c_m}\right)^2\tilde{E}_{j,m}\hat{P}_m=\omega\hat{P}_j, \tag{4.135}$$

with boundary conditions $\hat{V}_j(\pm 1)=0$ for $j=0,1,2,....$ The dispersion relations are then calculated from the eigenvalues ω of this problem.

The infinite system is solved by truncating the number of vertical modes at a finite number N_s. Here, the calculations are performed for $N_s=10$, which since our method converges rapidly (see figure 4.7), is sufficient to resolve the barotropic, and first two baroclinic modes in the atmosphere. The cross-channel variable y is discretised using a Chebyshev grid with 25 points. In this formulation, the discrete eigenvalue problem takes the form of a diagonal block matrix, with the jth diagonal block resembling that of the usual shallow water system with wave speed c_j; however, additional off-diagonal blocks due to the correlation terms are also present, coupling the modes. The eigenvalues are then calculated using the methods discussed in section 3.2.4.

4.4.2 Dispersion relations

Figures 4.10, 4.11 and 4.12 show the dispersion relations for some of the barotropic and the first two baroclinic wave modes. In each case, the dispersive characteristics of the first three cross-channel modes of the inertia-gravity and Rossby waves are plotted along with the Kelvin wave. The presence of the Kelvin waves in the problem is just an artefact of the fact that we are solving the problem in a channel. The Kelvin wave here relies on the presence of the sidewalls. In the mid-latitude troposphere, there are no equivalent boundaries or waveguides, so they are not physical. We do however plot these solutions for completeness, and for the sake of comparison with the material discussed in chapter 3. The deviation of the calculated dispersion relations from those in the absence of clouds is then easily analysed on a mode-by-mode basis. The results are summarised below.

Firstly, from figure 4.10 we see that all of the barotropic wave modes are almost entirely unaffected by the presence of convection. Mathematically, this arises from the fact that integrating the homogenised equations (4.101–4.104) over the vertical domain causes the terms due to convection to vanish. Small residual effects exist due to the barotropic waves not being exactly homogeneous in the vertical, and are present in the numerical calculations due to the error introduced by the rigid lid/free surface approximations discussed in section 4.2. In summary, the barotropic modes are unaffected by convection to leading order in the rigid lid approximation.

By contrast, from figure 4.11, the first baroclinic mode is seen to be strongly influenced by convection. In particular, the inertia-gravity waves and high-frequency Kelvin waves are relatively unaffected by the clouds, with the dispersion relations deviating only slightly from their counterparts in a cloud-free atmosphere. On the other hand, the Rossby waves and low-frequency Kelvin waves are all seen to be significantly slowed by convection, with some frequencies being reduced by over half at small wave numbers compared to their counterparts in a quiescent atmosphere. Furthermore, the lower order cross-channel modes are more significantly slowed than the higher order modes, especially at smaller zonal wave numbers, indicating that for the first baroclinic mode the cross-channel wave number is of significant importance in determining how waves and clouds interact.

For the second baroclinic mode, it is seen from figure 4.12 that all wave types are noticeably slowed by the presence of clouds. Once again, we see that the waves most affected are the low-frequency Kelvin waves and the Rossby waves. However, in contrast to the first baroclinic mode, it appears that the cross-channel wave number is no longer an important factor in determining the clouds' effect on wave dispersion, since all Rossby modes are slowed by approximately a factor of one half. Thus it appears that the disparate behaviour between different cross-channel wave numbers is a peculiarity of the first baroclinic Rossby wave modes only.

Finally, from figure 4.13 we see that for the first two baroclinic modes

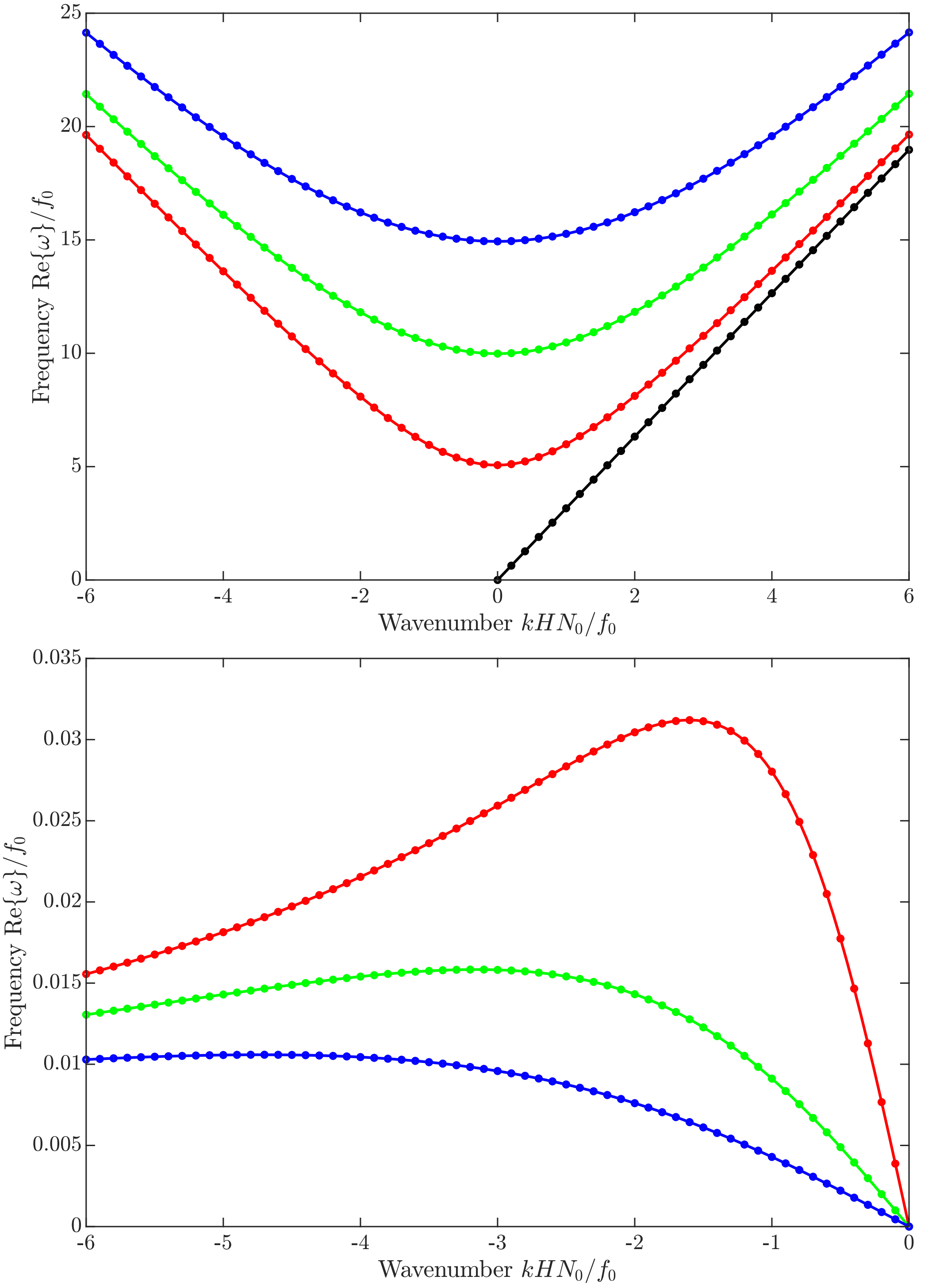

Figure 4.10: Dispersion relations for the barotropic waves. In the top panel the first three cross-channel inertia-gravity modes are shown (red, green, blue) along with the Kelvin wave (black), and in the bottom panel the first three Rossby wave modes are shown. The line plots indicate wave propagation through a cloud-free atmosphere calculated from (4.52) and (4.53) and the circles indicate the corresponding waves when clouds are present, calculated from (4.128) and (4.129). The numerical parameters are $\bar{\beta} = 0.1$ and $n = 5$, and the wave speed of the Kelvin wave in the absence of clouds is $c_0 = 1/\sqrt{\alpha} \approx 3.16$.

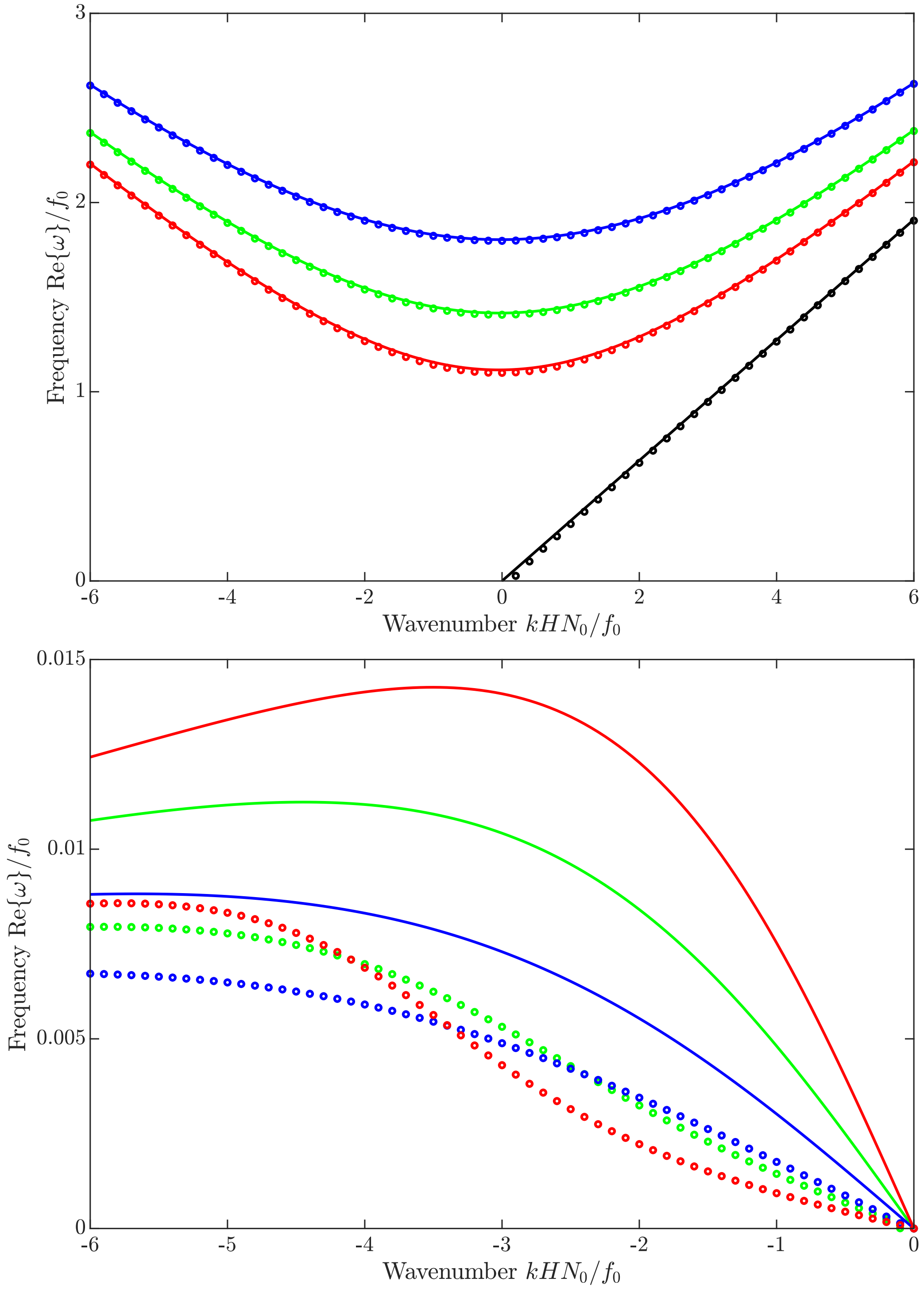

Figure 4.11: Same as figure 4.10 but for the first baroclinic mode. The wave speed of the Kelvin wave in the absence of clouds is $c_1 = 1/\pi \approx 0.32$.

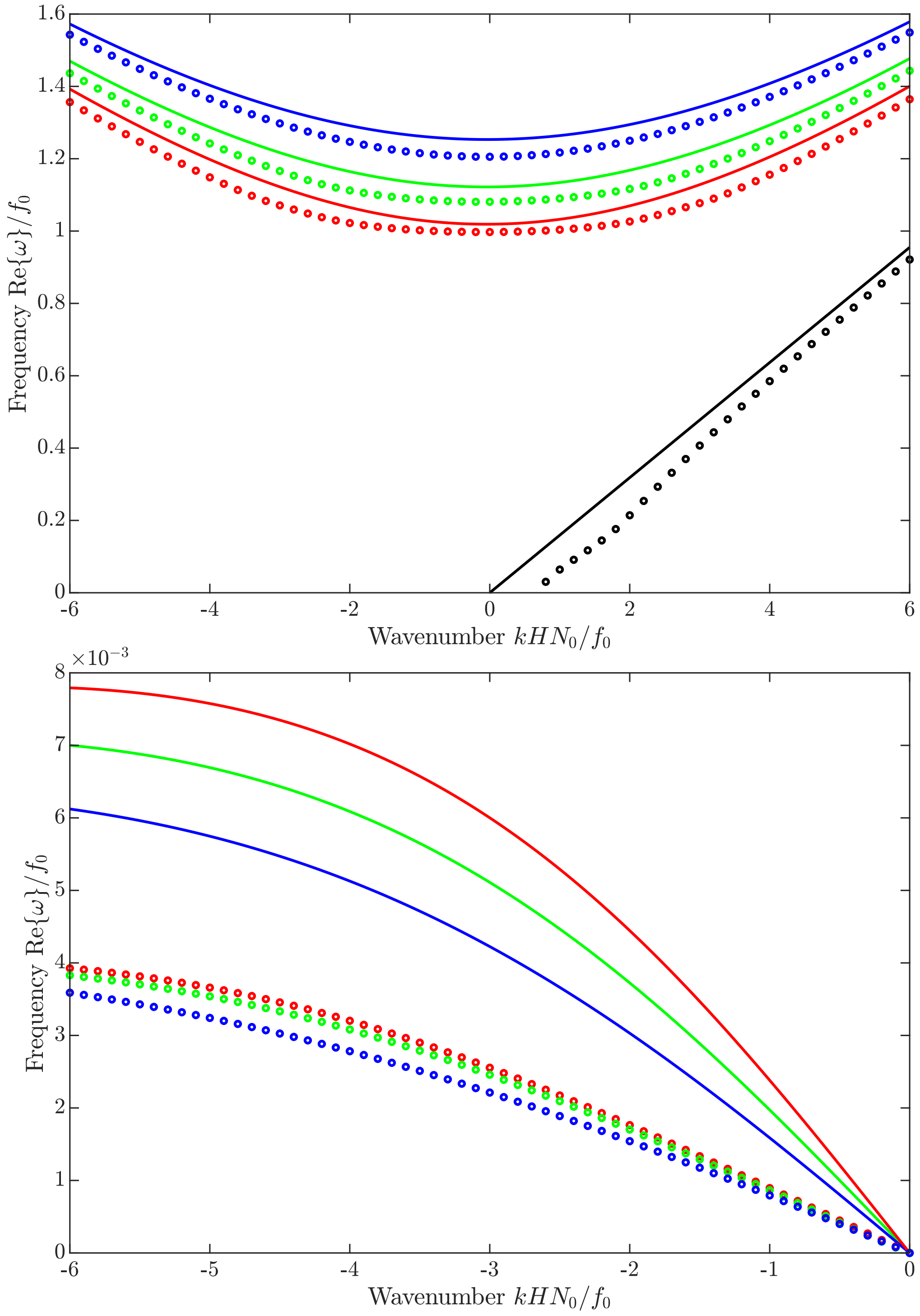

Figure 4.12: Same as figure 4.10 but for the second baroclinic mode. The wave speed of the Kelvin wave in the absence of clouds is $c_2 = 1/2\pi \approx 0.16$.

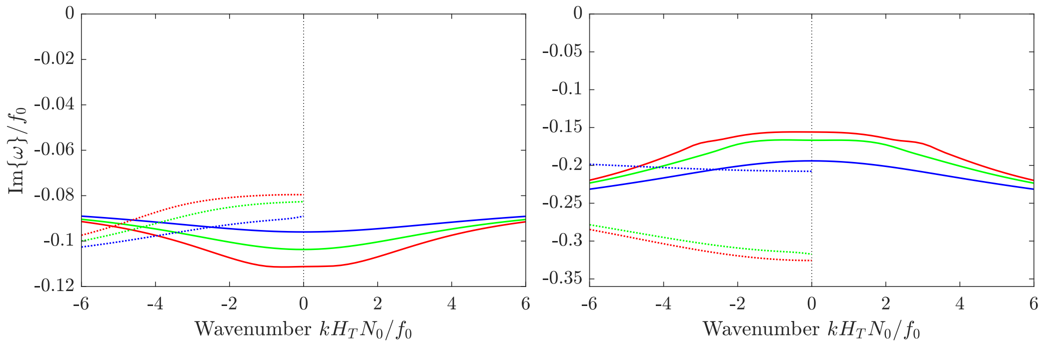

Figure 4.13: Plots of $\mathrm{Im}\{\omega\}$ for the first and second baroclinic modes (left and right panels respectively). The first three cross channel modes (red, green, blue) are shown for the inertia-gravity waves (solid lines) and Rossby waves (dotted lines). Kelvin waves are omitted from this figure.

$\mathrm{Im}\{\omega\} < 0$ for all ω, indicating that the cloud field acts as a damping mechanism which stabilises all wave types. The stabilising effect appears to approximately double between the first and second baroclinic mode, so that the damping primarily affects higher order baroclinic modes. There appears to be no significant discrepancy in the magnitude of the damping between the inertia-gravity and Rossby waves of each baroclinic mode.

4.5 Discussion

In this chapter, the method of homogenisation has been used to derive the homogenised equations (4.101–4.104) governing long wave propagation in the atmosphere in the presence of a convective cloud field. The effect of the clouds on the propagation of barotropic and baroclinic inertia-gravity, Rossby and Kelvin waves are illustrated in figures 4.10–4.12, which show that the clouds act to slow the baroclinic waves - primarily those of low frequency. Figure 4.13 further shows that the cloud field acts as a damping mechanism, causing them to decay over time. As well as giving some insight into how different wave types are affected, the work presented here highlights a number of other interesting features of the interaction between convection and atmospheric waves. In particular, it is seen that small-scale convection acts on long waves through non-local operators involving transilient kernels, and that these operators act to redistribute the large-scale horizontal momentum and buoyancy in the vertical.

Of course, in the interest of simplifying the presentation, our model is highly idealised, and does not constitute a complete picture of the atmospheric dynamics associated with convective processes in the atmosphere. In particular, here, the mechanism driving convection is simply a prescribed diabatic heating profile which forces the dry Boussinesq equations. In order to produce realistic simulations, moist dynamics would also need to be included in the equations through a model describing the bulk cloud microphysics (see e.g. Biello and Majda, 2010). Including a dynamically active moisture field would complicate the solution of the CCP and the CPE, but would leave the basic features of the homogenisation problem largely unchanged. With this in mind, the model discussed here should be viewed as a motivating example of how homogenisation may be used to reduce the multi-scale dynamics associated with convectively coupled waves to a system of averaged equations amenable to numerical computations. Furthermore, when considered alongside the results of chapter 3, the importance of accurately parameterising convection in these models through rigorous asymptotic analyses is emphasised, since it is known that heuristic averaging procedures have the potential to introduce large modelling errors.

Whilst we have discussed only one asymptotic regime here, a number of other interesting and dynamically rich regimes may be studied in an analogous manner. For example, the situation in which clouds are not well-separated would likely introduce a number of other features associated with convectively coupled waves. Studying such a system would require a more detailed asymptotic analysis whereby the homogenisation procedure is carried out to a higher order, and thus is left as a topic for future work. In addition to this, temporal variability within the clouds on time-scales much shorter than those associated with long wave propagation may be considered. Coupling the multi-scale analysis of this section with multiple temporal-scale asymptotics would facilitate the study of such variations. Such a situation would likely lead to dynamics involving resonant behaviour and instabilities, affecting the propagation of long waves governed by the averaged equations at leading order.

Chapter 5

Conclusions

In this thesis, the mathematical theory of homogenisation and its applications in the context of geophysics has been investigated with a particular view towards creating accurate parameterisations of convection in the atmosphere. Beginning with a rigorous asymptotic analysis of the classical wave equation with a rapidly varying local wave speed, as well as a summary of relevant physical concepts, we develop and demonstrate the utility of homogenisation in two novel geophysical contexts. In both cases we conclude that significant modelling errors are possible when small-scale processes are parameterised using averaging procedures based on the mean variables since doing so avoids taking vital sub-grid scale dynamics into account. The original work presented here in chapters 3 and 4 consist of two new multiple-scale systems in a homogeneous and stably stratified atmosphere respectively.

The first of these applies the method of homogenisation to the propagation of long waves in a rotating shallow water system in the presence of small-scale topography, and is based on the paper by Goldsmith and Esler (2021). Naturally, this investigation has many applications in the context of oceanography and wave-topography interactions; however, it is also highly relevant to convective parameterisation in the atmosphere. Not only does it serve as a motivating problem exploring the utility of homogenisation as a tool for building accurate sub-grid scale parameterisations, it also has a direct atmospheric analogue whereby the varying sea depth may be understood as regions of reduced stratification in the atmosphere caused by convection. In this context, the results indicate that the errors introduced into the problem by using parameterisations based on the mean stratification may be large, since they fail to capture vital small-scale dynamics caused by resonant interactions with trapped waves. It should also be noted that the rotating shallow water equations are commonly used in a modified form, known as the ‘thermal rotating shallow water equations’, to explore problems involving horizontal density and temperature gradients, which are particularly pertinent to studying problems associated with convective processes in the atmosphere (Zeitlin, 2018, part III). Applying the method of homogenisation to these equations with a background buoyancy profile consistent with an array of cumulus clouds may provide a more concrete description of how clouds affect the propagation of long waves, and could be a topic of future work in this area. See also the works of Warneford and Dellar (2013); Kurganov et al. (2020, 2021) for applications of these equations to convective systems.

The second novel body of work, given in chapter 4 extends the method of homogenisation to investigate the effects of small-scale, localised heat sources on the propagation of waves though a stratified atmosphere. These sources, assumed to be well spaced, drive a steady, circulatory background flow which mimics that of a convective cloud field. The large-scale equations, after linearisation about the background flow, are then homogenised to give a system of averaged equations describing the propagation of long waves through the atmosphere, and which account for the vertical redistributions of momentum and buoyancy profiles caused by wave-cloud interactions. Such a procedure allows the effects of convection to be rigorously incorporated into the large-scale equations without the application of heuristic averaging procedures, which are known from chapter 3 to be capable of introducing large modelling errors. The model presented here is chosen for its simplicity, applying as it does to an incompressible, dry atmosphere. This allows the main focus to be on the homogenisation procedure, with as few technicalities as possible. However, future work may include generalising the model to include the effects of advected moisture and temporal variations in the clouds, as well as accounting for compressibility. Furthermore, the procedure may also be modified to include the effects of cloud interactions by relaxing the assumption that they are well spaced. Such a generalisation would likely involve significantly more work in order to derive a closed set of averaged equations, but would give a much richer picture of wave dynamics, especially in regions of extreme convective activity.

Appendix A

Quasi-geostrophic limit

In section 3.1.2, it was shown that the quasi-geostrophic averaged equation (3.21) and cell problem (3.22) of Vanneste (2000a,b) emerge from the quasi-geostrophic limit of equations (3.9), (3.10) and (3.11). This demonstrates that the quasi-geostrophic result is independent of the value of ε/b, or in other words, whether the homogenisation procedure, or quasi-geostrophic limit is carried out first, the same set of equations apply. Here, this fact is shown in a more explicit manner.

Beginning with the rSWE, where time and topography height has been rescaled appropriately for the quasi-geostrophic regime using $T = bt$ and $h = 1 - bh_b$, equations (3.1) become

$$\begin{aligned} b\boldsymbol{u}_T + (1 + by)\boldsymbol{k} \times \boldsymbol{u} &= -\nabla\eta, \\ b\eta_T + \nabla \cdot [(1 - bh_b)\boldsymbol{u}] &= 0. \end{aligned} \tag{A.1}$$

In order to analyse the effect of the ratio ε/b, the parameter δ is introduced, and defined by the relation

$$b = \delta\varepsilon, \tag{A.2}$$

so that by expanding the gradient operator via the multi-scale formalism, the equations become

$$\begin{aligned} \delta\varepsilon^2\boldsymbol{u}_T + \varepsilon(1 + \delta\varepsilon y)\boldsymbol{k} \times \boldsymbol{u} &= -\nabla_{\boldsymbol{X}}\eta - \varepsilon\nabla_{\boldsymbol{x}}\eta, \\ \delta\varepsilon^2\eta_T + \nabla_{\boldsymbol{X}} \cdot [(1 - \delta\varepsilon h_b)\boldsymbol{u}] + \varepsilon\nabla_{\boldsymbol{x}} \cdot [(1 - \delta\varepsilon h_b)\boldsymbol{u}] &= 0. \end{aligned} \tag{A.3}$$

The idea is that by treating δ as a quantity of order unity, we can essentially perform the homogenisation process and quasi-geostrophic limits simultaneously, and by examining the limits $\delta \to 0$ and $\delta \to \infty$, determine any dependence of the results on the ordering of ε and b post-hoc. Thus, seeking solutions of the form (3.6), the leading-order balance gives

$$\nabla_{\boldsymbol{X}} \cdot \boldsymbol{u}_0 = 0, \quad \nabla_{\boldsymbol{X}} \eta_0 = 0, \tag{A.4}$$

which leads to

$$\boldsymbol{u}_0(\boldsymbol{X}, \boldsymbol{x}, t) = \boldsymbol{U}(\boldsymbol{x}, t) + \nabla_{\boldsymbol{X}}^{\perp} \psi, \quad \eta_0 = \Pi(\boldsymbol{x}, t), \tag{A.5}$$

where $\boldsymbol{U} = \langle \boldsymbol{u}_0 \rangle$, and $\psi(\boldsymbol{X}, \boldsymbol{x}, t)$ is a scalar function to be determined.

At $O(\varepsilon)$, we have

$$\boldsymbol{k} \times \boldsymbol{u}_0 = -\nabla_{\boldsymbol{X}} \eta_1 - \nabla_{\boldsymbol{x}} \Pi, \tag{A.6}$$

$$\nabla_{\boldsymbol{X}} \cdot \boldsymbol{u}_1 - \delta \nabla_{\boldsymbol{X}} \cdot (h_b \boldsymbol{u}_0) + \nabla_{\boldsymbol{x}} \cdot \boldsymbol{u}_0 = 0. \tag{A.7}$$

Substituting the value of $\boldsymbol{u}_0$ from (A.5) into equation (A.6) gives

$$\boldsymbol{k} \times \boldsymbol{U} - \nabla_{\boldsymbol{X}} \psi = -\nabla_{\boldsymbol{X}} \eta_1 - \nabla_{\boldsymbol{x}} \Pi, \tag{A.8}$$

from which, two things may be determined. Firstly, averaging over the small-scales gives the quasi-geostrophic balance of the leading order variables $\boldsymbol{k} \times \boldsymbol{U} = -\nabla_{\boldsymbol{x}} \Pi$. Secondly, this implies that ψ and η_1 differ only by a constant (a function of the large-scales only), and hence are interchangeable in this context.

Finally, at $O(\varepsilon^2)$, we have

$$\delta \boldsymbol{u}_{0T} + \boldsymbol{k} \times \boldsymbol{u}_1 + \delta y \boldsymbol{k} \times \boldsymbol{u}_0 = -\nabla_{\boldsymbol{X}} \eta_2 - \nabla_{\boldsymbol{x}} \eta_1, \tag{A.9}$$

$$\delta \Pi_T + \nabla_{\boldsymbol{X}} \cdot [\boldsymbol{u}_2 - \delta h_b \boldsymbol{u}_1] + \nabla_{\boldsymbol{x}} \cdot \boldsymbol{u}_1 - \delta \nabla_{\boldsymbol{x}} \cdot (h_b \boldsymbol{u}_0) = 0. \tag{A.10}$$

Applying $\nabla_{\boldsymbol{x}}^{\perp} \cdot$ to equation (A.9), eliminating $\nabla_{\boldsymbol{x}} \cdot \boldsymbol{u}_1$ using (A.10) and then averaging gives the equation

$$\partial_T\left(\nabla_{\boldsymbol{x}}^2\Pi-\Pi\right)+\Pi_x+\nabla_{\boldsymbol{x}}\cdot\left\langle h_b\nabla_{\boldsymbol{X}}^{\perp}\eta_1\right\rangle=0, \tag{A.11}$$

and likewise applying $\nabla_{\boldsymbol{X}}^{\perp}\cdot$ to equation (A.9) and eliminating $\nabla_{\boldsymbol{X}}\cdot\boldsymbol{u}_1$ using (A.7) gives the cell problem

$$\partial_T\nabla_{\boldsymbol{X}}^2\eta_1-\nabla_{\boldsymbol{X}}\eta_1\cdot\nabla_{\boldsymbol{X}}^{\perp}h_b=\nabla_{\boldsymbol{x}}\Pi\cdot\nabla_{\boldsymbol{X}}^{\perp}h_b. \tag{A.12}$$

Importantly, the ratio δ cancels from both sides of equations (A.11) and (A.12) returning the equations derived in section 3.1.2, and thus it is clear that the results do not depend on the parameter ordering of b and ε.

Appendix B

Homogenisation of the rSWE in the presence of Ekman friction

In this section, the analysis of section 2 is repeated for the rSWE with Ekman friction, which in non-dimensional form are

$$\begin{aligned} \boldsymbol{u}_t + (1+by)\boldsymbol{k}\times\boldsymbol{u} &= -\nabla\eta - r\frac{\boldsymbol{u}}{h}, \\ \eta_t + \nabla\cdot(h\boldsymbol{u}) &= 0. \end{aligned} \tag{B.1}$$

The Ekman friction parameter is given by $r = E/f_0H_0$, where E is the dimensional Ekman drag coefficient. Following the procedure of section 3.1, at leading order (3.7) is obtained, and the leading order surface displacement Π and velocity $\boldsymbol{u}_0$ can be defined as in the frictionless case. At next order, multiplying the velocity equation by h and averaging, results in

$$\begin{aligned} \boldsymbol{U}_t + (1+by)\boldsymbol{k}\times\boldsymbol{U} &= -\nabla_{\boldsymbol{x}}\Pi - r\frac{\boldsymbol{U}}{\bar{H}} + \frac{\langle\eta_1\nabla_{\boldsymbol{X}}h\rangle}{H} + r\frac{\left\langle\psi\nabla^{\perp}_{\boldsymbol{X}}\left(\frac{1}{h}\right)\right\rangle}{H}, \\ \Pi_t + \nabla_{\boldsymbol{x}}\cdot(H\boldsymbol{U}) &= 0, \end{aligned} \tag{B.2}$$

where $\bar{H} = \langle h^{-1}\rangle^{-1}$ is the harmonic mean of the depth. Compared with (3.9) there are two extra terms in (B.2), one from the mean drag due to the Ekman friction, and a second correlation term involving ψ.

The cell problems are then obtained following the methodology of section 3.1.

The analogue of the first cell problem (3.10) is obtained by multiplying the $O(\varepsilon)$ equation by h and taking the divergence, giving

$$\begin{aligned}\nabla_{\boldsymbol{X}} \cdot (h \nabla_{\boldsymbol{X}} \eta_1) - (1+by)\nabla^2_{\boldsymbol{X}}\psi - r\nabla_{\boldsymbol{X}}\psi \cdot \nabla^{\perp}_{\boldsymbol{X}}\left(\frac{1}{h}\right) = \\ - \nabla_{\boldsymbol{X}} h \cdot \nabla_{\boldsymbol{x}} \Pi - rH\boldsymbol{U} \cdot \nabla_{\boldsymbol{X}}\left(\frac{1}{h}\right),\end{aligned} \tag{B.3}$$

The second cell problem determining ψ follows from the potential vorticity equation, which at leading order in r is given by

$$\begin{aligned}\nabla_{\boldsymbol{X}} \cdot \left(\frac{\nabla_{\boldsymbol{X}}\psi_t}{h}\right) + r\nabla_{\boldsymbol{X}} \cdot \left(\frac{\nabla_{\boldsymbol{X}}\psi}{h^2}\right) - (1+by)\nabla_{\boldsymbol{X}}\psi \cdot \nabla^{\perp}_{\boldsymbol{X}}\left(\frac{1}{h}\right) = \\ H\left(\boldsymbol{k} \times \boldsymbol{U}_t - (1+by)\boldsymbol{U}\right) \cdot \nabla_{\boldsymbol{X}}\left(\frac{1}{h}\right) + rH\boldsymbol{k} \times \boldsymbol{U} \cdot \nabla_{\boldsymbol{X}}\left(\frac{1}{h^2}\right).\end{aligned} \tag{B.4}$$

Seeking solutions with frequency ω, and exploiting the linearity of (B.3) and (B.4), leads to

$$\begin{aligned}\eta_1 &= \boldsymbol{\Phi} \cdot \nabla_{\boldsymbol{x}}\Pi + rH\boldsymbol{\Lambda} \cdot \boldsymbol{U} + H(1+by)\boldsymbol{\Psi}_{\frac{(1+by)}{\omega}, \frac{r}{\omega}} \cdot \left(\mathrm{i}\frac{1+by}{\omega}\boldsymbol{U} - \boldsymbol{k} \times \boldsymbol{U}\right) \\ &\quad + \mathrm{i}\frac{r^2 H}{\omega}\boldsymbol{\Sigma}_{\frac{(1+by)}{\omega}, \frac{r}{\omega}} \cdot \boldsymbol{k} \times \boldsymbol{U}, \\ \psi &= H\boldsymbol{\Theta}_{\frac{(1+by)}{\omega}, \frac{r}{\omega}} \cdot \left(\mathrm{i}\frac{1+by}{\omega}\boldsymbol{U} - \boldsymbol{k} \times \boldsymbol{U}\right) + \mathrm{i}\frac{rH}{\omega}\boldsymbol{\Upsilon}_{\frac{(1+by)}{\omega}, \frac{r}{\omega}} \cdot \boldsymbol{k} \times \boldsymbol{U},\end{aligned} \tag{B.5}$$

where the vectors $\boldsymbol{\Phi} = (\Phi_1, \Phi_2)^T$, $\boldsymbol{\Lambda} = (\Lambda_1, \Lambda_2)^T$, $\boldsymbol{\Psi}_{\alpha,\delta} = (\Psi_{1,\alpha,\delta}, \Psi_{2,\alpha,\delta})^T$, $\boldsymbol{\Sigma}_{\alpha,\delta} = (\Sigma_{1,\alpha,\delta}, \Sigma_{2,\alpha,\delta})^T$, $\boldsymbol{\Theta}_{\alpha,\delta} = (\Theta_{1,\alpha,\delta}, \Theta_{2,\alpha,\delta})^T$ and $\boldsymbol{\Upsilon}_{\alpha,\delta} = (\Upsilon_{1,\alpha,\delta}, \Upsilon_{2,\alpha,\delta})^T$ are obtained by solving

$$\nabla_{\boldsymbol{X}} \cdot (h\nabla_{\boldsymbol{X}}\Phi_i) = -\partial_{X_i} h, \tag{B.6}$$

$$\nabla_{\boldsymbol{X}} \cdot (h\nabla_{\boldsymbol{X}}\Lambda_i) = -\partial_{X_i}\left(\frac{1}{h}\right), \tag{B.7}$$

and

$$\nabla_{\boldsymbol{X}} \cdot (h\nabla_{\boldsymbol{X}}\Psi_{i,\alpha,\delta}) = \nabla^2_{\boldsymbol{X}}\Theta_{i,\alpha,\delta} + \frac{\delta}{\alpha}\nabla_{\boldsymbol{X}}\Theta_{i,\alpha,\delta} \cdot \nabla^{\perp}_{\boldsymbol{X}}\left(\frac{1}{h}\right), \tag{B.8}$$

$$\nabla_{\boldsymbol{X}} \cdot (h\nabla_{\boldsymbol{X}}\Sigma_{i,\alpha,\delta}) = \frac{\alpha}{\delta}\nabla^2_{\boldsymbol{X}}\Upsilon_{i,\alpha,\delta} + \nabla_{\boldsymbol{X}}\Upsilon_{i,\alpha,\delta} \cdot \nabla^{\perp}_{\boldsymbol{X}}\left(\frac{1}{h}\right), \tag{B.9}$$

where,

$$\begin{aligned}\nabla_{\boldsymbol{X}}\cdot\left(\frac{\nabla_{\boldsymbol{X}}\Theta_{i,\alpha,\delta}}{h}\right)+\mathrm{i}\delta\nabla_{\boldsymbol{X}}\cdot\left(\frac{\nabla_{\boldsymbol{X}}\Theta_{i,\alpha,\delta}}{h^2}\right)&\\ -\mathrm{i}\alpha\nabla_{\boldsymbol{X}}\Theta_{i,\alpha,\delta}\cdot\nabla_{\boldsymbol{X}}^{\perp}\left(\frac{1}{h}\right)&=-\partial_{X_i}\left(\frac{1}{h}\right), \qquad \text{(B.10)}\\ \nabla_{\boldsymbol{X}}\cdot\left(\frac{\nabla_{\boldsymbol{X}}\Upsilon_{i,\alpha,\delta}}{h}\right)+\mathrm{i}\delta\nabla_{\boldsymbol{X}}\cdot\left(\frac{\nabla_{\boldsymbol{X}}\Upsilon_{i,\alpha,\delta}}{h^2}\right)&\\ -\mathrm{i}\alpha\nabla_{\boldsymbol{X}}\Upsilon_{i,\alpha,\delta}\cdot\nabla_{\boldsymbol{X}}^{\perp}\left(\frac{1}{h}\right)&=\partial_{X_i}\left(\frac{1}{h^2}\right), \qquad \text{(B.11)}\end{aligned}$$

and α and δ are complex parameters. The Ekman friction generalisation of (3.18) therefore requires a pair of two-parameter families of equations to be solved in order to determine η_1 and ψ. Substituting η_1 and ψ into equation (B.2), the generalisation of (3.18) is found to be

$$\begin{aligned}&-\mathrm{i}\omega\left(\boldsymbol{\mathcal{I}}+\left(\tfrac{1+by}{\omega}\right)^2\boldsymbol{\mathcal{K}}_{\frac{1+by}{\omega},\frac{r}{\omega}}+\left(\tfrac{1+by}{\omega}\right)\tfrac{r}{\omega}\boldsymbol{\mathcal{M}}_{\frac{1+by}{\omega},\frac{r}{\omega}}\right)\cdot\boldsymbol{U}\\ &+(1+by)\left(\boldsymbol{\mathcal{I}}+\boldsymbol{\mathcal{K}}_{\frac{1+by}{\omega},\frac{r}{\omega}}+\tfrac{r}{1+by}\boldsymbol{\mathcal{M}}_{\frac{1+by}{\omega},\frac{r}{\omega}}-\mathrm{i}\tfrac{r^2}{\omega(1+by)}\boldsymbol{\mathcal{N}}_{\frac{1+by}{\omega},\frac{r}{\omega}}\right)\cdot(\boldsymbol{k}\times\boldsymbol{U})=\\ &\qquad\qquad-(\boldsymbol{\mathcal{I}}+\boldsymbol{\mathcal{D}})\cdot\nabla_{\boldsymbol{x}}\Pi-\frac{r}{\bar{H}}(\boldsymbol{\mathcal{I}}+\boldsymbol{\mathcal{E}})\cdot\boldsymbol{U}, \qquad \text{(B.12)}\end{aligned}$$

with the mass conservation equation for Π unchanged. Here, $\boldsymbol{\mathcal{D}}$ and $\boldsymbol{\mathcal{K}}_{\alpha,\delta}$ are given by (3.17) as before, and the new matrices $\boldsymbol{\mathcal{E}}$, $\boldsymbol{\mathcal{M}}_{\alpha,\delta}$ and $\boldsymbol{\mathcal{N}}_{\alpha,\delta}$ have elements

$$\begin{aligned}(\boldsymbol{\mathcal{E}})_{ij}=-\bar{H}\left\langle\Lambda_j\partial_{X_i}h\right\rangle,\quad(\boldsymbol{\mathcal{M}}_{\alpha,\delta})_{ij}&=\left\langle\Theta_{j,\alpha,\delta}\partial_{X_i}^{\perp}\left(\frac{1}{h}\right)\right\rangle,\\ \text{and}\quad(\boldsymbol{\mathcal{N}}_{\alpha,\delta})_{ij}&=\left\langle\Sigma_{j,\alpha,\delta}\partial_{X_i}h+\Upsilon_{j,\alpha,\delta}\partial_{X_i}^{\perp}\left(\frac{1}{h}\right)\right\rangle.\end{aligned} \qquad \text{(B.13)}$$

As in section 3.1, further simplifications result if it is assumed that the topography has a fourfold symmetry.

In the event that the topography is sparse and the Ekman friction is weak, i.e. the topography area fraction $A \ll 1$ and Ekman friction parameter $r \ll 1$, as in the case of randomly distributed seamounts covered in section 3.3, then (B.2) can be greatly simplified by retaining only those terms which are leading order in A and r.

The result is

$$\begin{aligned} \boldsymbol{U}_t + (1 + by)\boldsymbol{k} \times \boldsymbol{U} &= -\nabla_{\boldsymbol{x}}\Pi - \frac{r}{h_+}\boldsymbol{U} + \frac{\langle \eta_1 \nabla_{\boldsymbol{x}} h \rangle}{h_+}, \\ \Pi_t + \nabla_{\boldsymbol{x}} \cdot (H\boldsymbol{U}) &= 0, \end{aligned} \tag{B.14}$$

and Ekman friction can be neglected when determining η_1, which is given by (3.13). Equations (B.14) are used to calculate the Ekman friction results presented in section 3.3.

Appendix C

Time-dependent solution for the homogenised rSWE

Here the full time-dependent solution to the cell-problem (3.11) is given, and used to obtain the time-dependent generalisation of (3.18), following the approach taken for the quasi-geostrophic system in Vanneste (2000a). Starting from a state of rest, the solution to (3.11) is

$$\psi = H \int_0^t \boldsymbol{R}(\boldsymbol{X}, \boldsymbol{x}, t-\tau) \cdot \left((1+by)\boldsymbol{U}(\boldsymbol{x}, \tau) - \boldsymbol{k} \times \boldsymbol{U}_t(\boldsymbol{x}, \tau)\right) \, \mathrm{d}\tau, \tag{C.1}$$

and hence from equation (3.10), η_1 is given by

$$\begin{aligned} \eta_1 &= \boldsymbol{\Phi}(\boldsymbol{X}, \boldsymbol{x}) \cdot \nabla_{\boldsymbol{x}} \Pi \\ &\quad + H(1+by) \int_0^t \boldsymbol{S}(\boldsymbol{X}, \boldsymbol{x}, t-\tau) \cdot \left((1+by)\boldsymbol{U}(\boldsymbol{x}, \tau) - \boldsymbol{k} \times \boldsymbol{U}_t(\boldsymbol{x}, \tau)\right) \, \mathrm{d}\tau. \end{aligned} \tag{C.2}$$

Here, $\boldsymbol{R}(\boldsymbol{X}, \boldsymbol{x}, t) = (R_1, R_2)^T$ and $\boldsymbol{S}(\boldsymbol{X}, \boldsymbol{x}, t) = (S_1, S_2)^T$ are periodic, zero-mean vectors satisfying the cell problems

$$\nabla_{\boldsymbol{X}} \cdot (h \nabla_{\boldsymbol{X}} S_i) = \nabla^2_{\boldsymbol{X}} R_i, \tag{C.3}$$

$$\nabla_{\boldsymbol{X}} \cdot \left(\frac{\nabla_{\boldsymbol{X}} R_{it}}{h}\right) - (1+by) \nabla_{\boldsymbol{X}} R_i \cdot \nabla^{\perp}_{\boldsymbol{X}} \left(\frac{1}{h}\right) = -\delta(t) \partial_{X_i} \left(\frac{1}{h}\right), \tag{C.4}$$

and the initial conditions

$$\boldsymbol{R}(\boldsymbol{X}, \boldsymbol{x}, 0^-) = \boldsymbol{S}(\boldsymbol{X}, \boldsymbol{x}, 0^-) = 0, \tag{C.5}$$

where $\delta(\cdot)$ is the Dirac delta function. The cell problem (3.14) satisfied by $\boldsymbol{\Phi}$ remains unchanged.

Using the expression (C.2), we can rewrite the momentum equation in (3.9) as an integro-differential equation

$$\begin{aligned}&\boldsymbol{U}_t - (1+by)^2 \int_0^t \boldsymbol{\mathcal{T}}(\boldsymbol{x}, t-\tau) \cdot \boldsymbol{U}(\boldsymbol{x}, \tau)\, \mathrm{d}\tau \\ &+ (1+by)\left(\big(\boldsymbol{\mathcal{I}} + \boldsymbol{\mathcal{T}}(\boldsymbol{x}, 0^+)\big) \cdot \boldsymbol{k} \times \boldsymbol{U} - \int_0^t \boldsymbol{\mathcal{T}}_t(\boldsymbol{x}, t-\tau) \cdot \boldsymbol{k} \times \boldsymbol{U}(\boldsymbol{x}, \tau)\, \mathrm{d}\tau \right) = \\ &\qquad - (\boldsymbol{\mathcal{I}} + \boldsymbol{\mathcal{D}}) \cdot \nabla_{\boldsymbol{x}} \Pi, \end{aligned} \tag{C.6}$$

where $\boldsymbol{\mathcal{T}}$ is the matrix given by

$$\boldsymbol{\mathcal{T}}(\boldsymbol{x}, t) = \begin{pmatrix} \langle S_1 \partial_{X_1} h \rangle & \langle S_2 \partial_{X_1} h \rangle \\ \langle S_1 \partial_{X_2} h \rangle & \langle S_2 \partial_{X_2} h \rangle \end{pmatrix},$$

and $\boldsymbol{\mathcal{D}}$ is defined as before.

Appendix D

Boundary conditions for discontinuous topography

In this section, the boundary conditions relating to the cell problems (3.14) and (3.15) are derived in detail. Suppose that h is discontinuous along a closed curve C in Ω, then it is necessary to determine the boundary conditions on $\boldsymbol{\Phi}$, $\boldsymbol{\Psi}_\alpha$ and G_i along C. Surface displacement must be continuous over C, and hence from (3.13),

$$\Phi_i^+ = \Phi_i^-, \quad \text{and} \quad \Psi_{i,\alpha}^+ = \Psi_{i,\alpha}^-, \tag{D.1}$$

and similarly, since the velocity field must be continuous, (3.8) gives

$$\boldsymbol{n} \cdot \nabla_{\boldsymbol{X}}^{\perp} G_i^+ = \boldsymbol{n} \cdot \nabla_{\boldsymbol{X}}^{\perp} G_i^-, \tag{D.2}$$

where the $+/-$ superscripts indicate the parts of the solution outside / inside the curve C, and $\boldsymbol{n}$ is the unit normal vector on C. The remaining boundary conditions are found from the divergence form of the cell problems

$$\begin{aligned}
\nabla_{\boldsymbol{X}} \cdot (h \nabla_{\boldsymbol{X}} \Phi_i + \boldsymbol{e}_i h) &= 0, \\
\nabla_{\boldsymbol{X}} \cdot (h \nabla_{\boldsymbol{X}} \Psi_{i,\alpha} - \nabla_{\boldsymbol{X}} G_i) &= 0, \\
\nabla_{\boldsymbol{X}} \cdot \left(\frac{\nabla_{\boldsymbol{X}} G_i}{h} + \mathrm{i}\alpha \frac{\nabla_{\boldsymbol{X}}^{\perp} G_i}{h} + \frac{\boldsymbol{e}_i}{h} \right) &= 0,
\end{aligned} \tag{D.3}$$

where $\boldsymbol{e}_i$ is the ith cartesian basis vector. The arguments of the divergence operator in each case must be continuous across C, i.e.

$$\begin{aligned} \left[(h\nabla_{\boldsymbol{X}}\Phi_i + \boldsymbol{e}_i h)\cdot\boldsymbol{n}\right]_-^+ &= 0, \\ \left[(h\nabla_{\boldsymbol{X}}\Psi_{i,\alpha} - \nabla_{\boldsymbol{X}}G_i)\cdot\boldsymbol{n}\right]_-^+ &= 0, \\ \left[\left(\frac{\nabla_{\boldsymbol{X}}G_i}{h} + \mathrm{i}\alpha\frac{\nabla_{\boldsymbol{X}}^{\perp}G_i}{h} + \frac{\boldsymbol{e}_i}{h}\right)\cdot\boldsymbol{n}\right]_-^+ &= 0. \end{aligned} \tag{D.4}$$

In the case of the cylindrical topography (3.28), in which C is a circle centred at the origin with radius R, only the $i = 1$ problem need be considered due to rotational symmetry. Dropping the i subscript, and focussing on the $i = 1$ problem, which is sufficient to obtain $K_1(\alpha)$ and $K_2(\alpha)$, the boundary conditions (D.4) become (3.33) given in the main text.

Appendix E

The multipole expansion method

Here the multipole method used to solve the cell problems (3.29-3.30) and (3.32-3.33) in section 3.2 is described. The method closely follows that of Godin (2013) (see also Balagurov and Kashin, 2001).

First, $G^{\pm}$ and $\Psi_{\alpha}^{\pm}$ in (3.32-3.33) are expanded into their real and imaginary parts $G^{\pm} = G_R^{\pm} + \mathrm{i}G_I^{\pm}$, and $\Psi_{\alpha}^{\pm} = \Psi_{\alpha,R}^{\pm} + \mathrm{i}\Psi_{\alpha,I}^{\pm}$. Next, all real dependent variables are expanded in a complex power series, for example

$$\Phi^{-} = \mathrm{Re}\left\{\sum_{m=0}^{\infty} W_m z^m\right\}, \qquad \text{(E.1a)} \qquad \Phi^{+} = \mathrm{Re}\left\{\sum_{m=1}^{\infty} Y_m r_m(z)\right\}, \qquad \text{(E.1b)}$$

where $z = X_1 + \mathrm{i}X_2$ is the usual complex variable defined on Ω (recall that the $+$ and $-$ superscripts refer to solutions in $|z| > R$ and $|z| < R$ respectively). Expansions for $\Psi_{\alpha,R}^{-}$, $\Psi_{\alpha,I}^{-}$, G_R^{-} and G_I^{-} have the same form as (E.1a), with coefficients A_m, B_m, F_m, G_m respectively, whereas $\Psi_{\alpha,R}^{+}$, $\Psi_{\alpha,I}^{+}$, G_R^{+} and G_I^{+} have the form of (E.1b) with coefficients C_m, D_m, M_m, P_m. In general all of the coefficients are complex, except for $m = 0$, when they must be real. The sequence of functions $\{r_m(z)\}$ is given by

$$\begin{aligned} r_1(z) &= \zeta(z;\Lambda) - \zeta(\pi;\Lambda)\,\frac{z}{\pi}, \\ r_m(z) &= \frac{(-1)^{m-1}}{(m-1)!}\,\frac{\mathrm{d}^{m-1}}{\mathrm{d}z^{m-1}}\,r_1(z), \qquad (m > 1) \end{aligned}$$

with $r_0(z)$ defined by $r_0'(z) = r_1(z)$. Here, $\zeta(z;\Lambda)$ is the Weierstrass zeta function associated with the lattice $\Lambda = \{z_{\boldsymbol{k}} = 2\pi(k_x + \mathrm{i}k_y) \,|\, \boldsymbol{k} = (k_x, k_y) \in \mathbb{Z}^2\}$. The advantage of expanding in the functions $\{r_m(z)\}$ is that use can be made of the Laurent expansion of the Weierstrass zeta functions, which for the rectangular lattice Λ can be written

$$\zeta(z;\Lambda) = \frac{1}{z} - \sum_{j=1}^{\infty} q_{4j}\, z^{4j-1},$$

where

$$q_j = \sum_{z_{\boldsymbol{k}} \in \Lambda^*} \frac{1}{z_{\boldsymbol{k}}^j},$$

with the sum over the lattice $\Lambda^* = \Lambda \backslash \{0\}$. The sequence $\{q_{4j},\ j = 2, 3, ...\}$ can be calculated using the recurrence relation

$$q_{4j} = \frac{3}{(4j-1)^2(2j-3)} \sum_{l=2}^{2j-2} (4j-2l-1)(2l-1) q_{2l} q_{4j-2l}.$$

From the above results, and the fact that $\zeta(\pi;\Lambda) = \frac{1}{4}$ (Balagurov and Kashin, 2001), it follows that

$$\begin{aligned} r_0(z) &= \log z - \frac{z^2}{8\pi} - \sum_{m=1}^{\infty} \frac{q_{4m} z^{4m}}{4m}, \\ r_1(z) &= \frac{1}{z} - \frac{z}{4\pi} - \sum_{m=1}^{\infty} q_{4m} z^{4m-1}, \\ r_2(z) &= \frac{1}{z^2} + \frac{1}{4\pi} + \sum_{m=1}^{\infty} (4m-1) q_{4m} z^{4m-2}, \\ r_m(z) &= \frac{1}{z^m} + \sum_{j=[(m+3)/4]}^{\infty} (-1)^m \binom{4j-1}{m-1} q_{4j} z^{4j-m}, \qquad (m \geq 3) \end{aligned}$$

from which the outer solutions can be expanded as (for example)

$$\Phi^+ = \mathrm{Re}\left(Y_0 \log z + \sum_{m=1}^{\infty} \frac{Y_m}{z^m} + \sum_{m=0}^{\infty} \sum_{j=0}^{\infty} Y_j E_{jm} z^m \right),$$

where

$$E_{jm} = \begin{cases} 0 & j = m = 0 \\ -\dfrac{\delta_{m2}}{8\pi} - \dfrac{Q_m}{m} & j = 0 \quad m \geq 1 \\ -\dfrac{\delta_{j1}\delta_{m1}}{4\pi} + \dfrac{\delta_{j2}\delta_{m0}}{4\pi} + (-1)^j \dbinom{m+j-1}{j-1} Q_{j+m} & j \geq 1 \end{cases}$$

where δ_{jk} is the Kronecker delta, and $Q_m = q_m$ if $m = 4k$ for integer k and is zero otherwise.

The boundary conditions for the two cell problems are (3.30) and (3.33) respectively. It is helpful to decompose boundary condition (3.33) into real and imaginary parts

$$\begin{aligned} \Psi^+_{\alpha,R} &= \Psi^-_{\alpha,R}, \\ \Psi^+_{\alpha,I} &= \Psi^-_{\alpha,I}, \\ \partial_\theta G^+_R &= \partial_\theta G^-_R, \\ \partial_\theta G^+_I &= \partial_\theta G^-_I, \\ h_+ \partial_\rho \Psi^+_{\alpha,R} - h_- \partial_\rho \Psi^-_{\alpha,R} &= \partial_\rho G^+_R - \partial_\rho G^-_R, \\ h_+ \partial_\rho \Psi^+_{\alpha,I} - h_- \partial_\rho \Psi^-_{\alpha,I} &= \partial_\rho G^+_I - \partial_\rho G^-_I, \\ \frac{\partial_\rho G^+_R}{h_+} - \frac{\partial_\rho G^-_R}{h_-} + \frac{\alpha}{R}\left(\frac{\partial_\theta G^+_I}{h_+} - \frac{\partial_\theta G^-_I}{h_-}\right) &= -\left(\frac{1}{h_+} - \frac{1}{h_-}\right)\cos\theta, \\ \frac{\partial_\rho G^+_I}{h_+} - \frac{\partial_\rho G^-_I}{h_-} - \frac{\alpha}{R}\left(\frac{\partial_\theta G^+_R}{h_+} - \frac{\partial_\theta G^-_R}{h_-}\right) &= 0, \end{aligned} \tag{E.2}$$

on $|\boldsymbol{X}| = R$. To apply the conditions (3.30) and (E.2), note that $z = R\mathrm{e}^{\mathrm{i}\theta}$ on the boundary. It is helpful to write $w_m = R^m \mathrm{Re}\,(W_m)$, $y_m = R^{-m}\mathrm{Re}\,(Y_m)$, $a_m = R^m\mathrm{Re}\,(A_m)$, $c_m = R^{-m}\mathrm{Re}\,(C_m)$, $b_m = -R^m\mathrm{Im}\,(B_m)$, $d_m = R^{-m}\mathrm{Im}\,(D_m)$, $f_m = R^m\mathrm{Re}\,(F_m)$, $m_m = R^{-m}\mathrm{Re}\,(M_m)$, $g_m = -R^m\mathrm{Im}\,(G_m)$, $p_m = R^{-m}\mathrm{Im}\,(P_m)$, and it follows that, for $m > 1$

$$\begin{gathered}
w_m = y_m + \sum_{j=0}^{\infty} R^{m+j} y_j E_{jm}, \\
a_m = c_m + \sum_{j=0}^{\infty} R^{m+j} c_j E_{jm}, \qquad b_m = d_m - \sum_{j=0}^{\infty} R^{m+j} d_j E_{jm}, \\
f_m = m_m + \sum_{j=0}^{\infty} R^{m+j} m_j E_{jm}, \qquad g_m = p_m - \sum_{j=0}^{\infty} R^{m+j} p_j E_{jm}.
\end{gathered} \tag{E.3}$$

and that

$$\begin{gathered}
y_m - \gamma \sum_{j=0}^{\infty} R^{m+j} y_j E_{jm} = R\gamma\delta_{m1}, \\
c_m - \gamma \sum_{j=0}^{\infty} R^{m+j} c_j E_{jm} = \frac{2}{h_+ + h_-} m_m, \quad d_m + \gamma \sum_{j=0}^{\infty} R^{m+j} d_j E_{jm} = \frac{2}{h_+ + h_-} p_m, \\
m_m + \gamma \sum_{j=0}^{\infty} R^{m+j} m_j E_{jm} + \gamma\alpha \left(p_m - \sum_{j=0}^{\infty} R^{m+j} p_j E_{jm} \right) = -R\gamma\delta_{m1}, \\
p_m - \gamma \sum_{j=0}^{\infty} R^{m+j} p_j E_{jm} + \gamma\alpha \left(m_m + \sum_{j=0}^{\infty} R^{m+j} m_j E_{jm} \right) = 0,
\end{gathered} \tag{E.4}$$

where $\gamma = (h_+ - h_-)/(h_+ + h_-)$. Now, by truncating the series at some finite value, say $m = j = M$, a linear system is obtained, which can be written in matrix form for the first cell problem (3.29-3.30) as

$$\boldsymbol{w} = \left(\boldsymbol{I} + \boldsymbol{D}\boldsymbol{E}^T\boldsymbol{D}\right)\boldsymbol{y}, \qquad \left(\boldsymbol{I} - \gamma\boldsymbol{D}\boldsymbol{E}^T\boldsymbol{D}\right)\boldsymbol{y} = \gamma R\boldsymbol{f}, \tag{E.5}$$

and for the second cell problem (3.32-3.33) as

$$\begin{gathered}
\boldsymbol{a} = \left(\boldsymbol{I} + \boldsymbol{D}\boldsymbol{E}^T\boldsymbol{D}\right)\boldsymbol{c}, \qquad \boldsymbol{m} = \tfrac{1}{2}\left(h_+ + h_-\right)\left(\boldsymbol{I} - \gamma\boldsymbol{D}\boldsymbol{E}^T\boldsymbol{D}\right)\boldsymbol{c}, \\
\boldsymbol{b} = \left(\boldsymbol{I} - \boldsymbol{D}\boldsymbol{E}^T\boldsymbol{D}\right)\boldsymbol{d}, \qquad \boldsymbol{p} = \tfrac{1}{2}\left(h_+ + h_-\right)\left(\boldsymbol{I} + \gamma\boldsymbol{D}\boldsymbol{E}^T\boldsymbol{D}\right)\boldsymbol{d}, \\
\left(\boldsymbol{I} + \gamma\boldsymbol{D}\boldsymbol{E}^T\boldsymbol{D}\right)\boldsymbol{m} + \alpha\gamma\left(\boldsymbol{I} - \boldsymbol{D}\boldsymbol{E}^T\boldsymbol{D}\right)\boldsymbol{p} = -\gamma R\boldsymbol{f}, \\
\left(\boldsymbol{I} - \gamma\boldsymbol{D}\boldsymbol{E}^T\boldsymbol{D}\right)\boldsymbol{p} + \alpha\gamma\left(\boldsymbol{I} + \boldsymbol{D}\boldsymbol{E}^T\boldsymbol{D}\right)\boldsymbol{m} = 0,
\end{gathered} \tag{E.6}$$

where $\boldsymbol{f} = (1, 0, ..., 0)^T$, $\boldsymbol{w} = (w_1, w_2, ..., w_M)^T$ (the remaining vectors are defined analogously), $\boldsymbol{D}$ =diag$(R, R^2, ..., R^M)$, and $\boldsymbol{E}$ has components E_{jm} given above.

E.1 Effective depth: small R asymptotics

Now consider the equations pertaining to the effective depth of the fluid, namely (E.5) in the regime $R \ll 1$. It is straightforward in principle to solve the system to any order in R. For example, retaining terms up to R^9 gives

$$\begin{aligned} y_1 - \gamma\left(-\frac{R^2}{4\pi}y_1 - 3R^4 q_4 y_3 - 7R^8 q_8 y_7\right) &= \gamma R \\ y_3 - \gamma(-R^4 q_4 y_1 - 35R^8 q_8 y_5) &= 0 \\ y_5 - \gamma(-21R^8 q_8 y_3) &= 0 \\ y_7 - \gamma(-R^8 q_8 y_1) &= 0 \end{aligned}$$

from which the following sequence of Padé approximants for y_1 and w_1 are easily found. Retaining only terms up to order R, gives the 'zeroth'-order approximations for y_1 and w_1,

$$y_1^{(0)} = w_1^{(0)} = \gamma R,$$

and likewise, retaining terms involving R^3 and R^5, give

$$y_1^{(1)} = \frac{\gamma R}{1 + \gamma R^2/4\pi} + O(R^9), \qquad w_1^{(1)} = \frac{\gamma R(1 - R^2/4\pi)}{1 + \gamma R^2/4\pi} + O(R^9),$$

and

$$\begin{aligned} y_1^{(2)} &= \frac{\gamma R}{1 + \gamma R^2/4\pi - 3\gamma q_4^2 R^8} + O(R^{17}), \\ w_1^{(2)} &= \frac{\gamma R(1 - R^2/4\pi + 3\gamma q_4^2 R^8)}{1 + \gamma R^2/4\pi - 3\gamma^2 q_4^2 R^8} + O(R^{17}). \end{aligned}$$

It is easy to see how this process could be extended up to any order, however, it is also notable that due to the extremely fast convergence rate for small R (see e.g. figure 3.3), that for the analytical purposes of section 3.2, the second-order approximant is sufficient. It is also an easy process to implement numerically to find Padé approximants at much higher orders, which give results up to machine precision (here, the 24th approximant is considered the ‘exact’ solution). The effective depth is then given by

$$H_{\text{eff}}^{(i)} = H - \frac{R\left(h_+ - h_-\right)w_1^{(i)}}{4\pi}, \tag{E.7}$$

which leads directly to the results given in (3.31).

Exactly the same procedure may be followed using equations (E.6) to determine the Padé approximants for a_1 and b_1 which are the coefficients needed to calculate the topographic resonance functions $K_1(\alpha)$ and $K_2(\alpha)$. Omitting the details, the leading three Padé approximants to $K_1(\alpha)$ are

$$\begin{aligned}
K_1^{(0)}(\alpha) &= -2\gamma^2 A\left(\frac{1}{1-\alpha^2\gamma^2}\right),\\
K_1^{(1)}(\alpha) &= -2\gamma^2 A\left(\frac{1-A}{1-\alpha^2\gamma^2+\gamma^2A^2\left(\alpha^2-1\right)}\right),\\
K_1^{(2)}(\alpha) &= -2\gamma^2 A\left(\frac{\left(1-A\right)\left(1-\alpha^2\gamma^2\right)-g_4\gamma^2A^4\left(1-\alpha^2\right)}{\left(1-\alpha^2\gamma^2+g_4\gamma^2A^4\left(\alpha^2-1\right)\right)^2+\gamma^2A^2\left(\alpha^2-1\right)\left(1-\alpha^2\gamma^2\right)}\right),
\end{aligned} \tag{E.8}$$

where $g_4 = 3q_4^2(4\pi)^4 \approx 0.305$. Similarly for $K_2(\alpha)$

$$\begin{aligned}
K_2^{(0)}(\alpha) &= 2\alpha\gamma^3 A\left(\frac{1}{1-\alpha^2\gamma^2}\right),\\
K_2^{(1)}(\alpha) &= \frac{2\alpha\gamma^3 A}{1-\gamma A}\left(\frac{1-A^2}{1-\alpha^2\gamma^2+\gamma^2A^2\left(\alpha^2-1\right)}\right),\\
K_2^{(2)}(\alpha) &= \frac{2\alpha\gamma^3 A}{1-\gamma A-g_4\gamma^2A^4}\\
&\times\left(\frac{\left(1-A^2-g_4A^4\right)\left(1-\alpha^2\gamma^2\right)+g_4\gamma A^4\left(\left(\gamma^2-1\right)A+\gamma(1-g_4A^4)(\alpha^2-1)\right)}{\left(1-\alpha^2\gamma^2+g_4\gamma^2A^4\left(\alpha^2-1\right)\right)^2+\gamma^2A^2\left(\alpha^2-1\right)\left(1-\alpha^2\gamma^2\right)}\right).
\end{aligned} \tag{E.9}$$

Finally, it is also helpful to give the results for the quasi-geostrophic analogue of

$K_1(\alpha)$, obtained from the solution of (3.24) by the same method. These are

$$\begin{aligned}
\tilde{K}^{(0)}\left(\alpha\right) &= -\tfrac{1}{2}h_b^2 A\left(\frac{1}{1-\frac{1}{4}\alpha^2 h_b^2}\right), \\
\tilde{K}^{(1)}\left(\alpha\right) &= -\tfrac{1}{2}h_b^2 A\left(\frac{1-A}{1-\frac{1}{4}\alpha^2 h_b^2(1-A)}\right), \\
\tilde{K}^{(2)}\left(\alpha\right) &= -\tfrac{1}{2}h_b^2 A\left(\frac{(1-A)\left(1-\frac{1}{4}h_b^2\alpha^2\right)+\frac{1}{4}g_4 A^4 h_b^2\alpha^2}{\left(1-\frac{1}{4}\alpha^2 h_b^2+\frac{1}{4}g_4 A^4 h_b^2\alpha^2\right)^2+\frac{1}{4}\alpha^2 h_b^2 A^2\left(1-\frac{1}{4}\alpha^2 h_b^2\right)}\right).
\end{aligned} \tag{E.10}$$

Appendix F

Vertical mode decomposition for $n = 0$

Here, we derive the Sturm-Liouville problems used in section 4.2, from the system of equations (4.29–4.32), subject to the boundary conditions (4.33) and (4.34). We are able to eliminate W and B from equations (4.29–4.32) by integration of the hydrostatic and continuity equations. This gives the relations

$$P(\boldsymbol{x}, z, t) = P(\boldsymbol{x}, 1, t) + \int_1^z B(\boldsymbol{x}, z', t)\, \mathrm{d}z', \tag{F.1}$$

$$W(\boldsymbol{x}, z, t) = -\int_0^z \nabla \cdot \boldsymbol{U}(\boldsymbol{x}, z'', t)\, \mathrm{d}z''. \tag{F.2}$$

Differentiating the first of these with respect to time, and substituting in the free surface boundary condition and the buoyancy equation (4.32) gives

$$\frac{\partial P}{\partial t} = \alpha^{-1} W(\boldsymbol{x}, 1, t) + \int_z^1 N^2(z') W(\boldsymbol{x}, z', t)\, \mathrm{d}z'. \tag{F.3}$$

We can then eliminate W to find

$$\frac{\partial P}{\partial t} = -\mathcal{I} \nabla \cdot \boldsymbol{U} \tag{F.4}$$

where the integral operator $\mathcal{I}$ is given by

$$\mathcal{I} = \frac{1}{\alpha} \int_0^1 \mathrm{d}z'' + \int_z^1 \mathrm{d}z' N^2(z') \int_0^{z'} \mathrm{d}z''. \tag{F.5}$$

Assuming a separable ansatz for $\boldsymbol{U}$ and P of the form

$$[\boldsymbol{U}(\boldsymbol{x}, z, t), P(\boldsymbol{x}, z, t)] = \left[\tilde{\boldsymbol{U}}(\boldsymbol{x}, t), \tilde{P}(\boldsymbol{x}, t)\right] \phi(z), \tag{F.6}$$

equation (F.5) yields

$$\frac{\partial \tilde{P}}{\partial t} + \lambda \nabla \cdot \tilde{\boldsymbol{U}} = 0, \tag{F.7}$$

$$\mathcal{I}\phi = \lambda\phi, \tag{F.8}$$

where λ is some separation constant. Applying $d/dz(N^{-2}d/dz)$ to (F.8) yields the ODE

$$\frac{d}{dz}\left(\frac{1}{N^2}\frac{d\phi}{dz}\right) = -\frac{1}{\lambda}\phi. \tag{F.9}$$

The first boundary condition is then found by differentiating (F.8) once with respect to z and evaluating the result at $z = 0$, from which it is found that

$$\frac{d\phi}{dz} = 0 \quad \text{at} \quad z = 0. \tag{F.10}$$

A second condition at the free surface is found by integrating (F.9) over the entire vertical extent of the fluid to get

$$\frac{1}{N^2(1)}\frac{d\phi}{dz}(1) - \frac{1}{N^2(0)}\frac{d\phi}{dz}(0) = -\frac{1}{\lambda}\int_0^1 \phi(z')\,\mathrm{d}z', \tag{F.11}$$

and observing from (F.8) that the right-hand side is equal to $-\alpha\phi(1)$. Thus we have

$$\frac{d\phi}{dz} + \alpha N^2\phi = 0 \quad \text{at} \quad z = 1. \tag{F.12}$$

Finally, an observation may be made about the constant λ by multiplying (F.9) by ϕ and integrating by parts. This gives

$$\int_0^1 \frac{1}{N^2}\left(\frac{d\phi}{dz}\right)^2 - \frac{1}{\lambda}\phi^2\,\mathrm{d}z = -\frac{\phi(1)^2}{\alpha}, \tag{F.13}$$

which by comparison of signs between the left- and right-hand side implies that the integrand may not be positive across the whole vertical domain, and consequently $\lambda \equiv c^2 > 0$ must be positive.

Equation (F.9) together with the boundary conditions (F.10) and (F.12) constitute a Sturm-Liouville problem, for which solutions $\phi = \phi_n(z)$ exist only for a discrete, ordered set of eigenvalues c_n^2, for $n = 0, 1, 2, ...$ The problem does not in general have analytic solutions, however when N^2 is taken to be a constant (as is done in the main text) the problem simplifies greatly. The full Sturm-Liouville problem with $N^2 = N^2(z)$ is given by

$$\frac{d}{dz}\left(\frac{1}{N^2}\frac{d\phi_n}{dz}\right) + \frac{1}{c_n^2}\phi_n = 0, \tag{F.14}$$

$$\frac{d\phi_n}{dz} = 0, \quad \text{on} \quad z = 0, \tag{F.15}$$

$$\frac{d\phi_n}{dz} + \alpha N^2 \phi_n = 0, \quad \text{on} \quad z = 1. \tag{F.16}$$

In order to complete our understanding of the Boussinesq system in this regime, it is helpful to understand how the vertical velocity W and buoyancy B act in this regime. Assuming the separable ansatz

$$[W(\boldsymbol{x}, z, t), B(\boldsymbol{x}, z, t)] = \left[\tilde{W}(\boldsymbol{x}, t), N^2(z)\tilde{B}(\boldsymbol{x}, t)\right]\Phi(z), \tag{F.17}$$

it is readily seen from the continuity equation (4.31) that $\Phi = \Phi_n(z)$ also has a modal structure satisfying

$$\frac{d\Phi_n}{dz} = \phi_n, \quad \text{for} \quad n = 0, 1, 2..., \tag{F.18}$$

with the boundary conditions $\Phi_n(0) = 0$. Integrating equation (F.14) from 0 to z then yields the Sturm-Liouville problem for Φ_n given by

$$\frac{d^2\Phi_n}{dz^2} + \frac{N^2}{c_n^2}\Phi_n = 0, \tag{F.19}$$

$$\Phi_n = 0, \quad \text{on} \quad z = 0, \tag{F.20}$$

$$\alpha\frac{d\Phi_n}{dz} = \frac{1}{c_n^2}\Phi_n, \quad \text{on} \quad z = 1. \tag{F.21}$$

Finally, by substituting (F.6) into (4.29) and (F.7), it is seen that the horizontal structure of each mode in the decomposition satisfies

$$\frac{\partial \tilde{\boldsymbol{U}}_n}{\partial t} + f\boldsymbol{k} \times \tilde{\boldsymbol{U}}_n = -\nabla \tilde{P}_n, \tag{F.22}$$

$$\frac{\partial \tilde{P}_n}{\partial t} + c_n^2 \nabla \cdot \tilde{\boldsymbol{U}}_n = 0. \tag{F.23}$$

That is, the horizontal structure of the nth mode obeys a shallow water equation with *equivalent wave speed* given by c_n.

Appendix G

Vertical mode decomposition of the integral terms in (4.101–4.104)

Here, we provide explicit calculations determining the vertical mode decompositions of the integral terms in the homogenised equations (4.101–4.104). Before proceeding, let us emphasise the importance of applying the convention discussed in section 4.2.2 accurately. That is, we use the free surface integral property and boundary conditions when manipulating the basis functions, and use the rigid lid approximations for the basis functions afterwards.

Let us recall the modal expansions of $\boldsymbol{U}$ and B, which are

$$\boldsymbol{U} = \sum_{j=0}^{\infty} \boldsymbol{U}_j \phi_j, \qquad B = \sum_{j=0}^{\infty} B_j \Phi_j, \tag{G.1}$$

from which see that

$$\partial_z \boldsymbol{U} = -\sum_{j=0}^{\infty} \frac{1}{c_j^2} \boldsymbol{U}_j \Phi_j, \qquad \partial_z B = \sum_{j=0}^{\infty} B_j \phi_j, \tag{G.2}$$

where we have used (4.37) and (4.41). Note that in contrast to (4.76) and (4.77), we opt to keep the coefficients in terms of $\boldsymbol{U}_j$ and B_j.

Next, using the definitions of the non-local operators (4.3.3), the modal expansions of the transilient kernels (4.114–4.116), and the integral properties (4.45) and

(4.51), we calculate

$$\mathcal{K}_1\boldsymbol{U} = \sum_{j=0}^{\infty} K_{1,j}(z)\boldsymbol{U}_j, \tag{G.3}$$

$$\mathcal{K}_2\partial_z\boldsymbol{U} = \sum_{j=0}^{\infty} \frac{1}{c_j^2}K_{2,j}(z)\left[\boldsymbol{U}_j + \frac{1}{\alpha}\partial_z\boldsymbol{U}(1)\Phi_j(1)\right], \tag{G.4}$$

$$\mathcal{L}\partial_z B = -\sum_{j=0}^{\infty} L_j(z)B_j. \tag{G.5}$$

Now we are able to project the integral terms in the homogenised equations (4.101–4.104) onto the vertical basis functions. Beginning with the term involving $\mathcal{K}_1$ which, using the integral condition (4.45) we project onto the ϕ_j basis, we find

$$\partial_z\left(\mathcal{K}_1\boldsymbol{U}\right) = \sum_{j=0}^{\infty}\left[\int_0^1 \partial_z\left(\mathcal{K}_1\boldsymbol{U}\right)\phi_j \,\mathrm{d}z\right]\phi_j(z), \tag{G.6}$$

$$= \sum_{j=0}^{\infty}\left[\mathcal{K}_1\boldsymbol{U}\phi_j\Big|_{z=1} - \mathcal{K}_1\boldsymbol{U}\phi_j\Big|_{z=0} + \frac{1}{c_j^2}\int_0^1 \mathcal{K}_1\boldsymbol{U}\Phi_j \,\mathrm{d}z\right]\phi_j(z), \tag{G.7}$$

$$= \sum_{j=0}^{\infty}\sum_{m=0}^{\infty}\left[\frac{1}{c_j^2}\int_0^1 K_{1,m}\Phi_j \,\mathrm{d}z\right]\boldsymbol{U}_m\phi_j(z), \tag{G.8}$$

where in going from the first to second line, we have used integration by parts, and from the second to third line we have used (G.3) and the fact that $K_1(z,z') = 0$ for $z = 0, 1$.

The same process is used to calculate the modal expansion of the integral term involving $\mathcal{K}_2$, which is found to be

$$\partial_z\left(\mathcal{K}_2\partial_z\boldsymbol{U}\right) = \sum_{j=0}^{\infty}\left[\int_0^1 \partial_z\left(\mathcal{K}_2\partial_z\boldsymbol{U}\right)\phi_j \,\mathrm{d}z\right]\phi_j(z), \tag{G.9}$$

$$= \sum_{j=0}^{\infty}\left[\mathcal{K}_2\partial_z\boldsymbol{U}\phi_j\Big|_{z=1} - \mathcal{K}_2\partial_z\boldsymbol{U}\phi_j\Big|_{z=0} \right.$$
$$\left. + \frac{1}{c_j^2}\int_0^1 \mathcal{K}_2\partial_z\boldsymbol{U}\Phi_j \,\mathrm{d}z\right]\phi_j(z), \tag{G.10}$$

$$= \sum_{j=0}^{\infty}\sum_{m=0}^{\infty}\left[\frac{1}{c_j^2 c_m^2}\int_0^1 K_{2,m}\Phi_j \,\mathrm{d}z\right]\boldsymbol{U}_m\phi_j(z), \tag{G.11}$$

where again we have integrated by parts, and used the expansion (G.4) along with the fact that $K_2(z, z') = 0$ on $z = 0, 1$. In the final step, we have also applied the rigid lid condition $\Phi_j(1) = 0$.

Finally, the term involving $\mathcal{L}$ is treated in much the same manner, except that we project it onto the Φ_j basis. Using the integral condition (4.51), we find

$$\partial_z\left(\mathcal{L}\partial_z B\right) = \sum_{j=0}^{\infty} \frac{1}{c_j^2}\left[\int_0^1 \partial_z\left(\mathcal{L}\partial_z B\right)\Phi_j \; \mathrm{d}z + \frac{1}{\alpha}\partial_z\left(\mathcal{L}\partial_z B\right)\Phi_j\Big|_{z=1}\right]\Phi_j(z), \tag{G.12}$$

$$= \sum_{j=0}^{\infty}\left[\mathcal{L}\partial_z B\Phi_j\Big|_{z=1} - \mathcal{L}\partial_z B\Phi_j\Big|_{z=0} + \frac{1}{\alpha}\partial_z\left(\mathcal{L}\partial_z B\right)\Phi_j\Big|_{z=1} - \int_0^1 \mathcal{L}\partial_z B\phi_j \; \mathrm{d}z\right]\Phi_j(z), \tag{G.13}$$

$$= \sum_{j=0}^{\infty}\sum_{m=0}^{\infty}\frac{1}{c_j^2}\left[\int_0^1 L_m\phi_j \; \mathrm{d}z\right] B_m\Phi_j(z), \tag{G.14}$$

where we have used the expansion (G.5) and the rigid lid condition in the final step. From these expressions, the values of $\tilde{C}_{j,m}$, $\tilde{D}_{j,m}$ and $\tilde{E}_{j,m}$ in (4.130) and (4.131) are found.

Bibliography

Allaire, G. (1992). Homogenization and two-scale convergence. *SIAM Journal on Mathematical Analysis*, 23(6):1482–1518.

Allaire, G. (2012). A brief introduction to homogenization and miscellaneous applications. *ESAIM: Proceedings*, 37:1–49.

Balagurov, B. and Kashin, V. (2001). The conductivity of a 2d system with a doubly periodic arrangement of circular inclusions. *Technical Physics*, 46:101–106.

Bauer, W., Haag, O., and Hennecke, D. (1999). Accuracy and robustness of nonlinear eddy viscosity models. In Rodi, W. and Laurence, D., editors, *Engineering Turbulence Modelling and Experiments 4*, pages 113–124. Elsevier Science Ltd, Oxford.

Bell, Z., Dance, S. L., and Waller, J. A. (2020). Accounting for observation uncertainty and bias due to unresolved scales with the schmidt-kalman filter. *Tellus, Series A: Dynamic Meteorology and Oceanography*, 72(1):1–21.

Benilov, E. S. (2000). Waves on the beta-plane over sparse topography. *Journal of Fluid Mechanics*, 423:263–273.

Bhamidipati, N., Souza, A., and Flierl, G. (2020). Turbulent mixing of a passive scalar in the ocean mixed layer. *Ocean Modelling*, 149:101615.

Bühler, O. and Holmes-Cerfon, M. (2011). Decay of an internal tide due to random topography in the ocean. *Journal of Fluid Mechanics*, 678:271–293.

Biello, J. A. and Majda, A. J. (2005). A new multiscale model for the Madden–Julian oscillation. *Journal of the Atmospheric Sciences*, 62(6):1694 – 1721.

Biello, J. A. and Majda, A. J. (2010). Intraseasonal multi-scale moist dynamics of the tropical atmosphere. *Communications in Mathematical Sciences*, 8(2):519 – 540.

Bjerknes, V., Rubenson, R., and Lindstedt, A. (1898). *Ueber einen Hydrodynamischen Fundamentalsatz und seine Anwendung: besonders auf die Mechanik der Atmosphäre und des Weltmeeres*. Kungl. Boktryckeriet. PA Norstedt & Söner.

Brahim-Otsmane, S., Francfort, G., and Murat, F. (1992). Correctors for the homogenization of the wave and heat equations. *Journal de Mathématiques Pures et Appliquées*, 71:197–231.

Briane, M. and Camar-Eddine, M. (2007). Homogenization of two-dimensional elasticity problems with very stiff coefficients. *Journal de Mathématiques Pures et Appliquées*, 88(6):483–505.

Chamsri, K. (2013). Derivation of Darcy's law using homogenization method. *International Journal of Mathematical and Computational Sciences*, 7(9):1399 – 1403.

Charney, J. (1948). *On the Scale of Atmospheric Motions*. Geofysiske publikasjoner. Grøndahl & søns boktr., I kommission hos Cammermeyer.

Cheng, B., Cullen, M. J. P., Esler, J. G., Norbury, J., Turner, M. R., Vanneste, J., and Cheng, J. (2017). A model for moist convection in an ascending atmospheric column. *Quarterly Journal of the Royal Meteorological Society*, 143(708):2925–2939.

Cioranescu, D. and Donato, P. (1999). *An Introduction to Homogenization*, volume 17.

Collins, S. N., James, R. S., Ray, P., Chen, K., Lassman, A., and Brownlee, J. (2013). Grids in numerical weather and climate models. In *Climate Change and Regional/Local Responses*, chapter 4. IntechOpen.

Colombini, F. and Spagnolo, S. (1978). On the convergence of solutions of hyperbolic equations. *Communications in Partial Differential Equations*, 3(1):77–103.

Craig, P. (1987). Solutions for internal tidal generation over coastal topography. *Journal of Marine Research*, 45(1):83–105.

Daly, K. R. and Roose, T. (2015). Homogenization of two fluid flow in porous media. *Proceedings of the Royal Society A: Mathematical, Physical and Engineering Sciences*, 471(2176):20140564.

Felbacq, D. (2016). Homogenization and transformation optics. In *Advanced Numerical and Theoretical Methods for Photonic Crystals and Metamaterials*, 2053-2571, pages 5–1 to 5–28. Morgan & Claypool Publishers.

Figotin, A. and Gorentsveig, V. (1998). Localized electromagnetic waves in a layered periodic dielectric medium with a defect. *Physical Review B*, 58:180–188.

Figotin, A. and Klein, A. (1997). Localization of classical waves I: Acoustic waves. *Communications in Mathematical Physics*, 180:439–482.

Flanders, H. (1973). Differentiation under the integral sign. *The American Mathematical Monthly*, 80(6):615–627.

Forster, C., Stohl, A., and Seibert, P. (2007). Parameterization of convective transport in a Lagrangian particle dispersion model and its evaluation. *Journal of Applied Meteorology and Climatology*, 46(4):403 – 422.

Francfort, G. A. and Murat, F. (1992). Oscillations and energy densities in the wave equation. *Communications in Partial Differential Equations*, 17(11-12):1785–1865.

Garrett, C. and Kunze, E. (2007). Internal tide generation in the deep ocean. *Annual Review of Fluid Mechanics*, 39(1):57–87.

Gill, A. E. (1980). Some simple solutions for heat-induced tropical circulation. *Quarterly Journal of the Royal Meteorological Society*, 106(449):447–462.

Gill, A. E. (1982). *Atmosphere-Ocean Dynamics*. Academic Press New York.

Godin, Y. A. (2013). Effective complex permittivity tensor of a periodic array of cylinders. *Journal of Mathematical Physics*, 54(5):053505.

Goldsmith, E. and Esler, J. (2021). Wave propagation in rotating shallow water in the presence of small-scale topography. *Journal of Fluid Mechanics*, 923:A24.

Gregory, D. (2002). The mass-flux approach to the parametrization of deep convection.

Guedes, J. and Kikuchi, N. (1990). Preprocessing and postprocessing for materials based on the homogenization method with adaptive finite element methods. *Computer Methods in Applied Mechanics and Engineering*, 83(2):143–198.

Hamill, T. M. and Whitaker, J. S. (2005). Accounting for the error due to unresolved scales in ensemble data assimilation: A comparison of different approaches. *Monthly Weather Review*, 133(11):3132 – 3147.

Hara, T. and Mei, C. C. (1987). Bragg scattering of surface waves by periodic bars: theory and experiment. *Journal of Fluid Mechanics*, 178:221–241.

Hassani, B. and Hinton, E. (1999). *Homogenization Theory for Media with Periodic Structure*, pages 11–30. Springer London.

Holmes, M. (2012). *Introduction to Perturbation Methods*. Texts in Applied Mathematics. Springer New York.

Holton, J. R. (2004). *An Introduction to Dynamic Meteorology*. International Geophysics Series. Elsevier Academic Press, fourth edition.

Holton, J. R. and Hakim, G. J. (2013). Chapter 11 - tropical dynamics. In *An Introduction to Dynamic Meteorology*, pages 377–411. Academic Press, Boston, fifth edition.

Holtslag, A. A. (2003). Atmospheric turbulence. In *Encyclopedia of Physical Science and Technology*, pages 707–719. Academic Press, New York, third edition.

Houze, R. A. (1977). Structure and dynamics of a tropical squall–line system. *Monthly Weather Review*, 105(12):1540 – 1567.

Houze, R. A. (1993). Chapter 10 clouds in hurricanes. In *Cloud Dynamics*, volume 53 of *International Geophysics*, pages 405–437. Academic Press.

Hu, X. and Chan, C. T. (2005). Refraction of water waves by periodic cylinder arrays. *Physical Review Letters*, 95:154501.

Hyder, P., Edwards, J., Allan, R., Hewitt, H., Bracegirdle, T., Gregory, J., Wood, R., Meijers, A., Mulcahy, J., Field, P., Furtado, K., Bodas-Salcedo, A., Williams, K., Copsey, D., Josey, S., Liu, C. l., Roberts, C., Sanchez, C., Ridley, J., and Belcher, S. E. (2018). Critical southern ocean climate model biases traced to atmospheric model cloud errors. *Nature Communications*, 9:3625.

Janjić, T. and Cohn, S. E. (2006). Treatment of observation error due to unresolved scales in atmospheric data assimilation. *Monthly Weather Review*, 134(10):2900 – 2915.

Jansons, K. M. and Johnson, E. R. (1988). Topographic Rossby waves above a random array of sea mountains. *Journal of Fluid Mechanics*, 191:373–388.

Keller, J. B. (1963). Conductivity of a medium containing a dense array of perfectly conducting spheres or cylinders or nonconducting cylinders. *Journal of Applied Physics*, 34(4):991–993.

Kelly, S. M. (2016). The vertical mode decomposition of surface and internal tides in the presence of a free surface and arbitrary topography. *Journal of Physical Oceanography*, 46(12):3777 – 3788.

Kelly, S. M., Nash, J. D., and Kunze, E. (2010). Internal-tide energy over topography. *Journal of Geophysical Research: Oceans*, 115(C6).

Kuell, V. and Bott, A. (2022). A nonlocal three-dimensional turbulence parameterization (NLT3D) for numerical weather prediction models. *Quarterly Journal of the Royal Meteorological Society*, 148(742):117–140.

Kurganov, A., Liu, Y., and Zeitlin, V. (2020). Moist-convective thermal rotating shallow water model. *Physics of Fluids*, 32(6):066601.

Kurganov, A., Liu, Y., and Zeitlin, V. (2021). Thermal versus isothermal rotating shallow water equations: comparison of dynamical processes by simulations with a novel well-balanced central-upwind scheme. *Geophysical & Astrophysical Fluid Dynamics*, 115(2):125–154.

Laplace, P. M. d. (1776). Suite des récherches sur plusieurs points du systeme du monde (xxv-xxvii). *Mém. Présentés Divers Savans Acad. R. Sci. Inst. France*, pages 525–52.

Li, S., Rupp, D., Hawkins, L., Mote, P., McNeall, D., Sparrow, S., Wallom, D., Betts, R., and Wettstein, J. (2019). Reducing climate model biases by exploring parameter space with large ensembles of climate model simulations and statistical emulation. *Geoscientific Model Development*, 12:3017–3043.

Li, Y. and Mei, C. C. (2014). Scattering of internal tides by irregular bathymetry of large extent. *Journal of Fluid Mechanics*, 747:481–505.

Ling, J. and Zhang, C. (2013). Diabatic heating profiles in recent global reanalyses. *Journal of Climate*, 26(10):3307 – 3325.

Longuet-Higgins, M. S. (1967). On the trapping of wave energy round islands. *Journal of Fluid Mechanics*, 29(4):781–821.

Majda, A. and Klein, R. (2003). Systematic multiscale models for the tropics. *Journal of the Atmospheric Sciences*, 60:393–408.

Mapes, B. E. and Houze, R. A. (1993). Cloud clusters and superclusters over the oceanic warm pool. *Monthly Weather Review*, 121(5):1398 – 1416.

Matsuno, T. (1966). Quasi-geostrophic motions in the equatorial area. *Journal of the Meteorological Society of Japan. Ser. II*, 44(1):25–43.

McPhedran, R. and McKenzie, D. (1980). Electrostatic and optical resonances of arrays of cylinders. *Applied Physics*, 23:223–235.

McPhedran, R. C., Poladian, L., and Milton, G. W. (1988). Asymptotic studies of closely spaced, highly conducting cylinders. *Proceedings of the Royal Society of London*, 415(1848):185–196.

Mei, C. C. (1985). Resonant reflection of surface water waves by periodic sandbars. *Journal of Fluid Mechanics*, 152:315–335.

Mei, C. C. and Vernescu, B. (2010). *Homogenization Methods for Multiscale Mechanics*. World Scientific.

Motsa, S., Magagula, V., and Sibanda, P. (2014). A bivariate Chebyshev spectral collocation quasilinearization method for nonlinear evolution parabolic equations. *The Scientific World Journal*, vol 2014.

Mottin, S., Panasenko, G., and Ganesh, S. S. (2011). Multiscale modeling of light absorption in tissues: Limitations of classical homogenization approach. *PLOS One*, 5(12):1–9.

Muzara, H., Shateyi, S., and Marewo, G. T. (2018). On the bivariate spectral quasi-linearization method for solving the two-dimensional Bratu problem. *Open Physics*, 16(1):554–562.

Naciri, M. and Mei, C. C. (1988). Bragg scattering of water waves by a doubly periodic seabed. *Journal of Fluid Mechanics*, 192:51–74.

Nandakumaran, A. (2007). An overview of homogenization. *Journal of the Indian Institute of Science*, 87.

North, G. R., Pyle, J., and Zhang, F. (2015). Mesoscale meteorology - mesoscale convective systems. In *Encyclopedia of Atmospheric Sciences*, pages 339–354. Academic Press, Oxford, second edition.

Ogura, Y. and Phillips, N. A. (1962). Scale analysis of deep and shallow convection in the atmosphere. *Journal of the Atmospheric Sciences*, 19(2):173 – 179.

Olbers, D., Willebrand, J., and Eden, C. (2012). *Ocean Dynamics*.

Paldor, N., Rubin, S., and Mariano, A. J. (2007). A consistent theory for linear waves of the shallow-water equations on a rotating plane in midlatitudes. *Journal of Physical Oceanography*, 37(1):115–128.

Paldor, N. and Sigalov, A. (2008). Trapped waves on the mid-latitude β-plane. *Tellus A*, 60(4):742–748.

Papanicolau, G., Bensoussan, A., and Lions, J. (1978). *Asymptotic Analysis for Periodic Structures*. Elsevier Science.

Pastukhova, S. E. (2005). Homogenization of elasticity problems on periodic composite structures. *Sbornik: Mathematics*, 196(7):1033–1073.

Pathak, R., Sahany, S., Mishra, S., and Dash, S. (2019). Precipitation biases in CMIP5 models over the South Asian region. *Scientific Reports*, 9:9589.

Pavliotis, G. and Stuart, A. (2008). *Multiscale Methods: Averaging and Homogenization*. Texts in Applied Mathematics. Springer New York.

Pedlosky, J. (1987). *Geophysical Fluid Dynamics*. Springer-Verlag, New York.

Phillips, N. A. (1963). Geostrophic motion. *Reviews of Geophysics*, 1(2):123–176.

Plumb, R. A. and Hou, A. Y. (1992). The response of a zonally symmetric atmosphere to subtropical thermal forcing: Threshold behavior. *Journal of the Atmospheric Sciences*, 49(19):1790 – 1799.

Rayleigh, L. (1892). On the influence of obstacles arranged in rectangular order upon the properties of a medium. *Philosophical Magazine*, 34(211):481–502.

Reuss, A. (1929). Berechnung der fließgrenze von mischkristallen auf grund der plastizitätsbedingung für einkristalle . *Journal of Applied Mathematics and Mechanics / Zeitschrift für Angewandte Mathematik und Mechanik*, 9(1):49–58.

Rhines, P. and Bretherton, F. (1973). Topographic Rossby waves in a rough-bottomed ocean. *Journal of Fluid Mechanics*, 61(3):583–607.

Romps, D. M. and Kuang, Z. (2011). A transilient matrix for moist convection. *Journal of the Atmospheric Sciences*, 68(9):2009 – 2025.

Rosales, R. and Papanicolaou, G. (1983). Gravity waves in a channel with a rough bottom. *Studies in Applied Mathematics*, 68:89–102.

Rossby, C. G. (1936). Dynamics of steady ocean currents in the light of experimental fluid mechanics.

Rossby, C. G. (1940). Planetary flow patterns in the atmosphere. *Quarterly Journal of the Royal Meteorological Society*, 66:68–87.

Scaife, A., Woollings, T., Knight, J., Martin, G., and Hinton, T. (2010). Atmospheric blocking and mean biases in climate models. *Journal of Climate*, 23:6143–6152.

Sheng, P., White, B., Zhang, Z.-Q., and Papanicolaou, G. (1986). Minimum wave-localization length in a one-dimensional random medium. *Physical Review B*, 34:4757–4761.

Shnirelman, A. (1993). The lattice theory and the flows of an ideal incompressible fluid. *Russian journal of mathematical physics*, 1:105–114.

Shnirelman, A. (2013). On the long time behavior of fluid flows. *Procedia IUTAM*, 7:151–160. IUTAM Symposium on Topological Fluid Dynamics: Theory and Applications.

Smith, S. G. L. and Young, W. R. (2002). Conversion of the barotropic tide. *Journal of Physical Oceanography*, 32(5):1554 – 1566.

Stull, R. B. (1984). Transilient turbulence theory. part I: The concept of eddy-mixing across finite distances. *Journal of the Atmospheric Sciences*, 41(23):3351 – 3367.

Thorpe, A. J., Volkert, H., and Ziemianski, M. J. (2003). The Bjerknes' Circulation Theorem: A Historical Perspective. *Bulletin of the American Meteorological Society*, 84(4):471–480.

Ting, D. S.-K. (2016). Chapter 2 - equations of fluid in motion. In *Basics of Engineering Turbulence*, pages 19–46. Academic Press.

Trefethen, L. N. (2000). *Spectral Methods in MATLAB*. SIAM, Philadelphia.

Vallis, G. K. (2006). *Atmospheric and Oceanic Fluid Dynamics*. Cambridge University Press, Cambridge.

Van Der Baan, M. (2001). Acoustic wave propagation in one dimensional random media: the wave localization approach. *Geophysical Journal International*, 145(3):631–646.

Vanneste, J. (2000a). Enhanced dissipation for quasi-geostrophic motion over small-scale topography. *Journal of Fluid Mechanics*, 407:105–122.

Vanneste, J. (2000b). Rossby wave frequency change induced by small-scale topography. *Journal of Physical Oceanography*, 30(7):1820–1826.

Voigt, W. (1928). *Lehrbuch der Kristallphysik (mit Ausschluss der Kristalloptik)*. Vieweg+Teubner Verlag.

Waller, J. A., Dance, S. L., and Lean, H. W. (2021). Evaluating errors due to unresolved scales in convection-permitting numerical weather prediction. *Quarterly Journal of the Royal Meteorological Society*, 147(738):2657–2669.

Warneford, E. S. and Dellar, P. J. (2013). The quasi-geostrophic theory of the thermal shallow water equations. *Journal of Fluid Mechanics*, 723:374–403.

Wirth, V. (1998). Thermally forced stationary axisymmetric flow on the f plane in a nearly frictionless atmosphere. *Journal of the Atmospheric Sciences*, 55(19):3024 – 3041.

Wirth, V. and Dunkerton, T. J. (2006). A unified perspective on the dynamics of axisymmetric hurricanes and monsoons. *Journal of the Atmospheric Sciences*, 63(10):2529 – 2547.

Wood, R. and Mcintyre, M. (2009). A general theorem on angular-momentum changes due to potential vorticity mixing and on potential-energy changes due to buoyancy mixing. *Journal of the Atmospheric Sciences*, 67.

Zadra, A., Williams, K., Frassoni, A., Rixen, M., Ángel F. Adames, Berner, J., Bouyssel, F., Casati, B., Christensen, H., Ek, M. B., Flato, G., Huang, Y., Judt, F., Lin, H., Maloney, E., Merryfield, W., Niekerk, A. V., Rackow, T., Saito, K., Wedi, N., and Yadav, P. (2018). Systematic errors in weather and climate models: Nature, origins, and ways forward. *Bulletin of the American Meteorological Society*, 99(4):ES67 – ES70.

Zeitlin, V. (2018). *Geophysical fluid dynamics : understanding (almost) everything with rotating shallow water models*. Oxford University Press, first edition.